Analysis and Characterization of Nanomembranes and Adlayers

Dissertation

submitted in partial fulfillment
of the requirements for the degree of
Doktor der Naturwissenschaften
(Dr. rer. nat.)

Roland Hillmann

Bielefeld University
Faculty of Physics
April 2019

für Nadine

Wahr sind auch die Erinnerungen, die wir mit uns tragen;
die Träume, die wir spinnen, und die Sehnsüchte, die uns treiben.
Damit wollen wir uns bescheiden.

(Heinrich Spoerl)

Hiermit versichere ich,

1. dass mir die geltende Promotionsordnung der Fakultät für Physik bekannt ist.

2. dass ich die vorliegende Dissertation selbst angefertigt, keine Textabschnitte von Dritten oder eigenen Prüfungsarbeiten ohne Kennzeichnung übernommen und alle von mir benutzten Hilfsmittel und Quellen in der Arbeit angegeben habe.

3. dass Dritte weder unmittelbar noch mittelbar geldwerte Leistungen von mir für Vermittlungstätigkeiten oder für Arbeiten erhalten haben, die im Zusammenhang mit dem Zustandekommen oder dem Inhalt der Dissertation stehen.

4. dass ich diese Dissertation oder wesentliche Teile davon nicht als Prüfungsarbeit für eine staatliche oder andere wissenschaftliche Prüfung eingereicht habe.

5. dass ich die gleiche, eine in wesentlichen Teilen ähnliche oder eine andere Abhandlung nicht bei einer anderen Hochschule als Dissertation eingereicht habe.

(Roland Hillmann)

Eingereicht am 30.04.2019

Referees

Prof. Dr. Dario Anselmetti
Experimental Biophysics and Applied Nanoscience
Faculty of Physics, Bielefeld University

Prof. Dr. Armin Gölzhäuser
Physics of Supramolecular Systems and Surfaces
Faculty of Physics, Bielefeld University

Abstract

A membrane is a barrier that can be passable to some things but impassable to others. Such things may be molecules, ions, or other small particles. Biological membranes come with a great variety, ranging from cell membranes, nuclear membranes to tissue membranes that cover the surface of internal organs. In contrast, synthetic membranes have been fabricated and utilized by humans for use in laboratories and industry for filtration and separation.

The scope of this work is to establish and characterize free-standing as well as substrate supported membranes of the thickness of only a few molecules. The fabrication of these *2D-nanomambranes* was achieved by the Langmuir-Blodgett (LB) technique, by a horizontal Montal-Mueller method, as well as by crosslinking of selfassembled layers. Isotherms of monolayer material were investigated at the LB trough. Transferred to substrates, they were studied with atomic force microscopy (AFM), helium ion microscopy (HIM), and infrared spectroscopy. Self assembling phenomena of photopolymerizable lipids on HOPG were revealed by AFM in dependence of their degree of polymerization. Infrared spectroscopy clarified the polymerization process from a chemical perspective. Free-standing membranes of polymerized lipids could be investigated by AFM and HIM due to their enhanced mechanical properties.

Free-standing lipid membranes were also fabricated in a fluid chamber. In this aqueous environment, electrophysiological recordings of lipid bilayer membranes were performed with the final measurement of free translocation of short DNA fragments through embedded α-Hemolysin pores. Specific membrane capacitance as well as conductance of α-Hemolysin were analyzed.

Furthermore, solid-state membranes from selfassembled monolayers were fabricated and studied electrophysiologically. Ion permeation through these carbon nanomembranes (CNM) of various ion species was investigated with respect to their potential application for filtration purposes.

Contents

1 Introduction and Motivation

Fascinating solutions to various problems have been developed in the process of evolution. And to fully understand complex problems of any kind, one has to explore the details. This is especially true for modern natural science.

Biophysical processes take place in an environment of high complexity and are always under the influence of a large number of different factors. Therefore, it is essential to limit the interactions of a system to a controllable minimum in order to understand the influence of a certain reaction to the overall picture. This is the birth of the controlled modern experiment. Only the combination of findings of many such sharply limited individual experiments gives rise to answers to complex problems.

One of the most fascinating and crucial molecules is deoxyribonucleic acid (DNA), which can be understand as the blueprint to all known organism.[1] Precise knowledge of DNA sequences has become an important key in numerous fields such as medical diagnosis,[2,3] molecular cloning,[4,5] forensic biology,[6,7] molecular biology,[8] and biological systematics.[9]

Starting with the Sanger sequencing technique (named after F. Sanger) in the 1970s, which is based on the statistical incorporation of chain-terminating dideoxynucleotides by DNA polymerase during in vitro DNA replication,[10] DNA sequencing has reached the fourth generation by now[11] and is dominated by high-throughput techniques, which are opening fascinating new opportunities.[12–14]

These latest sequencing technologies are based on nanopore detection of single molecules and are one of the most powerful sequencing technologies to this day.[11] DNA sequencing using nanopores comes with significant advantages such as label-free,[15] ultra-long reads (up to 1.3×10^6 bases),[16] high throughput (450 bases of DNA per second per nanopore),[16] and low material requirement.[17] Recently, nanopore sensing has been extended to the field of protein sequencing.[18–20]

Nanopore sensing is based on the concept of the *Coulter counter*, which was originally used to detect cells and particles.[21] Two chambers that are filled with electrolyte solutions are separated by a membrane that contains one or more nanochannels. When

a voltage is applied across the membrane, an ionic current through the nanopore can be detected. However, when electrically charged molecules are present, they temporarily modulate the ionic current as they pass through the nanopore, which allows them to be detected.[22] Membrane materials vary widely but can be divided into solid-state and biological membranes.

The concept of DNA sequencing by using membranes containing a nanoscopic channel was formed in 1989 by D. Deamer.[23] DNA molecules would be pulled in a linear fashion through a hole in the membrane, driven by an electrical potential. Based on the different structures of the four bases, the DNA sequence could be read out by analyzing the varying current through the nanopore.

In 1996, D. Deamer, D. Branton and J. Kasianowitz published the first demonstration that nanopore sequencing by using a pore protein (α-Hemolysin) embedded in a lipid membrane may be feasible.[22]

The success and the wide range of applications of biological membranes for DNA sequencing led to the development of solid-state membranes with similar dimensions. In contrast to biological membranes, which are generally phospholipid membranes and rather fragile, membranes made from solid-state materials have advanced mechanical properties. Superior stability and easy producibility are a key feature of membranes of solid-state materials like silicon nitride,[24] graphene,[25] molybdenum disulfide[26] and boron nitride.[27] Nanopores within solid-state materials are then fabricated via ion beam[28] or electron beam sculpting.[29]

Membranes are of general use as they are a barrier on one side, but can be passable at the same time for a selective number of objects. Such things may be molecules, ions, or other small particles. Besides a great variety in biology,[30] membranes have been fabricated and utilized for a long time by humans for use in manufacturing, industry and laboratories for filtration and separation.

Water purification is a global challenge and membranes are a crucial part of that technology. While standard purification presses water through membranes with high pressure to separate its constituents,[31] nanotechnology uses submicrometer thick carbon membranes that are completely impermeable to liquids, vapors, and gases, but these membranes allow unimpeded permeation of water.[32,33] By using reverse osmosis, these membranes are potent in the separation of inorganic salts and small organic molecules.[34] Nanofiltration membranes have come a long way since they were first recognized in the late 1980s.[35]

In this work, various membrane materials were characterized in a free-standing as

well as substrate supported manner. The fabrication of these *2D-nanomambranes* was achieved by Langmuir-Blodgett (LB) technique, by a horizontal Montal-Mueller method, as well as by selfassembled layers. Phospholipids containing diyne groups in their hydrocarbon chains were used as photopolymerizable material to establish a membrane that is biomimetic but come with advanced mechanical properties over conventional lipid membranes. Their free-standing properties were investigated using atomic force microscopy (AFM) and helium ion microscopy (HIM).[36] Infrared spectroscopy was used on substrate supported lipid adlayers to study and clarify the polymerization process from a chemical perspective.[36]

In a second approach, double layered lipid membranes (bilayers) were fabricated in a fluid chamber using a horizontal Montal-Mueller method.[37,38] In this aqueous environment, electrophysiological recordings of lipid bilayer membranes made from conventional as well as polymerizable lipids were performed. Specific membrane capacitance as well as conductance of α-Hemolysin that incorporated into the lipid bilayer were analyzed. Initial experiments of UV-induced polymerization of lipid bilayers in aqueous environments were carried out. Using α-Hemolysin, nanopore sensing experiments of short DNA fragments were performed.

The third section of this thesis is about carbon nanomembranes (CNM), which are solid-state membranes made from carbon-rich material. Fabricated and designed by Prof. A. Gölzhäuser and his group *Physics of Supramolecular Systems and Surfaces* of the Faculty of Physics of Bielefeld University, electrophysiological experiments were performed in a collaboration with Y. Yang. Ion permeation through CNM of various ion species were investigated with respect to their potential application for osmosis purposes.[33,39]

2 Background and Theory

2.1 DNA

If there were a single molecule that is highly symbolic for life - it would be DNA, short for *deoxyribonucleic acid*. It is the blueprint of all biological components of an organism and is present[40] in the nucleus of every eukaryotic cell. Through the process of DNA replication during each cell division, information is passed on from generation to generation. Information is organized in genes, which are sections within the DNA. Functional biological molecules like proteins are then generated in a process called *gene expression* from a sequence of the DNA.[1] The subdivision of DNA into small sections, called *genes*, was first suggested by G. Mendel who established the *laws of Mendelian inheritance*.[41] Because of its fundamental significance in context of full understanding of living organism, DNA is part of broad scientific research to this day, such as genome editing technologies,[42] sequencing technologies,[43] but also nanostructures[44] and high density information storage.[45]

DNA was first isolated by F. Miescher in 1869, when he isolated phosphate-rich chemicals from the nuclei of white blood cells. He named it *nuclein*, from which *nuclein acid* later emerged.[46] In 1953, J. Watson and F. Crick proposed the helical structure of DNA by X-ray diffraction.[47] As it proved to be correct, they received the Nobel Prize for medicine in 1962.

DNA consists of two individual strands, which spiral together around one axis to form a helix. The polynucleotide chains run parallel to each other but with opposite directionality, which is referred to as *antiparallel*. Each of the two chains consists of the periodic sequence of a phosphate group and a 2-deoxy-β-D-ribofuranose. Ladder-like, the sugar-phosphate backbones of two DNA strands form a double helix, while the bases protrude into the interior.[48]

Consisting of a phosphate group, a deoxyribofuranose, and one of four possible bases (Fig. 2.1), the smallest subunit of DNA is the nucleotide (Fig. 2.2). Each base is either a purine (adenine or guanine) or a pyrimidine (thymine or cytosine).
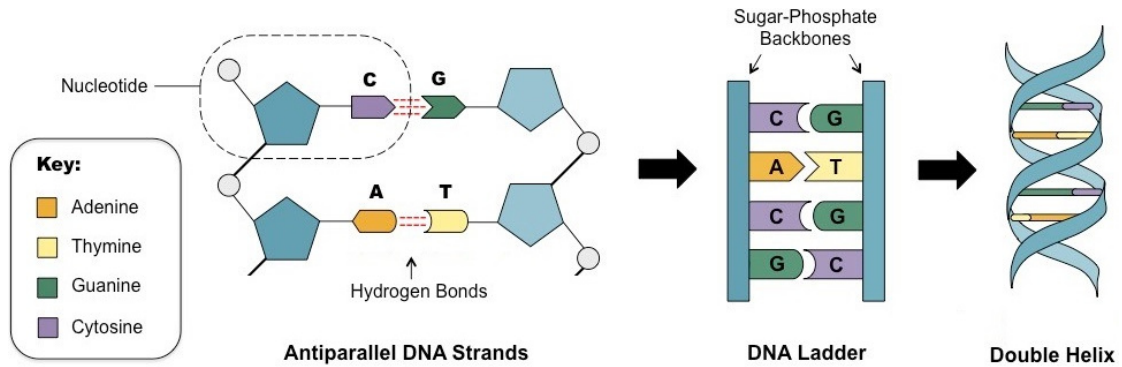
Figure 2.1: The smallest subunit of DNA is the *nucleotide*, which is marked by the dashed circle. It is attached to the sugar of another nucleotide at its phosphate group. Two polynucleotide chains are bounded by hydrogen bonds between complementary bases (red dashed lines). The two polynucleotide chains are antiparallel. The most stable energy configuration is formed by a double helix with about 10.5 bases per turn.[49]

The base is attached to the 1'-C atom of the cyclic sugar, the phosphate is located at the 5'-C atom. The next higher order is achieved when the phosphate group binds to the ribose of another nucleotide via a phosphodiester bond at the 3'-C atom.[50] This results in a single strand with a sequence of bases that is not necessarily helically ordered. Only the interaction with a second, complementary strand leads to the expression of the double helix. This second strand is orientated antiparallel to the first and contains a sequence of complementary bases, which is given by the sequence of the first strand. The formation of hydrogen bonds between two bases is called *base-pairing* and establishes only between matching partners. Due to their chemical structure, two (adenine-thymine) or three (guanine-cytosine) hydrogen bonds are formed. The presence of thousands of such hydrogen bonds in a DNA molecule contributes greatly to the stability to the helix.[51] Van der Waals interactions between the aromatics of adjacent base pairs stabilize the DNA additionally.[48]

From a hypothetical point of view, DNA could be arranged in a simple ladder design, with the paired bases being the steps and the phosphate the rails. It is known from elementary chemistry that the distance between adjacent sugars or phosphates in the DNA chain is 0.6 nm. But the distance between each base pair in a DNA molecule is found to be 0.33 nm.[52] This would leave a gap of 0.27 nm between the stacked bases. To minimize this space, DNA could form a skewed ladder, with no gaps between the paired bases. But this would lead to many unacceptably close contacts between neighboring atoms.[53]
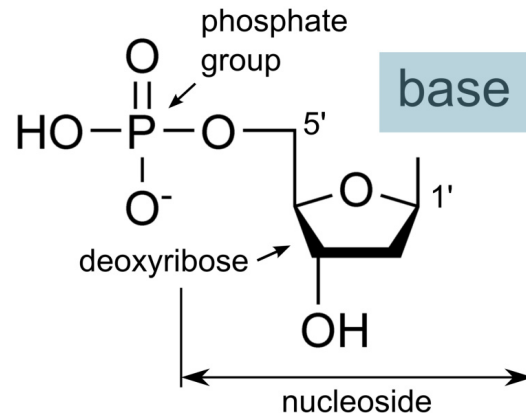
Figure 2.2: A nucleotide contains the five-carbon sugar deoxyribose in a circular configuration, a nitrogenous base attached to the 1'-C of the sugar, and one phosphate group attached to the 5'-C atom of the sugar. The deoxyribose sugar joined only to the base forms a nucleoside, whereas the whole structure along with the phosphate group is a nucleotide.

In the accepted double-helix shape of DNA, a complete turn is achieved after 3.6 nm in a right-handed double helix. In solution, this section averages about 10.5 phosphates per turn.[54] Therefore, two bases exhibit an angle of 32.3° to each other. The diameter of the double helix is about 2.4 nm.[53]

High solubility of the DNA in an aqueous environment results from the spatial arrangement of the base pairs in the interior and the phosphate backbone on the outside. The double negatively charged phosphate group makes DNA a polyanion. This charge is shielded by a layer of water molecules, as well as by divalent cations.[55] A completely extended polymer would bind numerous water molecules. From the perspective of the *principle of maximum entropy*, a compact polymer structure is energetically favorable. Therefore, a sufficient length of DNA strand forms a random coil in aqueous solutions.[56]

2.2 Nanopore Sensing

Nanopore sensing is based on the concept of the *Coulter counter*, which was originally used to detect cells and particles. Two chambers that are filled with electrolyte solutions are separated by a membrane that contains one or more nanochannels. When a voltage is applied across the membrane, an ionic current through the membrane can be detected. However, when electrically charged molecules are present, they temporarily modulate the ionic current as they pass through the membrane, which allows

them to be detected. The advantages of this nanopore technology are single-molecule sensitivity at low cost and label-free detection without molecular amplification.[57]

Nanopore sensing has become a very successful technique in the field of nanotechnology and molecular biology with its high sensitivity and versatility.[12,13] It provided a detailed insight into nanoscale molecular transport mechanisms.[58] Transposition of ions and molecules through the biological cellmembrane via ionchannels is essential for life. The passage of messenger RNA from the cell nucleus into the cytosol is controlled by nuclear membrane pores. Proteins are secreted across pores in the membranes of cell organelles, and viruses dump their genomes into cells via pores that they insert into the cell membrane. Some of the transport through pores is passive, although most of it is actively controlled.[59]

In 1989, D. Deamer formed the concept of *DNA sequencing* by using a nanoscopic channel.[23] DNA molecules would be pulled in a linear fashion through a hole in a membrane, driven by an electrical potential. Based on the different structures of the four bases, the DNA sequence could be read out by analyzing the varying current through the nanopore (Fig. 2.3).
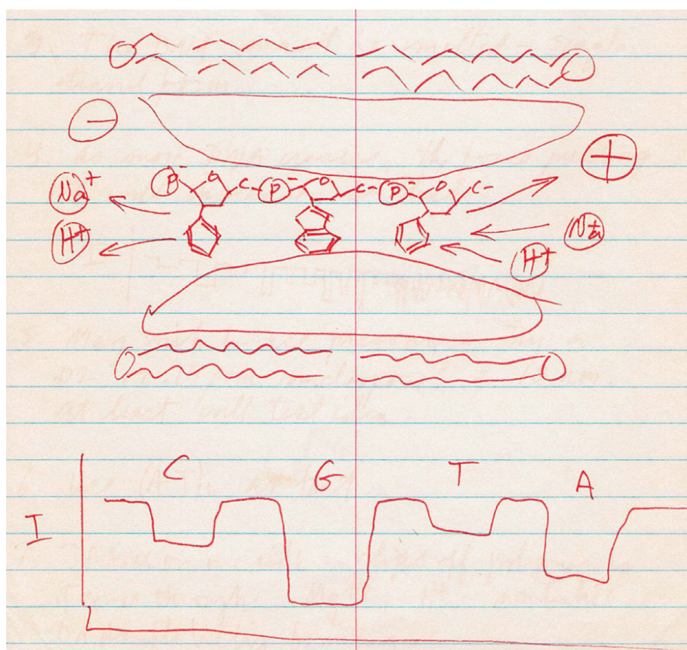

Figure 2.3: This is part of the original sketch of D. Deamer for the detection of individual bases in a DNA sequence by translocation through a biological nanopore embedded in a lipid bilayer. In the lower part of the figure, an electrical readout is shown with each base affecting the current in a distinct way, which allows the read out of the bases. Dated June 25, 1989.[23]

In 1996, D. Deamer, D. Branton and J. Kasianowitz published the first demonstration that nanopore sequencing is feasible using the pore protein α-*Hemolysin* (α-HL).[22] Since the first use of α-HL as a nanopore, additional biological nanopores with varios characteristics have been developed and utilized in many sensing applications. These protein pores, which are also called *porins* (Fig. 2.4), were used in the detection of metal ions,[60] small molecules,[61] nucleotides,[62,63] and proteins[64,65] as well as differentiation between classes of nucleotide conformations.[66]

The success and the wide range of applications of biological nanopores led to the development of solid-state nanopores with similar diameter. In contrast to biological pores, which have to be embedded in a rather fragile lipid membrane, membranes made from solid-state materials have advanced mechanical properties. Superior stability and easy producibility are a key feature of membranes of solid-state materials like silicon nitride,[24] graphene,[25] molybdenum disulfide[26] and boron nitride.[27]
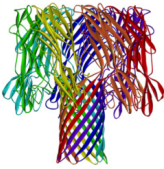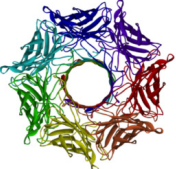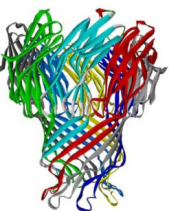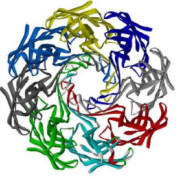
Biological Nanopore	Structure		Critical Dimension	Types of Analytes
	Side View	Top View		
α-HL			1.4nm	small molecules, RNA, ssDNA, dsDNA, proteins
OmpG			1.3nm	small molecules, proteins
MspA			1.2nm	ssDNA, dsDNA

Figure 2.4: Three of the most commonly used biological porins and some of their specifications. Subdomains are illustrated by a colorscheme. Inspired by a Figure in *Shi et al.*[14,67]

Nanopores within solid-state materials are then fabricated via ion beam[28] or electron beam sculpting.[29] Glass pipettes can also be utilized for nanopore sensing.[68]

All synthetic nanopores have tunable properties such as size, geometry, and surface chemistry as well as enhanced mechanical, thermal, and chemical stability in comparison to their biological counterparts. Nonetheless, synthetic nanopores usually lack the specificity of protein pores found in nature.[14]

2.2.1 Detection Method

In the late 1940s, W. Coulter discovered the *Coulter Principle* to simplify and improve blood cell analysis. The U.S. patent, granted in 1953, was claiming for counting particles suspended in a fluid.[21] By the use of an electric field, size and number of dilute suspensions of particles in conducting liquids can be estimated. Centerpiece of a *Coulter counter* is one or more microchannels, separating two chambers of electrolyte solutions. Applying a voltage of a few millivolts across the membrane cause particles in the fluid to be drawn through the microchannel. Each particle then causes a change of the electrical resistance of the channel. Analysis of these changes leads to the determination of the size and shape of each translocated particle.[69]

Modern nanopore sensors have evolved from the first Coulter counter by shrinking the pore size to the nanometer scale. Since the relative change of the electric resistance depends on the ratio of pore to particle diameter, nanopores of similar size as the investigated particles are essential. Experimental setups that are using the mentioned detection scheme usually consist of a nanoscale hole within a membrane, biological or synthetic, separating two reservoirs filled with an electrolytic solution. Each reservoir contains an electrode to apply a constant potential across the membrane. Due to the flow of ions through the nanopore, a constant electric current is detectable. Molecules dissolved in the solution pass through the nanopore and are detected as a temporary obstruction of the pore by causing detectable modulations in the electrical current. Size, shape and charge of the molecules are affecting amplitude, duration and frequency of the current modulations. Because of its functional principle, no labeling or modification of the transpassing molecules of interest is necessary. That allows for characterizing of biological molecules with their functional integrity.

In the first successful demonstration, a single stranded DNA (ssDNA) and RNA molecules were electrophoretically driven through an α-HL pore. Because parts of the liquid volume of the nanopore that carries the ionic current are occupied by a DNA molecule, the translocation results in a transient current. Translocation times

are quite fast: for typical conditions, a strand containing 100 nucleotides of cytosine will passes through in about 0.1 ms.[70]

2.2.2 Biological Nanopores

The use of biological nanopores for nanopore sensing is inspired from nature, where a variety of biological transport processes across the cell membrane are controlled and regulated by protein channels. The size of protein pores are of similar size as many biologically important analyte molecules and specifications of the former are highly reproducible with atomic precision. However, to meet individual requirements, biological nanopores can be engineered in a wide variety of approaches like site-directed mutagenesis or incorporation of specific adaptors.[71]

First nano-sensing experiments were performed[22] with α-Hemolysin (α-HL), which is the major cytotoxic agent released by bacterium *Staphylococcus aureus* and the first identified member of the pore forming beta-barrel toxin family.[72] It is a mushroom-shaped, heptameric transmembrane pore formed by self-assembly of seven monomers in the lipid bilayer and measures 10 nm in height and up to 10 nm in diameter. The cap domain of the protein pore protrudes when embedded into a lipid bilayer (Fig. 2.5). The structure has an opening of 2.6 nm, a wider 4.6 nm area and is 1.4 nm at the narrowest point.[73] Because of this constriction, only single stranded DNA or RNA is able to pass through an α-HL pore. The nanocavity can be used for biotechnological engineering.[74]

The transmembrane protein pore *Mycobacterium smegmatis porin A* (MspA) is similar to α-HL (Fig. 2.4) and is a funnel shaped octameric channel pore that allows diffusional transport of water-soluble molecules.[75]
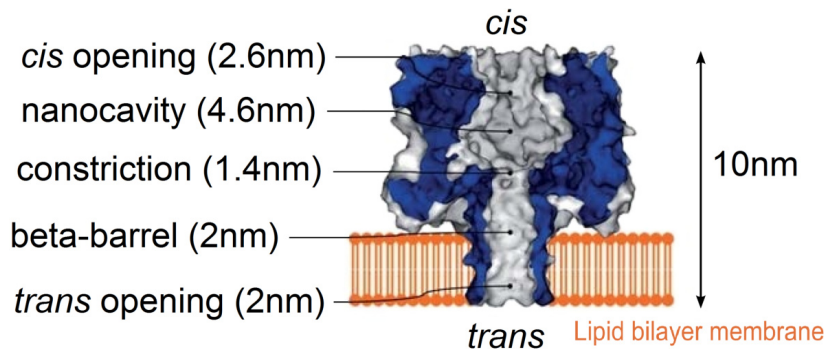

Figure 2.5: Section through an α-HL embedded into a bilayer lipid membrane. Critical diameters of various regions within the funnel are given.[76]

Geometrically, MspA consists of a single constriction with a diameter of 1.2 nm and a length of 0.6 nm.[77] The advantage of MspA over α-HL lies in the length of the constriction region, as it is important for the sensitivity in a Coulter counter measurement. While a strand of DNA translocates through a nanopore, the ion current signal of each base is influenced by neighboring bases within the constricting region. With shorter constricting region comes a better signal interpretation and contributions from nearby bases are reduced. With the distance between two bases in ssDNA being about 0.34 nm,[47] a total number of 15 bases will coexist within an α-HL pore that has a 5 nm constriction region. In the case of MspA, only 3-4 bases are dominating the current modulation, because the narrowest region is only of 0.6 nm. Analysis of individual bases should therefore be much more advanced and reach higher resolution by using MspA in comparison to α-HL for nanopore sensing. Demonstration of the use of MspA for DNA sequencing has been shown.[78]

Another promising transmembrane protein pore is the *outer membrane protein G* (OmpG), which is a monomeric β-barrel protein pore with seven flexible loops at the extra-cellular side (Fig. 2.4). The pore has a cylindrical, slightly tapered shape with one exit of 2.2 nm and the other of 1.3 nm.[79] Because of its geometry, it is suitable for ssDNA translocation. Mobile loops at the extra-cellular side entrance allow a pH driven gating of the nanopore, which is fully reversible.[80] Therefore, OmpG is a promising candidate for nanosensors.[81]

2.2.3 Solid-State Nanopores

One of the biggest advantages of biological nanopores, the high reproducibility of dimension with atomic precision can also be a disadvantage at the same time. The lack of freedom to tune the pore size and geometry as well as the limited stability of the lipid membrane, in which the pores are embedded, puts limitations to the versatility of their use. The experimental parameters are often dominated by required conditions of the lipid bilayer such as pH, temperature and salt concentration. At this point, fabrication of artificial solid-state nanopores in insulating membranes has been introduced to circumvent these limitations of biological setups.

Solid-state nanopores and their membranesystems offer several advantages such as tuning pore size and shape, advanced mechanical properties, chemical resistance and adjustable surface properties. Fabrication of solid-state nanopores can also be performed in advance as they are easy to store. A common technique in preparation of solid-state nanopores was first accomplished in 2001, when ion beam sculpting was

introduced to fabricate nanopores in thin silicon nitride membranes with nanometer precision.[29] Furthermore, silicon nitride is a very well known material, since its use in microelectronics for about fifty years. Nanopore milling with ion[82] or electron beam construction[24] comes with the advantage of feedback from the detectors in the device. Signals of transmitting ions or electrons indicate when to stop the milling. Even fine-tuning of the pore size and geometry is possible, due to shrinking processes, depending on the ion rate and temperature. This results in a high degree of control over the final pore dimensions with subnanometer control and with diameters as small as 1 nm.[59]

A more recently development is the fabrication of nanopores by electric breakdown of the membrane material by applying a constant potential to the membrane material.[83] Successful nanopore creation is indicated by an abrupt increase of the current signal. For fabrication of the first generation of solid-state nanopores, a thin layer of Si_3N_4 was deposited on a silicon substrate by chemical vapor deposition. By photolithography and wet chemical etching of the silicon, a small free-standing membrane of Si_3N_4 was created, supported on a silicon frame. These membranes had a size of $25 \times 25\,\mu m^2$ with a typical thickness of 500 nm.[29]
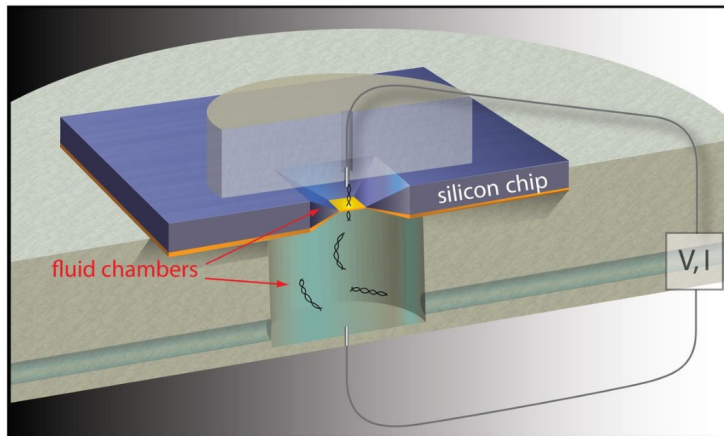
Figure 2.6: Schematic of a Si-Si_3N_4-chip, mounted for nanopore sensing purposes. An etched funnel of conical shape clears a free-standing area of the 10 nm thick Si_3N_4-membrane (orange) in which a 5 to 100 nm nanopore was drilled by ion beam sculpting. DNA molecules are threaded through the nanopore under a voltage bias. Small channels provide access to the fluid chambers.[84]

Sample holders for electron microscopy of similar dimensions are commercial available and allow many researcher easy access to nanopores, as these chips are laboratory consumables at low costs (Fig. 2.6). But when it comes to high resolution of nano-sensing, shorter nanopores and thus, thinner membranes are essential. Though, Si_3N_4

chips are mechanical stable down to a membrane thickness of about $10\,nm$, creation of ultrathin nanopores within atomically thin membranes made from 2-dimensional material is more desirable.

First studies of these atomically thin materials were investigating graphene,[85] a monolayer of graphite which is just a single layer of carbon atoms arranged in a hexagonal lattice.[86] Further 2D-materials have recently been proven to be feasible, including boron nitride,[27] hafnium oxide,[87] and molybdenum disulfide.[26]

The great advantage of ultrathin 2D-materials for nanopore sensing lies in their thickness, which is significant for resolution in any translocation experiment. Membranes made of graphen exhibit similar dimensions comparable to the spacing between DNA bases. Current modulations of DNA molecules, passing through the nanopore, may be the result of a single base interaction with the pore. This leads to a superb spatial resolution of biological molecules, and studies of dsDNA detection in graphene nanopores with resistive pulse sensing techniques have been published.[88]

Aside solid-state nanopores made from 2D-materials, shrinking on glass nanocapillaries with diameters ranging from 75 to $14\,nm$[68] and DNA origami, used for the formation of nanopores in insulating materials[89] have been developed.

2.3 Reference Electrodes

In the field of nanopore sensing, electric conductivity has become the most common parameter to analyze processes of translocation or estimation of the nanopore size.[90] For experimental measurement of the electric conductivity, electrodes are used to provide current through aqueous solutions, which generally contain the nanopore in a Coulter counter setup.

From the point of electrochemistry, the centerpiece of a classical reference electrode is a reversible chemical reaction at the electrode surface and a stable electrolytic contact to the analyte. Reaching the equilibrium of that reversible reaction results in a distinct and stable electrode potential.[91] An ideal electrode should show the following properties: (1) it should be reversible and obey the *Nernst equation* (Eq. 2.1) with respect to some species in the electrolyte, (2) its potential should be stable with time, (3) its potential should return to its initial value after small currents are passed through the electrode (no hysteresis), (4) if it is an elctrode of the second kind (e.g. Ag/AgCl), the solid phase must not be appreciably soluble in the electrolyt, and (5) it should show low hysteresis with temperature cycling.[92]
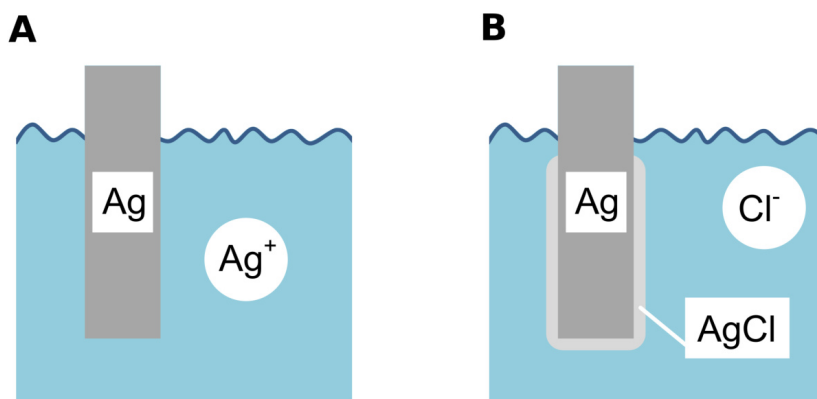
A　　　　　　　　　　**B**

Figure 2.7: (A) Schematic description of the silver electrode as an example for an electrode of the first kind. (B) The silver-silver chloride electrode is extended by a layer of silverchloride and is therefore an electrode of the second kind. Inspired by a Figure in *Reference electrodes: Theory and practice.*[93]

A simple metal electrode surrounded by its cations dissolved in an electrolyte is called an *electrode of the first kind.* The potential of this electrode is dependent on the concentration of the surrounding cations and therefore variable.[94] An *electrode of the second kind* results, when a simple metal electrode is coupled to a precipitation equilibrium of a metal salt and the presence of a salt containing the same anion like the metal salt.[95, 96]

The Ag/AgCl electrode (Fig. 2.7) is complying all the specifications of a reference electrode and is one of the most reproducible and reliable reference electrodes, it is therefore commonly used in electrochemical measurements.[97] The centerpiece of the Ag/AgCl electrode is a silver wire, which is coated with silver chloride ($AgCl_2$) and then immersed into a saturated potassium chloride (KCl) solution, typically $3.5\,\text{M}$. The silver wire and its surrounding electrolyte is generally contained in a glass tube with either a porous glass frit or an agarose gel bridge at the tip to allow ion exchange at the experimental setup.[98] Because the Ag/AgCl electrode is a second kind electrode, there is a precipitation reaction additional to the ion transfer reaction as follows:

$$(1) \quad \text{ion-transfer reaction:} \qquad \text{Ag} \rightleftharpoons \text{Ag}^+ + \text{e}^-$$

$$(2) \quad \text{precipitation:} \qquad \text{Ag}^+ + \text{Cl}^- \rightleftharpoons \text{AgCl}\downarrow$$

$$(3) \quad \text{net reaction:} \qquad \text{Ag} + \text{Cl}^- \rightleftharpoons \text{AgCl}\downarrow + \text{e}^-$$

Under equilibrium conditions of an electron-transfer process, where n is the number of electrons transferred in the cell reaction, undergoing reduction and oxidation, the

Nernst equation is an equation that relates the reduction potential E_{eq} of an electrochemical reaction to the standard electrode potential E^0, universal gas constant R, temperature T, Faraday constant F, and activities of the chemical species (a_{Ox}, a_{Red})[99] and is given by:

$$E_{eq} = E^0 + \frac{RT}{nF} \ln \frac{a_{Ox}}{a_{Red}} \tag{2.1}$$

Though the electrode of the Ag/AgCl electrode is coated with $AgCl_2$, the electrode itself is of pure silver, therefore, chemical activity is set to 1 $(a_{Red} = 1)$.[100] The electrode potential is then given by:

$$E_{eq} = E^0 + \frac{RT}{nF} \ln a_{Ox} \tag{2.2}$$

On the other hand, the activity of the silver ions in the saturated solution depends on the solubility equilibrium, and the activity of the silver ions is given by the solubility product K_{sp} as the following:

$$a_{Ag^+} = \frac{K_{sp}}{a_{Cl^-}} \tag{2.3}$$

This results in the following Nernst equation, where the electrode potential only depends on the activity of the chloride ions in the electrolyte solution:

$$E_{eq} = E^0 + \frac{RT}{nF} \ln \frac{K_{sp}}{a_{Cl^-}} \tag{2.4}$$

If Ag^+ ions are formed during a current by operating the Ag/AgCl electrode, the solubility product is exceeded by the superior number of Cl^- ions present, and solid AgCl will precipitate. Conversely, if metallic silver were deposited from silver ions, Ag^+ ions could immediately re-dissolve and be supplemented by a small amount of solid AgCl. However, the Cl^- ions which simultaneously dissolve do not practically change the total concentration since they are already of very high concentration (3.5 M KCl). As a result, the Cl^- ion concentration, and thus, the chemical activity remains practically constant. The constant Ag^+ ion concentration thus ensures a constant reference potential of the measuring electrode.[96]

2.4 Langmuir-Blodgett Films

2.4.1 Historical Development

The discovery and history of Langmuir-Blodgett films could be a prime example, how research often tends to begin. In 1757, B. Franklin was a member of an expedition

of 96 ships against Louisburg, which was a french fortress in today's Canada. He observed the backwash of two of the ships to be remarkably smooth, while all the others were ruffled by the wind. He was puzzled with the different appearance and asked the captain the meaning of that observation. It turned out that the cooks had just emptied greasy water through the scuppers, which had greased the side of those ships and the surrounding water.

When he decided to make experiments of his own, he observed the droplet of oil to spread on the water with surprising swiftness upon the surface. He assumed a very thin layer of oil, since he noticed prismatic colors of the film, and a large widespread area for very small amounts of oil. He supposed the particles to be repulsive, that way they spread very fast and to a large amount of area.[101]

His publication led to a discussion that every ship should carry supplies of oil for pouring on stormy seas. It was then J. Aitken in 1882, who took further experiments on thin layers of oil on water. In a circular vessel he arranged that a jet of air should blow over the surface and caused it to take up a rotary motion. This motion was measured by hanging a completely submerged horizontal paddle in the middle of the vessel. A needle, rigidly attached to the paddle, measured on a circular scale the amount of torsion produced by the moving water.[102] Unfortunately, the experiments found to be contradicting to the theory of wave-damping by oil.[103]

Shortly after that, J. W. Strutt, better known as Lord Rayleigh, performed experiments with layers of olive oil and their effect on surface tension. He estimated the film thickness of 1 to 2 nm, but was not able to find a precise method to take an exact measurement.[104] This would have been the first direct measurement of the size of an organic molecule.[102]

The science of monolayers reached a next level, when A. Pockels send a letter to Lord Rayleigh in 1891. She described her use of a rectangular tin trough, filled with water to perform experiments on surface tension on an oil-contaminated surface. She established the methods which have remained to this day the essentials of monolayer research.[102] With recommendation of Lord Rayleigh, her work was published in the journal *Nature* and the very first pressure-area diagram is shown.[105] Her data of the molecular area of stearic acid was correct in the order of one magnitude.[106]

It was then I. Langmuir, who followed the theory of Rayleigh about layers of oil being only one molecule thick. Though his work was largely carried out independently of the earlier investigators, he gave generous acknowledgement to Pockels and Rayleigh and commented on the apparent neglect of their method and conclusions during the first two

decades of the 19th century.[102] He developed a film balance for monolayer preparation, which is associated with his name until today. A movable barrier is separating clean water from the water covered by a molecular film. With the deflection of a float, changes in the surface tension could be measured.

However, Langmuir's greatest achievement was that he confirmed his films to be of only one molecule in thickness and that they are orientated on the surface of water, with the polar group immersed in the water and the long nonpolar chains directed almost vertically from the surface. Based on a publication on the chemistry of oil films,[107] he received the Nobel Prize in chemistry in 1932. In 1919, under Langmuir's guidance at the research staff of General Electric Company, K. Blodgett was able to transfer fatty acid monolayers from the air-water interface to solid substrates for the first time, though it was published not until 1935.[108] This gave birth to the modern term of *Langmuir-Blodgett transfer*.

2.4.2 Surface Tension

Surface tension is the cause of many phenomena that can be observed in nature. It causes the surface of a liquid to behave like a stretched elastic film. Some insects are able to walk across the water, a coin seems to float on the water and it causes water to form droplets.

The term of *surface* only makes sense, when there are two different phases involved that are separated by the surface. A two-phase system of water is defined as equilibrium between a condensed (liquid or solid) phase and its vapor. The interphase is then defined as the thin section between the two phases, in which properties like density smoothly converge.[109] Because forces between uncharged molecules are only relevant at short ranges, this layer is no more then of one or two molecular diameters.[110] It follows that this interphase can be considered as infinitely thin and is known as the *interface* or *surface*.

Due to attractive forces in the bulk of a liquid, the potential energy of a molecule is reduced by bonds to neighboring molecules. These intermolecular forces act to stabilize the system by reducing the total potential energy.[109] Such forces give rise to *cohesion* among the molecules of a liquid.[111] However, at the air-water interface, a molecule is surrounded by fewer molecules than one in the bulk liquid. Therefore, they exhibit a higher potential energy than those in the bulk of the liquid. In other words, to transfer a molecule from the bulk to the surface, work is necessary. Hence, it requires work, to expand the surface area of the liquid.

Formally, the surface tension γ represents the amount of work necessary to increase the surface of a liquid per unit area:

$$\gamma = \frac{\delta W}{\delta A} \tag{2.5}$$

The surface tension of water is $72.8\,\mathrm{mN\,m^{-1}}$ at $20\,°C$[110] and is considered high, compared to that of most other liquids, due to the relatively high attraction of water molecules to each other through a network of hydrogen bonds (ethanol: $22.3\,\mathrm{mN\,m^{-1}}$ at $20\,°C$, glycerol: $63.0\,\mathrm{mN\,m^{-1}}$ at $20\,°C$).[112]

With increasing temperature, the kinetic energy of the water molecules rise. Intermolecular bonds are weakened and surface tension is decreased in general. It becomes zero at the critical point.[113] The SI unit for the surface tension is a force per length (Nm^{-1}) which manifests itself as energy per area.
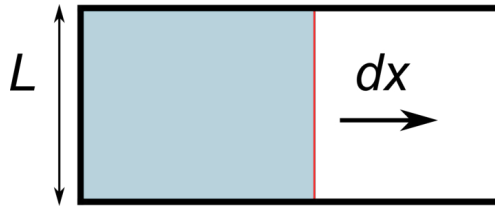

Figure 2.8: A thin layer of liquid is clamped in a frame like a flat bubble. A force is necessary to move the red bar to enlarge the surface area of the enclosed liquid.

The equality of *force per unit length* on the one hand, and *energy per unit area* on the other hand can be proved by a simple experiment. If a liquid is restrained to an area of certain size (similar to a soap film in a toy bubble blower loop), like in a frame (Fig. 2.8), a force is needed to enlarge the area. This force is proportional to the surface tension γ as well as to the increase in area, that is, to L. However, to understand the surface tension as an *energy per area* is much more intuitive. That way, it represents the amount of energy that is necessary to increase the surface.

$$\gamma = \frac{\delta W}{\delta A} = \frac{F\,\mathrm{d}x}{L\,\mathrm{d}x} = \frac{F}{L} \tag{2.6}$$

In accordance with the principle that every system moves towards a state of minimum potential energy, if free to do so, the surface of a liquid shows a tendency to be minimized. The smallest surface area for a given mass of water is that of a sphere. This explains the formation of spherical droplets in the rain and in zero gravity. Any other

shape would represent a larger surface area and thus a higher energy content.[111]
Surface tension is commonly measured by the *Wilhelmy plate* technique. A rectangular plate, often made of filter paper or platinum, is submerged into the liquid (Fig. 2.9). The plate is attached to a sensitive microbalance by a wire. For the plate dimensions of h_0, w and t and material of density ρ_p immersed to a depth h in a liquid of density ρ_l, the net downward force F is given by:

$$
\begin{aligned}
F &= (\rho_p h_0 w t) \cdot g &-& (\rho_l h w t) \cdot g &+& 2\gamma \cdot (w + t) \cdot cos\theta \\
&= \text{gravity} &-& \text{buoyancy} &+& \text{surface tension}
\end{aligned}
$$

where γ is the surface tension of the liquid, θ is the contact angle on the Wilhelmy plate and g is the gravity acceleration. Under ideal conditions, the plate is fully wetted, that is, the contact angle is zero ($\theta = 0$). For a stationary plate, the change in force ΔF is then related to the change in surface tension $\Delta\gamma$ by:

$$
\Delta\gamma = \frac{\Delta F}{2(t + w)} \quad \overset{t \ll w}{=\!=\!\Rightarrow} \quad \Delta\gamma = \frac{\Delta F}{2w} \tag{2.7}
$$
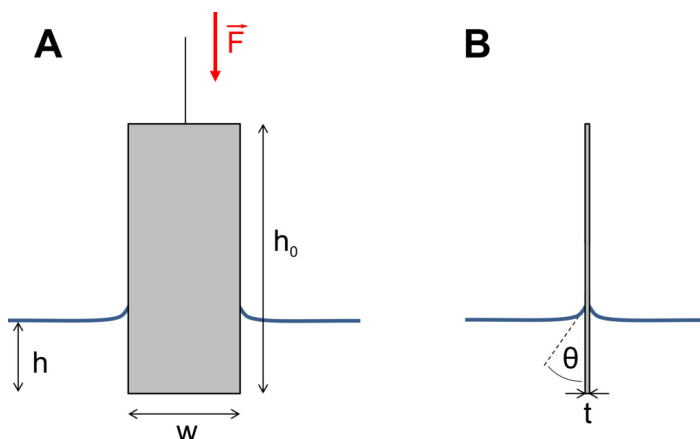
Figure 2.9: The surface tension of a liquid is measured by a Wilhelmy plate. It is partially submerged into a liquid. Front (A) and side (B) view.

2.4.3 Monolayers at the Air-Water Interface

It was one of the first observations that even small amounts of oil spread to water on a large area. There seems to be a force for the molecules to spread throughout the entire water surface. The origin of that force lies in their chemical composition. A typical monolayer-forming material has two distinct regions within the molecule.

The first contains a hydrophilic group, attracted to water, which is easily soluble in water. The second region contains a hydrophobic group, which is generally nonpolar and is seemingly repelled from water. Strictly speaking, it is more of an absence of attraction. Inserting it into water would break up the local hydrogen-bonding forces and is therefore energetically unfavorable. In turn, functional groups with hydrophilic character are typically charge-polarized and capable of hydrogen bonding. A molecule with both functional groups is known as an amphiphile (*amphis*: both, *philia*: love).
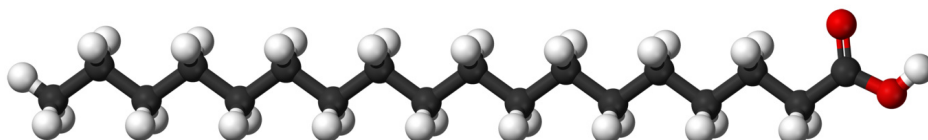

Figure 2.10: Modell of stearic acid. The two red balls are representing the oxygen molecules of the carboxyl group. It contains 18 carbon atoms and has a total length of ≈ 2.5 nm and a crosssection of about 0.19 nm.[110]

A commonly used amphiphilic monolayer-forming material is stearic acid, which is one of a series of long chain fatty acids, with the general chemical formula $C_nH_{2n+1}COOH$. In this group of molecules, a hydrophilic carboxylic group (-COOH) is attached to a long alkyl chain, which provides a hydrophobic character (Fig. 2.10). The molecule has a cylindrical shape with a length of approximately 2.5 nm and a cross section of about 0.19 nm.[110] Whether a functional group has a hydrophilic character is generally associated with their dipole moment, examples are given in Table 2.1.

It should be noted, that the solubility of an amphiphilic molecule in water also depends on the balance between the alkyl chain length and the strength of its hydrophilic head. For example, while hexadecanoic acid (palmitic acid) forms stable Langmuir films, hexadecyl-trimethyl-ammonium chloride (cetrimonium chloride) is too soluble in water to allow the formation of a monolayer,[114] although their alkyl chain is of the same length.

Chemical group	Dipole moment [D]	Chemical group	Dipole moment [D]
H_2O (for comparison)	1.85	COOH	1.75
OH	1.68	NO_2	3.66
NH_2	1.17	C_6H_6	0
cis C=C	0.33	*trans* C=C	0

Table 2.1: Dipole moments of relevant chemical groups, attached to an alkyl chain[110]

Before application of stearic acid molecules to a water surface, the lipids must first be dissolved in a water-immiscible solvent such as chloroform, benzene or diethyl ether. The solution is then dropwise put to the air-water interface and it spreads rapidly to cover the available area. As the solvent evaporates, the molecules of stearic acid align to the surface. According to their amphiphilic character, the headgroup is facing to the water, while the hydrophobic tale remains outside. This is illustrated in Fig. 2.11. It usually is assumed that the first one or two methylene groups are also submerged to water. This can be justified easily based on water solubilities of carboxylic acids; for example, propanoic acid (CH_3CH_2COOH) is soluble in water.[114]

Figure 2.11: Amphiphile molecules at the air-water interface in the expanded, compressed, and closed packed state. These states are also referred to as *gaseous*, *liquid*, and *solid* in analogy to thermodynamics. Inspired by a Figure in *Langmuir-Blodgett Films*.[102]

The potential energy of water molecules at the air-water interface, now covered by a monolayer of amphiphiles, is highly reduced by bonds to neighboring amphiphilic molecules. Thus, the energetic difference between water molecules in the bulk liquid and at the surface is also reduced, and consequently, the surface tension is reduced. The amount of amphiphilic molecules per unit area has a great influence on the extent of surface tension reduction.

In the *expanded phase*, which will later be referred to as the *gaseous phase*, the molecules are far apart and their interactions are small. Under these conditions the surface tension of water is hardly affected. When the area of the monolayer is reduced, repulsive forces arise between the amphiphilic molecules creating a kind of two-dimensional pressure.

In analogy to thermodynamics, this pressure is called the *surface pressure*. It is defined as follows:

$$\pi = \gamma - \gamma_0 \tag{2.8}$$

where γ_0 is the surface tension of the monolayer-covered water surface and γ is that of pure water at the same temperature.

2.4.4 Two Dimensional Thermodynamics

Molecules at the air-water interface are free to diffuse randomly and they spread apart in order to homogeneously distribute themselves throughout any area. Because they are far apart, their interactions are small. It takes comparatively little force to move the molecules closer together and their size is neglectable in comparison to the intermolecular distance.
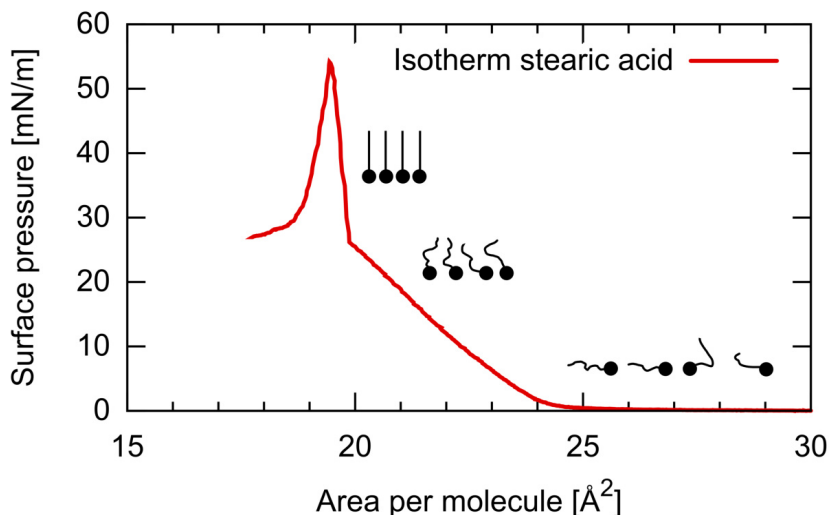

Figure 2.12: Surface pressure versus area per molecule isotherm for stearic acid at 20 °C. Water is used as a subphase with pH 7. Different phases are easily identifiable by their specific slope.

These properties are similar to those of the gaseous state of thermodynamics. The term surface *pressure* is also based on thermodynamics. Because of these fundamental similarities, monolayers at the air-water interface will obey the ideal gas law in the form of $\pi A = k_B T$, where A is the area per molecule, π is the surface pressure, k_B is the Boltzmann constant and T is the absolute temperature. For the physics of Langmuir films, A is equivalent to VN^{-1} and π is equivalent to p in the original ideal gas law. If π is measured in $[\mathrm{mN\,m^{-1}}]$ and A in $[\mathrm{\mathring{A}^2\ molecule^{-1}}]$, their product should be $40.5\,\mathrm{m^2\,kg\,s^{-2}}$ at 20 °C. Therefore, the surface pressure in the gaseous phase would be expected to be about $1\,\mathrm{mN\,m^{-1}}$ at an area per molecule of $40.5\,\mathrm{\mathring{A}^2}$. This is in good agreement with experimental parameters of typical long-chain amphiphilic molecules.[110] However, the most interesting analogy is the characteristic isotherm of a monolayer and a gas, while getting compressed. An isotherm of a monolayer is measured by recording the surface pressure and the area of the monolayer while it gets continuously compressed by a moving barrier at a constant temperature.

Like for isotherms of real gases, many amphiphiles show distinct characteristic points in their isotherm, where the slope increases abruptly. The *gaseous phase* is the first section, which is characterized by an extremely low surface pressure. Molecules of the monolayer ideally show no interaction with each other. In the case of stearic acid (Fig. 2.12), each molecule takes only about $50\,\text{Å}^2$ and the surface pressure is less then $0.5\,\text{mN}\,\text{m}^{-1}$, thus this part of the isotherm is often not resolved by the apparatus.

As the area is further compressed, the intermolecular distance decreases. For stearic acid, a phase transition can be observed at around $24\,\text{Å}^2$ in the isotherm.[114] This first phase transition from gaseous to *liquid state* is characterized by a significant increase in surface pressure. In the liquid state, the alkyl chains of the amphiphiles are becoming more coherent. The hydrophobic chains, which were originally distributed near the water surface, are being lifted away.

By further film compression, a second phase transition can be observed, from the liquid to the *solid state*. At this stage, the area per molecule is around $20\,\text{Å}^2$ for stearic acid.[102] In this confirmation, the molecules are closely packed and uniformly orientated. The area per molecule is close to their spatial chemical confirmation. The compressibility, which is the reciprocal of tangential slope of the isotherm, is constant in this state. Thus, the slope is linear and about 10 times higher compared to the liquid state phase in accordance with classical thermodynamics. If this second linear section of the isotherm is extrapolated to zero surface pressure, the intercept gives the area per stearic acid molecule that would be expected for the hypothetical state of an uncompressed close-packed layer. This value of $22\,\text{Å}^2$ per molecule is close to that occupied by stearic acid molecules in single crystals, thus confirming the interpretation of a compact film as a two-dimensional solid.[102]

Especially in the solid state phase of the isotherm, compression speed takes a great influence on the shape of the isotherm, because of the incompressibility of the monolayer in this state.[115]

At even smaller surface areas, the film collapses due to mechanical instability.[116] The rise of surface pressure stops and eventually decreases. The onset of collapse depends on experimental parameter like rate of compression, pH or temperature[114] and is highly characteristic of the monolayer material used. Mechanical stress promotes molecular layers to ride on top of each (Fig. 2.13), forming an unordered multilayer, and partial dissolution of the film material to the subphase occurs. Finally, three-dimensional structures of amphiphiles in the form of vesicles and micelles are formed, which dissolve in the subphase.
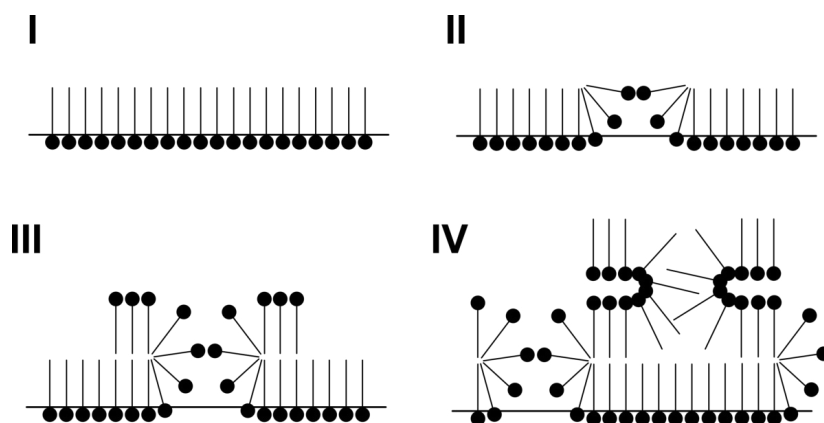
Figure 2.13: The stages of a collapse of a monolayer at the air-water interface. As the area per molecule becomes smaller than the molecular area of the amphiphile, the film begins to spread randomly to further layers. Inspired by a Figure in *Langmuir-Blodgett Films.*[102]

However, partial collapse of the monolayer can occur in the solid state phase before reaching the actual collapse point. This becomes visible, when a monolayer is kept at a certain high surface pressure and the occupied molecular area is relaxed over time.[115] Overall, stearic acid shows three distinct sections along its isotherm (20 °C), characterized by their different slopes, and thus can be clearly assigned to the three phases. However, this behavior is actually not consistent with thermodynamics of real gases, where subcritical isotherms show phase transitions with a constant pressure region (phase coexistence region), which is characteristic for a *first-order* thermodynamic transition like melting or condensing. Instead, the sudden increase in the slope of many Langmuir isotherms (like stearic acid) is characteristic for a *second-order* phase transition. There, the phase transition is the final step of constant and collective tilting of the molecules in the present phase. Whereas the first-order phase transition is associated with the formation and growth of nuclei consisting of molecules of higher order.[117]

Superconductivity is a prominent example of another second-order phase transition, when cooled below a characteristic critical temperature.

If a floating monolayer film at the air-water interface consists of a mixture of two phases, visualization can be realized with Brewster angle microscopy.[118,119] By fluorescence microscopy[120,121] it was revealed that islands of the so called *liquid condensed* (LC) phase are dispersed in a phase that is called *liquid expanded* (LE). It takes place through the formation of a two-dimensional microemulsion of the new phase (LC) in the old one (LE), with the islands of the microemulsion organized as a superlattice.[122]

Figure 2.14: The pictures show a Langmuir film from the top view. A fluorophore (Texas Red) is conjugated to the headgroups of lipids in the Langmuir film and is distributed homogeneously (LE). During phase coexistence (LE/LC), the dye is excluded from the more-ordered LC phase, thus generating a contrast between the phases.[123]

In fluorescence microscopy experiments (Fig. 2.14), distinct phases of LE and LC become visible by using a water-soluble dye in the subphase which preferentially adsorbs into less-ordered monolayer domains, where it provides quantifiable contrast in confocal microscopy. This is an advance over fluorescently tagged lipids, which are not water-soluble and cannot leave the interface. This leads to a high concentration of tagged lipids in high density areas and therefore, fluorescence quenching and change in domain shape is happening.[123]
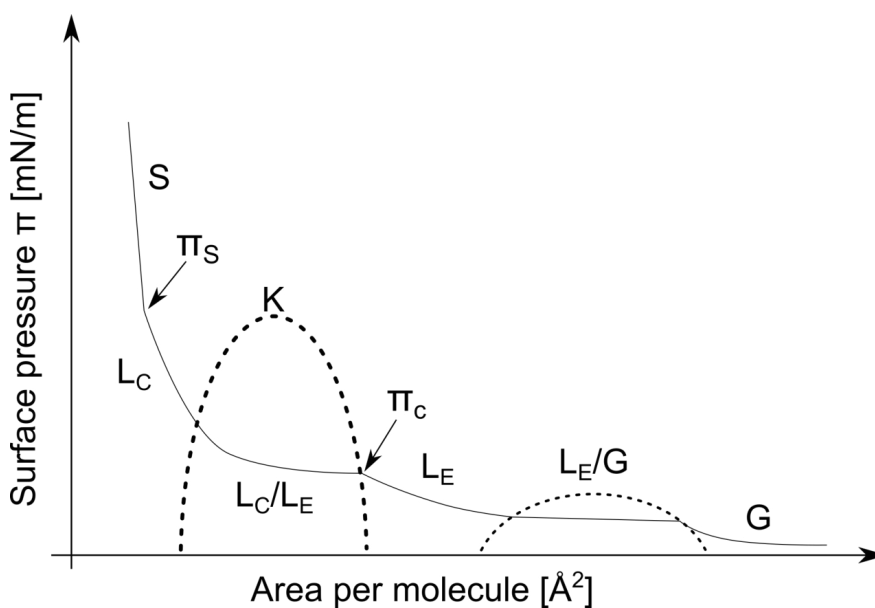

Figure 2.15: Isotherm with several visible phase transitions, partly with horizontal plateau. The dashed lines are representing the coexistence (K) ranges of the liquid expanded (LE) and liquid condensed (LC) phases, and of the LE and gaseous (G) phases. Inspired by a Figure in *Mohwald et al.*[124]

A schematic isotherm containing all of the possible phases and their transitions is shown in Fig. 2.15. Each phase transition is characterized by a kink in the beginning, followed by either a nearly horizontal or inclined chart.[125]

After the gaseous (G) phase, a first phase transition to the liquid expanded (LE) phase occurs. The surface pressure of the gaseous phase and its transition to the LE phase is often too low to be measured with most devices. After the phase coexistence (LE/G), the LE region follows. Starting with a kink at π_C, the second phase transition of the isotherm from the LE phase to the liquid condensed (LC) phase is in progress.[122] The area enclosed by the dashed line is representing the *coexistence range* with the critical point K. At temperatures above the critical point, the isotherm shows no phase coexistence area, comparable to classic thermodynamics.

Though both, the LE and LC phases, are considered analogues of the liquid phase in thermodynamics, they differ in their structure from each other. The LE phase corresponds to the fluid phase of bilayer membranes in biological cells, where lipid molecules diffuse freely within this plane. Thus, like in a fluid bilayer, a given lipid will rapidly exchange locations and migrate over long distances within the LE phase. In contrast to the situation with lipid bilayers, however, the two-dimensional density in this phase can be varied to a large extent, while the orientation of polar groups does not appear to vary.[124]

"In contrast, the LC phase is characterized by short range positional ($\sim 100\,\text{Å}$) and long range orientational ($\sim 100\,\mu\text{m}$) order. The mass density in the hydrocarbon phase is identical within 1–$3\,\%$ to that of lamellar alkane phases with low density of kink defects, and the chain tilt is uniform."[124]

After the coexistence of LC and LE phases (Fig. 2.15), the isotherm proceeds in the LC phase to reach the point of π_S, where a third phase transition to the solid (S) phase occurs. This final transition is characterized by a kink (π_S) followed by a linear part of the isotherm. In the solid state regime, the monolayer parameters like molecular area and compressibility are comparable to single crystals, thus confirming the interpretation of a compact film as a two-dimensional solid.[102]

Isotherms of 1,2-bis(10,12-tricosadiynoyl)-sn-glycero-3-phosphocholine (DiynePC) are shown in Fig. 2.16 at $16\,^\circ\text{C}$ and $23\,^\circ\text{C}$, respectively. At $16\,^\circ\text{C}$, the isotherm shows a direct transition from a gaseous phase to a liquid condensed phase, whereas at $23\,^\circ\text{C}$ a coexistence plateau between an expanded phase and the condensed phase is observed. The surface pressure of the plateau varies within the coexistance range (dashed lines in Fig. 2.15) depending on the temperature, but also on the molecular structure. In

general, a decrease in the hydrocarbon chain length produces an increase in the surface pressure of the phase change plateau. An increase in temperature produces a similar result. These effects are a result of the forces between the molecules in the monolayer. A shorter alkyl chain leads to decreasing van der Waals forces between the molecules, resulting in less cohesion within the film. Incidentally, the melting point of the bulk material decreases, too. A decrease in temperature, on the other side, leads to less thermal motion, thus the film tends to condense. As a rule of thumb, reducing the hydrocarbon chain length of a long-chain fatty acid by one methylene group is roughly equivalent to a temperature increase of 5–10 °C.[110]
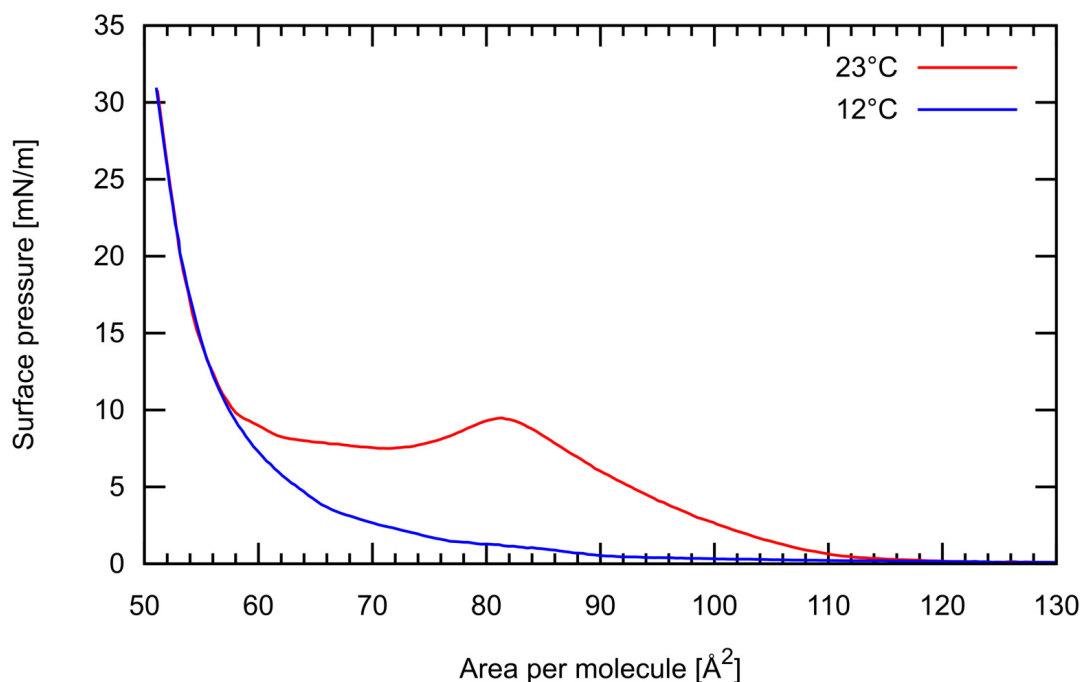

Figure 2.16: Surface pressure versus area per molecule isotherm for DiynePC at 12 °C (blue chart) and 23 °C (red chart). An overshoot at the transition between the LE and LC phase for the isotherm at 23 °C is visible.

Another important parameter in lipid layers (membranes, monolayers) is the so called *phase transition temperature* T_M, also referred to as the *melting temperature*. T_M is influenced by many factors like alkyl chain length, saturation state, the ionic conditions in the subphase or the presence of sterols. At temperatures above T_M, layers of lipids exist in the *liquid-crystaline* phase, characterized by a relatively high degree of lateral mobility of individual lipids within the layer. The hydrocarbon chains are bent and their mutual bonds are weak. At temperatures below T_M, the lipid layer exists in the *gel* phase.[126,127] The hydrocarbon chains are fully extended, that is, in the all-trans

configuration, and are aligned nearly perpendicular to the plain of the layer.[128] As a consequence there are increased van der Waals forces between lipids and reduced mobility.

In a last class of isotherms of amphiphilic monolayers, no clear phase transitions can be observed at all. The area per molecule remains at much higher values than required for close packing. After a gaseous phase, the film is believed to be arranged in the LE phase at the entire process of compression.[102] This type of isotherms is mostly typical for molecules with disruption in their hydrocarbon chain, like in the case of unsaturated fatty acids. A typical example of this behavior is shown in Fig. 2.17 for oleic acid, which is a monounsaturated omega-9 fatty acid. In the process of compression, the hydrophobic chain causes difficulties in packing, resulting in a higher value for the area per molecule compared to a all-trans configuration of the same molecule.[102]
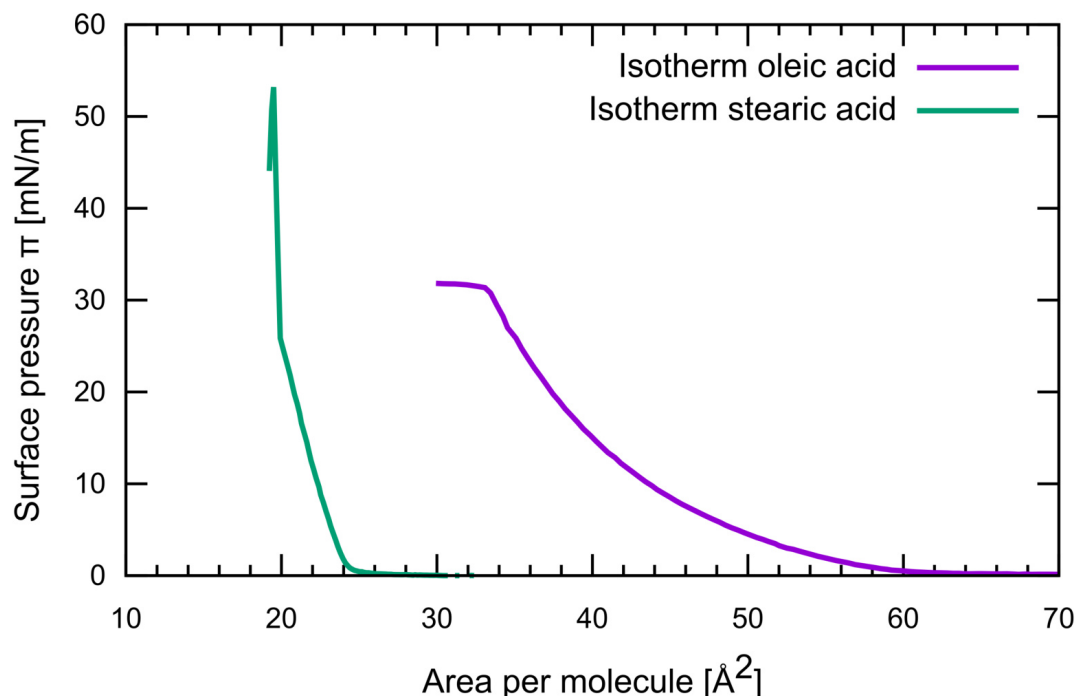

Figure 2.17: Surface pressure versus area per molecule isotherm for oleic acid, with stearic acid as a comparison. The chart of oleic acid looks similar to the isotherm of an ideal gas in thermodynamics.

2.4.5 Transfer of Langmuir Films

Experimental studies of monolayer-forming substances at the air-water interface can provide valuable information on molecular size, intermolecular forces, and chemical

properties of the material used. However, the most promising subject in this field of science is the transfer of films of molecules from the water surface to a solid substrate using various transfer techniques. In the most commonly used method, the *Langmuir-Blodgett* (LB) transfer, the vertically orientated substrate is first lowered through the monolayer at the surface into the subphase of a Langmuir-Blodgett trough and then withdrawn (Fig. 2.18). The temperature and the surface pressure is kept constant during the transfer to maintain constant conditions. For a most stable state, the film is generally in its solid phase, but this is not essential as long as it is not in an expanded (gas or LE) state.[102] The molecular arrangement in the transferred LB film will depend on these initial parameters.

Beside the LB transfer, the *Langmuir-Schaefer* (LS) technique is often used for mono-layer transfer onto hydrophobic samples. There, the sample is approached and with-drawn parallel, thus horizontally orientated, to the interface. Due to the transfer technique, the LS technique is often used for single layer transfers only.
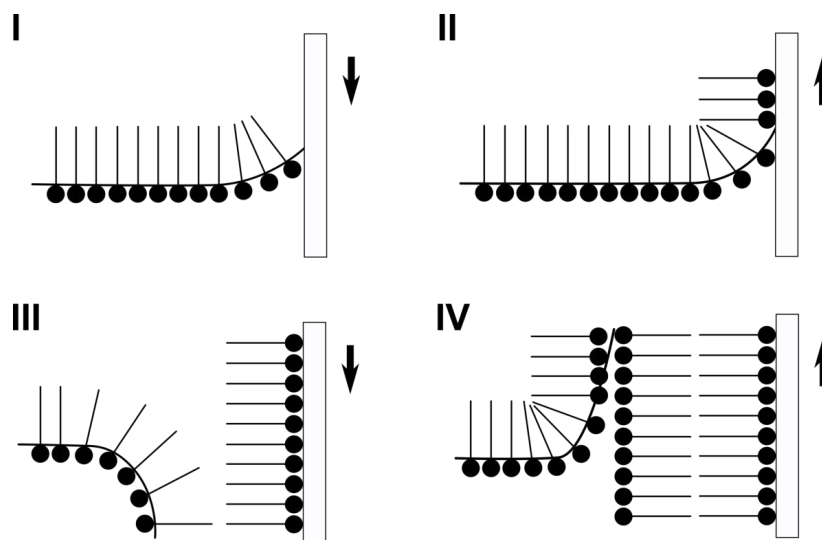

Figure 2.18: Deposition of a monolayer from the air-water interface to a substrate using the the Langmuir-Blodgett (LB) technique. A multilayer film can be obtained by multiple transfer procedures (I-IV). Inspired by a Figure in *Langmuir-Blodgett Films*.[102]

In the LB technique and the case of a hydrophilic substrate like glass, for instance, deposition follows the sequence shown in Fig. 2.18. As soon as the sample is touching the water during the first dipping, a convex meniscus forms. Due to the orientation of the monolayer molecules, there is no mechanism for deposition under ideal conditions in this phase of transfer (Fig. 2.18, step I).[110] Thus, the deposition begins at the first

withdrawal from the subphase. However, it is also possible to first place the substrate in the subphase, then spread the monolayer and finally start the process of transfer. As the substrate is then withdrawn from the subphase, the meniscus wipes across the surface of the substrate leaving a monolayer (Fig. 2.18, step II). In this setup, the headgroups of the initial amphiphilic layer face towards the hydrophilic substrate. Every further layer aligns to this initial orientation in a head-to-head and tail-to-tail configuration (Fig. 2.18, step IV). During any further immersion of the sample, the meniscus turns down, because the sample is hydrophobic. The multilayer that results is called *Y-type*.[129] Although, this is the most frequently encountered transfer, two other types of LB structures are known. In the *X-type* structure, all hydrophobic groups face to the substrate, which must be hydrophobic for this multilayer system.[129] In the case of a *Z-type*, all amphiphilic molecules face their hydrophilic groups to the hydrophilic sample.[130]
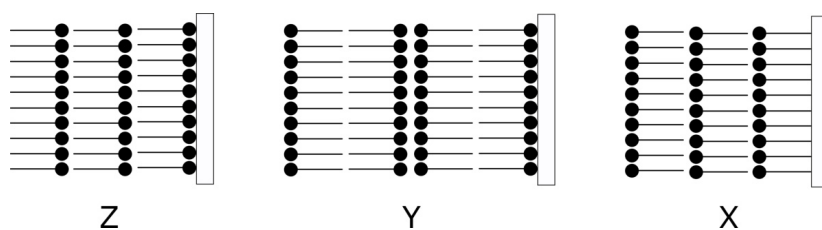

Figure 2.19: Structures of X, Y, and Z multilayers. Y-type is the most commonly used technique, while X- and Z-type require certain preparation concepts as well as suitable molecules. Inspired by a Figure in *Langmuir-Blodgett Films*.[102]

However, X-type or Z-type deposition (Fig. 2.19) often results in LB films of Y-type, depending on the deposition conditions, such as temperature, controlled surface pressure for transfer, pH and concentration of multivalent metal ion in the subphase.[114]

As for long-chain fatty acids deposition, X as well as Z-type deposition result generally in a Y-type multilayer structure.[115] Although some work about Z-types is reported for aromatic materials with relatively short or no carbon chains,[130] the Z-type is very unlike. Examples include substituted anthracene derivates,[131] porphyrins,[132] phthalocyanines and certain dye materials.[133]

Besides the transfer technique, the chemical structure of the substrate can also affect the appearance of the transferred layer. Though amphiphilic molecules are orientated vertically at the air-water interface of the Langmuir trough, they are found to be horizontally orientated after the transfer in rare cases. On graphite for instance, long-chain alkanes, alcohols and fatty acids organize in lamellae with the extended alkyl chains

oriented parallel to a lattice axis within the basal plane of the substrate.[134] Investigations by AFM[135] and STM[136] revealed a self assembling character on appropriate substrates. Domains in the transferred monolayer exhibit orientation angles, displaying the symmetry of the substrate lattice.

For all transfer techniques using the LB trough, the first layer of the transferred film becomes particularly important as it represents the initial interaction between the chemical character of the sample and the monolayer. Due to the presence of water during any transfer protocol of a monolayer to the sample, small amounts of water always remain to the transferred monolayer. For this reason, particular care is usually taken to ensure complete drying of the deposited film before further treatment.[102] On the other side, a water film can stabilize the lipid layer during the transfer by filling any kind of irregularities in the deposited monolayer. By drying the water film, the monolayer is left unsupported and may collapse and form defects.[129,137]

Rearrangements within the film due to the presence of water even after transfer is reported for amphiphilic block copolymers,[138] for Tripalmitin[139] and are reported in chpt. 4.1 in this thesis.

Deposition characteristics are often improved by adding divalent cations (e.g. Ca^{2+}, Zn^{2+}, Cd^{2+}) into the subphase.[140] At high pH values, the carboxyl group in fatty acids tends to deprotonate and the monolayer will then be a mixture of the fatty acids and its corresponding salt. In a subphase containing cadmium chloride, the following reaction will take place:

$$2\,C_nH_{2n+1}COOH + CdCl_2 \rightleftharpoons (C_nH_{2n+1}CO_2)_2^-\,Cd^{2+} + 2\,HCl \tag{2.9}$$
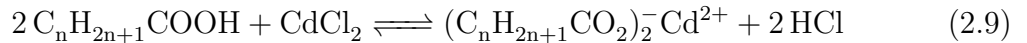
The resulting compound (e.g. cadmium distearate) is insoluble in water. The incorporation of Cd^{2+} and other doubly charged ions is also responsible for a small change in the surface area per molecule since two stearate ions are linked together by one Cd^{2+}.[102] This mixture of fatty acids and their salts converts the Langmuir monolayer into a more condensed film, as the head groups move closer together. Thus, the deposition characteristics of the monolayer are improved.[102]

The transfer speed of LB and LS transfer techniques is typically between 0.01–$1\,\mathrm{mm\,s^{-1}}$. It is mainly limited to the speed of draining water in the process of withdrawing.[102] It also depends on the dynamic properties of the monolayer at the air-water interface, that is, a highly viscous monolayer is unable to attach to a fast moving sample.[141] There is also a problem with highly rigid monolayers, polymerized at the water surface for instance. However, much faster speeds up to several $\mathrm{cm\,s^{-1}}$ is possible, once the

initial layer has been transferred.[142] The orientation of the sample with respect to the compressing barriers also has an influence on the quality of the deposited film.[143]

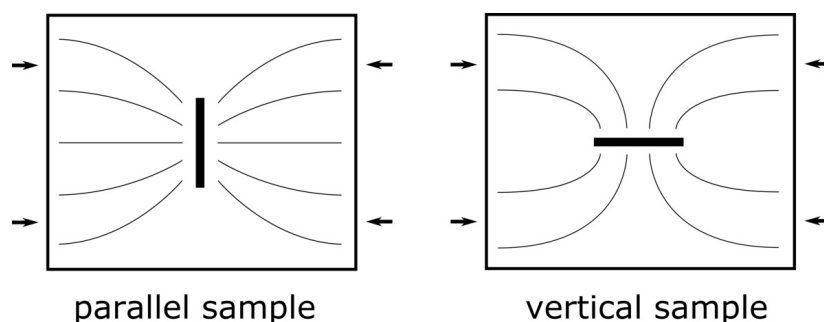parallel sample   vertical sample

Figure 2.20: Lines of motion of a monolayer during deposition of Langmuir films onto a substrate aligned either parallel or perpendicular to the direction of barrier motion. Inspired by a Figure in *Langmuir-Blodgett Films*.[102]

When the monolayer material is transferred to the sample, material has to be replenished from the surrounding air-water interface. A sample with surfaces parallel to the barriers is better supplied by the compressed film as the barriers push the film directly to the sample (Fig. 2.20). This effect increases with growing sample size.

2.5 Scanning Probe Microscopy

For a long time in the history of science, details of the surface of a sample have been achieved by a light microscope using a group of lenses to magnify features. Due to diffraction limitations of photons, electrons were introduced in the first half of the 20th century because of their shorter wavelength. The field of electron microscopy was able to discover details of nanometer scale.[144] However, imaging of the surface of a sample by particles is generally limited to very few material properties. With the development of scanning probe microscopy (SPM), it is possible to generate images of surfaces using a physical probe that scans the sample. That way, many additional material properties can be determined, including friction,[145] electrostatic forces,[146] capacitance,[147] magnetic forces,[148] conductivity,[149] viscoelasticity,[150] contact potential[151] and resistance.[152] The origins of SPM go back to the development of the scanning tunneling microscope (STM), invented in 1981 by G. Binnig and H. Rohrer, who received the Nobel Prize in Physics in 1986.[153]

STM uses a sharp metallic needle to scan over the surface at a distance of less than 1 nm. By applying of a small voltage across the tip and the sample, a tunneling current

is then used to measure and control the tip-sample distance via a feedback circuit. As an improvement to the STM technique, G. Binning, C. Quate and C. Gerber invented the atomic force microscope (AFM) in 1985 to overcome a basic drawback with STM - it can only image conducting or semiconducting surfaces. The AFM has the advantage of imaging almost any type of surface, including polymers, ceramics, composites, glass, and biological samples. The probe consists of a very sharp tip, which is ideally only of a few atoms in size. The tip is mounted to a flexible lever. This probe is guided along the surface of the sample, only a few nanometers above. Interactions of the probe with molecules or atoms of the sample of about 1 nN are used for a feedback loop to control the distance between probe and sample.[154]

With the invention of scanning probe microscopy, the large gap between the macroscopic world and single-atom sensitivity has been bridged in one step. Interactions between micro-fabricated probes and the sample allow imaging, analysis and manipulation[155] on the atomic scale.[156]

2.5.1 Atomic Force Microscope

The basic concept of an AFM is the measurement of forces between a sharp tip and a sample surface. Most commonly, the tip is mounted to the end of a flexible lever (cantilever) which serves as a force sensor. Either the static deflection of the cantilever or the change in its dynamic properties due to interactions between tip and surface can be exploited.[156] The sample is being moved relative to the cantilever in a rectangular way to create an areal scan of the sample. This is usually done by piezoelectric actuators.

To detect the small bending of the cantilever due to interacting forces, the most commonly used procedure is the beam-deflection method (Fig. 2.21).[157] Thereto, a laser beam is deflected from the rear side of the cantilever and is then monitored by a position-sensitive photodiode.[158] Though most of the interactions cause a bending in its normal direction, a four-segment photodiode also allows to detect torsion of the cantilever. Sensitivity of this detection technique is mainly limited due to the thermal noise of the cantilever.[159]

Other methods can be used to detect the cantilevers bending, like optical interferometry[160] or piezoelectric detection.[161] In the original AFM of Binning and Gerber, electron tunneling was used.[162] There, a STM tip is placed above the cantilever to detect tunneling current from the cantilever to the STM tip, which varies in dependence of the cantilevers bending.
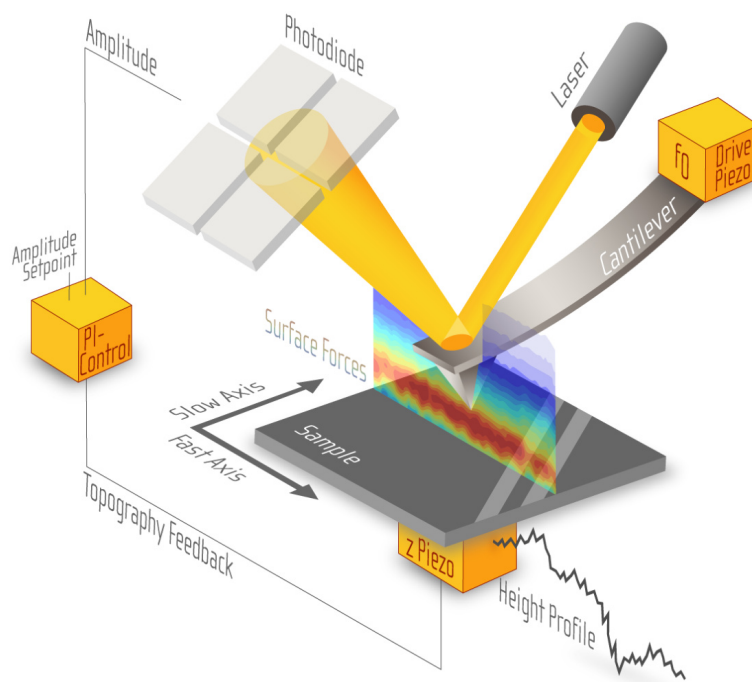
Figure 2.21: Schematic of the laser beam deflection method, used in an AFM. The cantilever deflection and torsion are measured using a four-quadrant photo diode, while the sample is scanned. The feedback system is shown by solid lines. The actual deflection signal of the photo diode is compared with the set point chosen by the user. The resulting error signal is fed into the controller, which moves the z-position of the scanner in order to minimize the deflection signal. Figure provided by N. Biere, Bielefeld University, Germany.

Detection of the cantilevers deflection is essential to control the z-position of the tip in relation to the sample. While the lateral motion of the cantilever is usually performed line-by-line, resulting in rectangular frames, the z-position is controlled by a closed-loop feedback system. In the simplest case, the difference between the actual bending of the cantilever and a preset setpoint is used to correct the tip-sample distance.

2.5.2 Forces

Two relevant force regimes must be considered, when operating an AFM tip in close contact to a surface. Short-range forces between tip and sample from the overlap of electron wave functions, resulting from the Pauli exclusion principle, which is stating that two electrons cannot occupy the same quantum state within a quantum system simultaneously.[163]

Though this kind of forces are generally repulsive, they can be attractive, when the sum of electron waves reduces the total energy (Fig. 2.22). These situations are comparable to molecular bondings. Attractive forces of this kind are in the order of 0.5–1 nN per interacting atom.[156]

The decay length of such forces is of around 0.05 nm for metallic adhesion, and 2 nm for covalent bonding.[164] Secondly, van der Waals interactions are long-range forces with dipole-dipole character. These dipoles arise from fluctuations, which generate further dipoles in their environment that are induced by the electric field of the first dipole generation.[165] They are always present and attract even chemically inert noble gas atoms. Van der Waals forces in the vacuum are in the range of 2 nN for a tip of 30 nm in radius and a tip-sample distance of 0.5 nm.[166] The medium between tip and sample has a high influence on the van der Waals forces, as they are greatly reduced, if the dielectric constant and the refractive index of the medium is close to the value of the tip and sample. For most solid materials, this is the case when immersing tip and sample in water.[156]
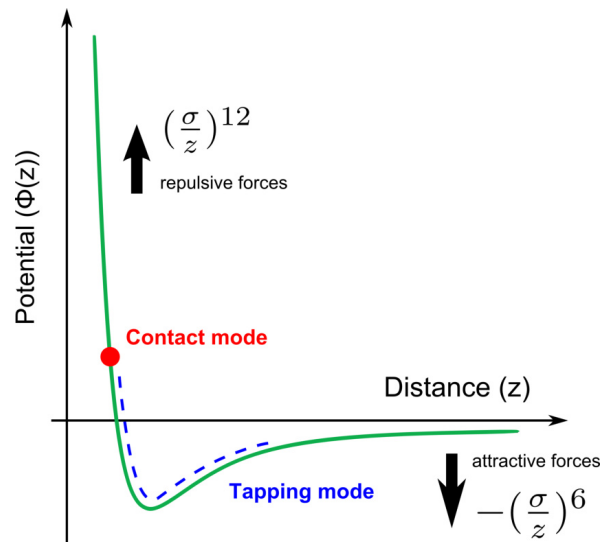

Figure 2.22: A Lennard-Jones potential. The AFM will operate in the attractive or the repulsive mode, depending on the part of the curve the AFM tip is held. Inspired by a Figure in *Merindol*.[167]

Finally, electrostatic forces can appear between localized charges on insulating tips and samples. They are very likely to occur by cleavage preparation, which is a common technique to get fresh samples of sheet-like arranged material such as graphite. Measurement in aqueous solutions with high salt concentrations are a way to reduce electrostatic repulsion, due to the shielding of ions in the water.[168]

2.5.3 Imaging Modes

The desired topographic information can be generated by a multitude of different operational modes. These can mainly be divided into static and dynamic modes. In the simplest case of a static mode, the scanner of the microscope maintains a fixed height of the cantilever. That way, the deflection of the cantilever reflects the topography of the sample. The main advantage of this *constant height* mode is high scanning speed which is only limited by the inertia of the tip.[169] As a drawback, samples must be sufficiently smooth. In *constant force* mode of operation the deflection of the cantilever is maintained by the feedback circuitry on the preset value. That way, the vertical displacement of the scanner reflects the topography of the sample. However, scanning speed is limited to the response time of the feedback system.[170] Both modes are associated with the so called *contact mode*. The sample and the tip are in physical contact and repulsive forces from the Pauli exclusion principle are dominating. Because these forces are proportional to z^{-12}, with z being the sample-tip distance, vertical resolution of contact mode is paramount and can reach values down to $0.01\,\text{nm}$,[171] mainly limited by the thermal noise of the deflection detection system.[172,173]

However, lateral resolution of AFM is largely limited by the geometry of the tip. With a tip radius of $2\,\text{nm}$, a lateral resolution of approximately $0.4\,\text{nm}$ is achievable.[172] Investigations of biological or fragile samples using the contact mode are possible, but require certain precautions due to the risk of damage.[174,175]

In the dynamic mode, the cantilever is excited to oscillate using a piezo actuator, and the tip is made to strike the surface on each oscillation. The driving frequency is usually close to the resonance frequency of the cantilever, with an amplitude of 20 to $100\,\text{nm}$.[176] Interactions of tip and sample are registered by changes of vibrational properties of the cantilever. These properties include the eigenfrequency, the oscillation amplitude and the phase between excitation and oscillation of the cantilever.[156]

A change of the resonance frequency can be measured directly in the so called frequency modulation mode (FM). The change of the resonance frequency leads to a change of the vibration amplitude and of the phase between excitation and oscillation, which can be measured in the amplitude modulation mode (AM).[177] Due to intermittent contact with the sample during measurement, this method is called *tapping mode* and was first demonstrated in 1993.[178] Through the short-time contact of sample and tip, repulsive forces dominate the acting potential and enable high resolution (Fig. 2.22).[179] Lateral forces are greatly reduced, compared to the contact mode, because drag across the surface is minimized.[156] In comparison to contact mode, less damage is done to the

sample, due to the short duration of the applied force onto the sample. In fact, tapping mode is even suitable for visualizing supported lipid bilayers in liquid medium,[180] or molecules that are weakly attached to a surface.[181]

The tapping mode generates several channels of data, that can be used to gain information about the sample. The most important channel is the topographic information, which is generated from the feedback signal. There, the perturbation on the oscillation amplitude is detected. The height variation is adjusted with the feedback to maintain the setpoint at a constant value.

Another important data channel results from the phase of the cantilevers oscillation with respect of its driving oscillator. Surface rigidity and adhesion can affect the phase shift. Therefore, the phase image is sensitive to those properties, which are not visible in the height image. It allows chemical mapping of surfaces based on such material differences.[182]

2.6 Helium Ion Microscopy

50 years ago, traditional optical microscopes gave way to new classes of alternative technologies with high magnification. Scanning electron microscopes (SEM) were developed and founded a science of microcosm with amazing imaging, offering higher resolution with longer depths of field. The image resolution was improved up to 2 nm, but has stagnated due to electron diffraction and interactions between the beam and the sample.[183] Moreover, samples require to be conductive and vacuum stable, and due to coating with heavy metal ions most biological samples lose their subtle surface features.[184]

The introduction of focused ion beam (FIB) microscopy with gallium ions[185] provided another technology for high resolution imaging, but the large mass of gallium ions causes damage to the sample or surface sputtering.

Most of the before mentioned challenges have been overcome with the development of the Helium Ion Microscope (HIM) by B. Ward.[186] HIM provides advances in charge reduction,[187] minimized sample damage, high surface contrast without the need for metal coating, increased depth of field, and 0.5 nm imaging resolution[188] of conducting, as well as uncoated insulating samples.[187] The key to the new microscope is a helium ion source of the size of only one atom (though, in most cases a source of three atoms is used, called *trimer*, for stability reasons).[189] It consists of a sharp needle that is maintanced in vacuum, cooled by liquid nitrogen. When a high voltage is applied to

the needle, an intense electric field is generated at the apex of the needle. The chance of a tunnel event of electrons in surrounding helium atoms is high.[190] Resulting positive helium ions are then accelerated in a radial way from the source. Due to a proper shape of the needle, the ionization process is taken place in the environment of just one atom, that is, the helium ion beam originates from a region less then 0.1 nm. The beam is then steered through a column of focusing, alignment and scanning elements that direct it to a probe size of 0.75 nm (Fig. 2.23).[190]
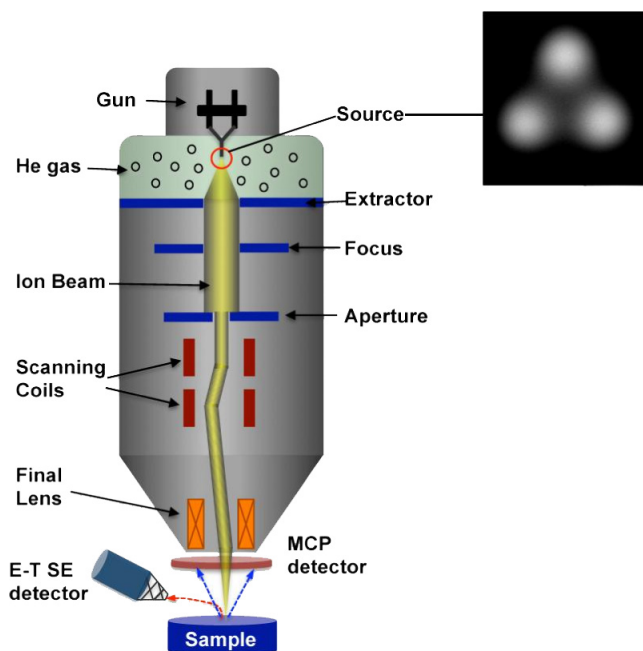

Figure 2.23: Schematic of a helium ion microscope column, showing the ion source, apertures, Everhart–Thornley secondary electron (E–T SE) detector and microchannel plate (MCP) detector configuration. (Inset) Image of atomic trimer on a tungsten tip, where ionization occurs.[191]

Like in other scanning microscopes, the beam is then scanned across the sample. Secondary electrons emitted by the sample are detected and determine the brightness value of a scanned pixel.[187]Because the number of detected electrons varies for each material or shape, HIM provide excellent topographic as well as compositional information. Compared to the microscopes mentioned earlier, the advantages of the HIM mostly arise from the properties of the element helium. Helium ions are about 7,000 times heavier than electrons, therefore, a helium ion beam exhibits very little diffraction compared to an electron beam. Consequently, when the helium ion beam strikes the sample with its larger and heavier particles, the particles do not scatter near the sur-
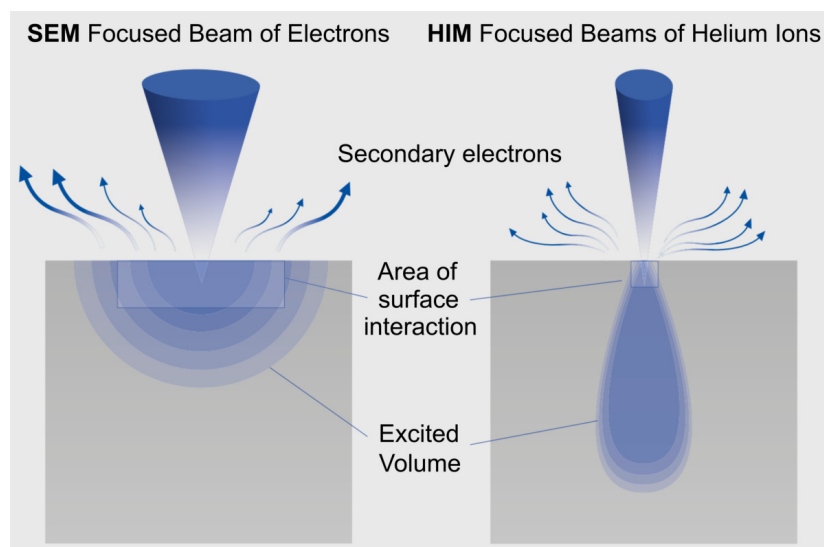
Figure 2.24: The helium ions strike the sample with larger and heavier particles, thus, the particles do not scatter near the surface. This translates into a smaller area of surface interaction and much higher resolution images for the helium ion microscope in comparison to electron microscopy.[192]

face and penetrate deeper to the sample (Fig. 2.24). This translates into a smaller interaction volume relevant for secondary electrons[183] and much higher resolution images for the helium ion microscope.[192] On the other side, helium ions are much less massive than gallium ions and sample damage or sputtering effects are less likely.

2.7 Fluorescence Microscopy

The two main parameters that are required to visually identify details are resolution and contrast. While the first is primarily defined and limited by refraction, the latter can be improved by various applications. Especially in biological microscopy, both parameters opened new access to high contrast imaging.

One of the simplest and very effective contrasting methods is dark field microscopy. It exploits the scattering of light on small particles that differ from their environment in refractive index.[193]

In the process of staining, which is another method, a proper dye can be used to stain a specific kind of tissue or cellar structure to get a colorful contrast.[194]

In phase-contrast microscopy, interaction of light with the medium causes the phase of light to change in a manner dependent on properties of the medium. Converted as

brightness variations, the phase shift becomes visible.

However, by far the most popular contrasting technique is *fluorescence*. It requires a fluorochrome, which is a molecule that absorbs light of a specific wavelength range. The re-emission then occurs with lower energy, that is, shifted to a longer wavelength.[193]

The term fluorescence was first used by G. Stokes in 1852 and was based on the mineral fluorspar, analogous to opalescence derived from opals. The generic term for fluorescence is known as luminescence. Light is emitted from a substance by relaxation of an electronically excited state. If the electron in the excited state is paired to the electron in the ground state, that is, they exhibit opposite spin, it is called a *singlet state*. Consequently, a return of the excited electron to the ground state is spin allowed and occurs on very short time scales in the order of $10\,\mathrm{ns}$.[195] However, if the excited electron has the same spin orientation as the ground state electron, it is called a *triplet state*, and transitions to the ground state S_0 are forbidden or relatively unlikely. This process is called *phosphorescence* and transitions of this kind exhibit typically a lifetime of milliseconds to seconds.

One widely encountered fluorophore is quinine, which is present in tonic water. The bright color of emergency vehicles is also caused by fluorescence.[196]
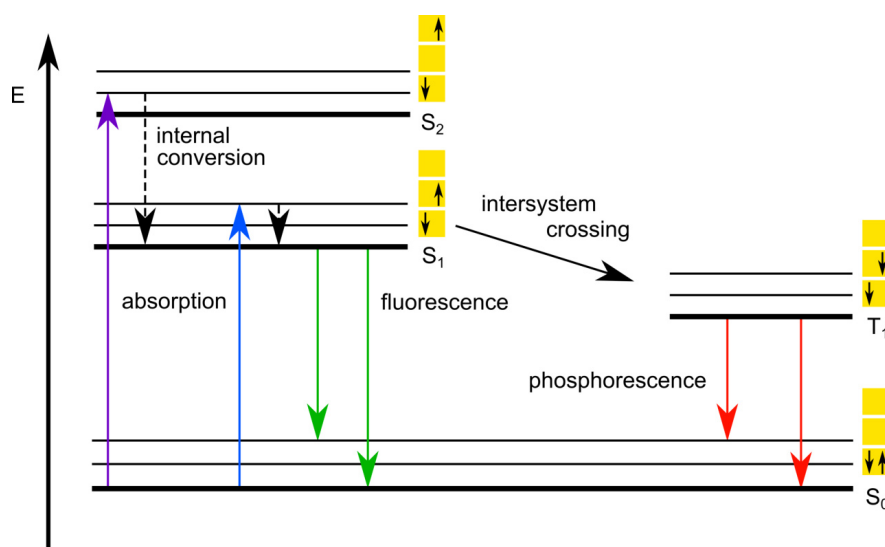

Figure 2.25: A Jablonski diagram. The color scheme illustrates the redshift between absorption and luminescence. The yellow boxes show the electron spin configuration of singlet (S_x) and triplet (T_x) state.

The process of absorption and emission of light can be illustrated by the Jablonski diagram (Fig. 2.25). The singlet first (S_0), second (S_1) and third (S_2) as well as the triplet first (T_0) and second (T_0) state represent electronic states, the fluorophore can

occupy. Each of this levels is divided into a number of subunits of vibrational energy levels. When a fluorophore in the ground state (S_0) absorbs a photon of appropriate wavelength, an electron is excited to a higher level. The molecule usually ends up in a vibrationally excited mode of the state S_1 or S_2. This step is illustrated by the purple and blue arrows in Fig. 2.25, respectively. The system will then relax to the lowest vibrational level of S_1. This process is called *internal conversion* (IC) and occurs within 10^{-12} s. Because IC occurs so much faster, fluorescence (10^{-8} s) generally occurs from the groundstate of S_1.[195] The molecule will then emit a photon by the return of an electron from the vibrational ground level of S_1 to S_0. The return often occurs to a vibrationally excited level of S_0 followed by a final IC process to the lowest level of S_0.[195] Due to the possibility of several IC processes, the light emitted by fluorescence is of lower energy than the absorbed light, that is, redshifted, as represented by the color scheme in Fig. 2.25. This redshift phenomenon is called *Stokes shift* and was first observed by G. Stokes in 1852.[197]

Normally, the spin of an electron in the excited state is orientated antiparallel to the remaining electron in the ground state. This is characteristic for singlet manifold electronic states and is illustrated by the yellow blocks and the small arrows in Fig. 2.25 within the S_x states. However, it is possible for the electron to undergo a spin-flip and end up in the first triplet state T_1, which is called intersystem crossing (ISC). Further transition to S_0 is only possible byz another rare spin-flip, which results in relatively long time scales for triplet emissions. This is the cause of the higher lifetime of phosphorescence.

3 Materials and Methods

This chapter contains an overview of the relevant preparation procedures and experimental setups that were used. All used chemical components, laboratory consumables as well as samples are listed in tables. Introductions of the Langmuir-Blodgett technique and various setups for membrane support are given.

3.1 Chemicals and Materials

Lipids ($>99\,\%$)	Distributor
Cholesterol ((3β)-cholest-5-en-3-ol)	Sigma-Aldrich
DiynePC (1,2-bis(10,12-tricosadiynoyl)-sn-glycero-3-phosphocholine)	Avanti Polar Lipids, USA
DPhPC (1,2-diphytanoyl-sn-glycero-3-phosphocholine)	Avanti Polar Lipids, USA
DPPC (1,2-dipalmitoyl-sn-glycero-3-phosphocholine)	Avanti Polar Lipids, USA
Rhod-DOPE (1,2-dioleoyl-sn-glycero-3-phospho-ethanolamine-N-(lissamine rhodamine B sulfonyl))	Avanti Polar Lipids, USA
Stearic acid ($CH_3(CH_2)_{16}COOH$)	Fluka
Oleic acid ($CH_3(CH_2)_7(CH)_2(CH_2)_7COOH$)	Fluka
PTPE (1-palmitoyl-2-(10,12-tricosadiynoyl)-sn-glycero-3-phosphoethanolamine)	Avanti Polar Lipids, USA

DNA / Microbeads	Distributor
Amicon® Ultracel Filter, Ultra-0.5 $50\,kDa$	Merck, USA
DNA oligomers (5'-AGGTCGCCGCCC-3'), $432\,ng\,\mu l^{-1}$	Metabion
Polysterine microbeads ($3.05\,\mu m$), streptavidine coated	Kisker Biotech

Chemical substance (p. a.)	Distributor
1,1',4',1"-terphenyl-4-thiol (TPT)	Sigma-Aldrich
Acetone $((CH_3)_2CO)$	Fischer Chemical
Argon (Ar), 4.6	Linde
Chloroform $(CHCl_3)$	VWR
Decane $(CH_3(CH_2)_8CH_3)$	Merck
Deionized water (Milli-Q), $18.2\,M\Omega\,cm$	Millipore, USA
Dimethylformamid $((CH_3)_2NCHO$	VWR
Ethanol (CH_3CH_2OH)	VWR
Gramicidine (from *Bacillus aneurinolyticus*)	Sigma
Hexanol $(CH_3(CH_2)_5OH)$	Alfa Aesar
Hydrochloric acid $(HCl(aq))$, $37\,\%$	Fischer
Hydrogen peroxide (H_2O_2), $30\,\%$	VWR
Isopropyl alcohol $((CH_3)_2CHOH)$	VWR
Nitrogen (N_2), 4.6	Linde
Oxygen (O_2), 4.6	Linde
Polydimethylsiloxane sylgard 184 (PDMS)	Dow Corning, USA
Potassium chloride (KCl)	VWR
RBS®35	Carl Roth
Sodium chloride (NaCl)	Alfa Aesar
Sulfuric acid (H_2SO_4), $96\,\%$	VWR
Zinc chloride $(ZnCl_2)$	Alfa Aesar
α-Hemolysin (from *Staphylococcus aureus*)	Sigma-Aldrich

Samples	Distributor
HOPG (Highly oriented pyrolytic graphite) ZYB spread $0.8\,\% \pm 0.2\,\%$	µmash, USA
Mica	Plano
Quantifoil® Multi A, copper and gold	Quantifoil® Micro Tools
Silicon nitride membrane chips (various dimensions)	Silson, Eng

Laboratory Equipment	Distributor
Axopatch 200B	Axon instruments
Balance CP224S	Sartorius
Centrifuge 5417 C	Eppendorf
Cold light source KL 200 LED	Schott
Desiccator	DURAN
Hamilton Syringe (250 µl)	Hamilton Bonaduz, CH
Helium Ion Microscope (HIM)	Carl Zeiss
Intensometer fieldmaster GS	Coherent, USA
Ionovation ExplorerSlides	Ionovation
Ionovation Explorer	Ionovation
Isolation table MOD-1XL	Herzan
K20 Thermo electron Typ 002-4276	Thermo Haake
Langmuir-Blodgett trough ($1200 \, cm^2$)	Riegler und Kirstein
Laboratory glass (beaker etc.)	Schott Duran
Light microscope Axiovert 200	Carl Zeiss
Light microscope BX51	Olympus
LCR Meter HM8018	Hameg
Magnetic Stirring Hotplate	Heidolph
Microscope slides ($75 \times 26 \, mm^2$)	Menzel-Gläser
NeMESYS syringe pump	Cetoni
Needles (ø0.5 mm x 40 mm)	B. Braun
Pipette, adjustable (1 µl, 10 µl, 250 µl, 1000 µl)	Brand
Pipette tips (1 µl, 10 µl, 250 µl, 1000 µl)	Brand
Plasma cleaner (O_2/Ar)	Self-constructed
Pneumatic Vibration Isolator, S-2000A	Newport, USA
Reference 600 Potentiostat/Galvanostat	Gamry Instruments, Inc.

Laboratory Equipment	Distributor
Rotary evaporator RV 05	Janke und Kunkel
Silicone tube (OD: 20 mm, ID: 10 mm)	Bola
Syringes, plastic (1 ml, 10 ml)	B. Braun
Syringes, glass (10 ml)	ILS
Thermocycler	VWR
DC10 pump 003-2859 Thermo electronics	Thermo Haake
Tissue wipers, cellulose/polyester	ITW Texwipe, USA
Ultrasonic bath digital s	Elma
UVS-14 EL, 4 W 254 nm	UVP, USA
Vortex-2 Genie	Scientific Industries, USA
Water jet pump	Brandt
Zeiss stemi 2000-C	Carl Zeiss

3.2 Langmuir-Blodgett Trough

The Langmuir-Blodgett (LB) technique is an elegant method for preparation of well ordered, layered structures with control of molecular precision.[198] Due to the broad variety of materials that can be transferred to virtually any surface, this technology is widely used in modern science.[199] This chapter is intended to clarify the preparation details with the LB trough.

The main component of a LB trough (Fig. 3.1) is the subphase reservoir, which is commonly made of polytetrafluoroethylene (PTFE). Its chemically inertness and hydrophobic character makes PTFE a highly suitable material for LB troughs. Movable barriers slide parallel to the walls of the trough and are in contact with the top of the fluid. They are also typically made from PTFE. In a modern rectangular LB trough setup, two barriers are guided along the surface in a simultaneous manner. That way, the area of a monolayer film at the air-water interface of the enclosed area can be varied. Structural as well as conformation parameters of the molecular film can be modified by reducing the area per molecule.

An important parameter in that context is the *compression factor*, which is the ratio

between the initial and the final area, enclosed by the barriers of a LB trough. More precisely, the area of a molecule at the air-water interface is compressed by that factor during the compression routine. Though there is theoretically no limit to this factor, because the final area can be taken as small as necessary, factors of 10 to 20 are common. Limitations result from a final minimal distance between the barriers to hold the Wilhelmy plate. For the purpose of a high compression factor, only the dimension of the trough perpendicular to the barriers is of interest. Therefore, LB troughs of high compression factors are long, but narrow. Most molecules, arranged as a two dimensional film at an air-water interface, exhibit all of their characteristic rearrangement and thermodynamic behavior within a window of a compression ratio of 10, starting in the gaseous phase. The trough width is only essential for a larger storage of film material to transfer to a sample.
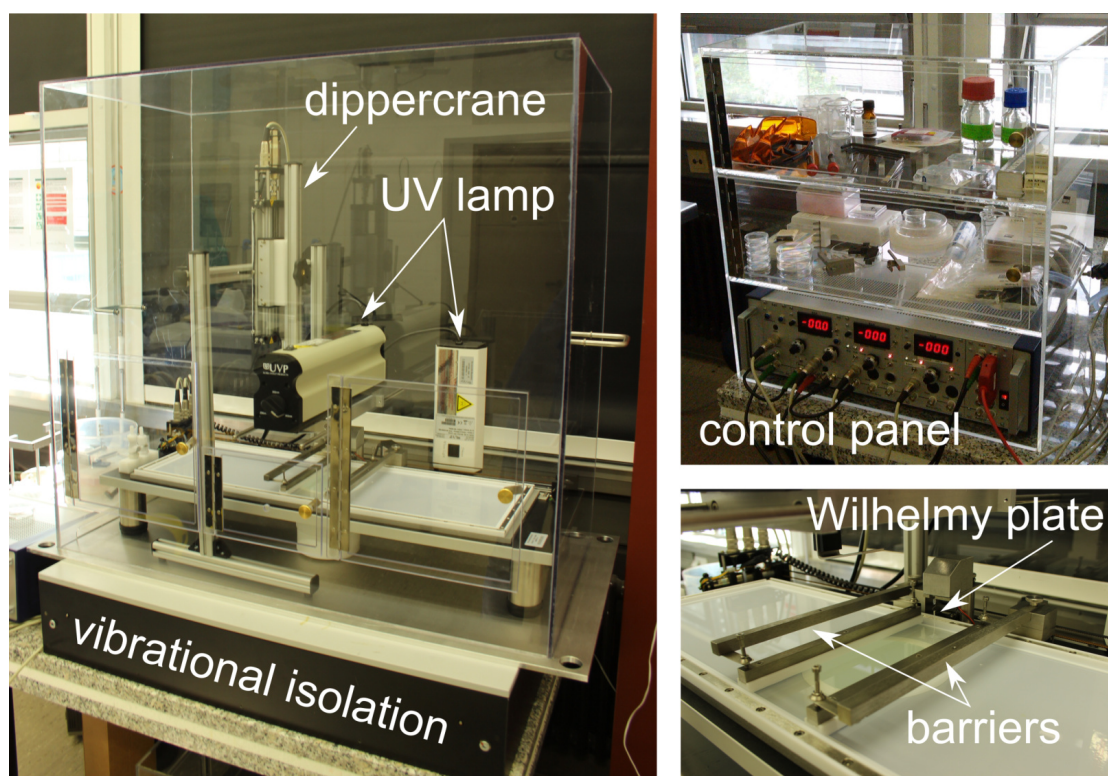

Figure 3.1: The Langmuir-Blodgett trough with a control panel and a table for vibrational isolation. Left: The LB trough is covered by an acryl glass box. The UV lamp is placed above the trough, a second one is stored in the background. Upper right: A storage box for equipment and the control panel. Lower right: A detailed view of the barriers, the enclosed area where the monolayer is located, and the housing of the Wilhelmy sensor.

After an optimal cleaning of all the PTFE components (see chpt. 3.2.1) of the LB trough, the reservoir is filled with the preferred subphase, usually water. The movable barriers should be arranged in a fully open position. Due to the hydrophobic PTFE, a meniscus appears at the trough bordering or at the barriers. The fluid level should be chosen with care. If the level is too low, film material at the surface may emerge under the barriers, and if the level is too high the film material might spill over. After filling the reservoir, the surface pressure balance should be adjusted to zero. To test the cleanliness of the water surface, the surface pressure should not change as the barriers move to their closed position. A large change indicates surfactants are present and further cleaning is necessary.

It is generally recommended to cover the whole experimental setup of the LB trough. An acryl glass cage can be used to prevent dust and other environmental contamination from the water surface. For sensitive experiments at the LB trough, vibration isolation is recommended. With active isolation platforms, mechanical vibration or acoustical noise can be eliminated to the highest requirements. For exact control of the subphase temperature, a water loop is mounted below the trough. Reaching the target temperature can be time consuming for greater amounts of subphase. Vibrations of the pump may affect the Wilhelmy plate.

Application of amphiphiles to the air-water interface is generally performed with low concentrated solutions (up to $5\,\mathrm{mg\,ml^{-1}}$) of unpolar solvents like chloroform. To avoid any reactions of the solvent with any application device, only inert materials should be used. Hamilton syringes are made of glass and stainless steel and are highly suitable. Droplets of solution should be deposited at the air-water interface very carefully (Fig. 3.2). The spreading efficiency is reduced, if high amounts of solution are applied to the interface in a short among of time. Amphiphiles are then simply pushed into the subphase.
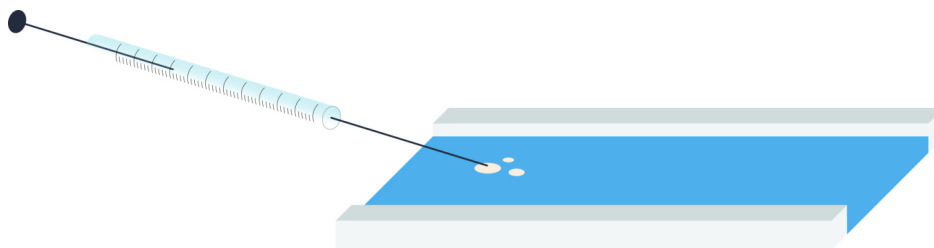

Figure 3.2: Application of the lipid solution with a glass syringe.

After preparing the film at the air-water interface, evaporation of the solvent must be awaited. Immiscible solvents like Chloroform take only $5\,\mathrm{min}$ to evaporate. If water

soluble solvents like methanol are used, complete negation of the influence on the surface tension take up to 30 min. The temperature of the subphase also affects this time, evaporation time is shortened with high subphase temperatures.

Transfer of the Langmuir film to a substrate is performed by a sequence of dipping and withdrawing of the sample through the air-water interface. The sample is attached to an electronically controlled lifter to ensure constant transfer parameters. In order to minimize vibrational interactions between the lifter and the trough, the lifter is mechanically disconnected from the trough. Individual mountings are necessary to fulfill individual sample requirements (Fig. 3.3).
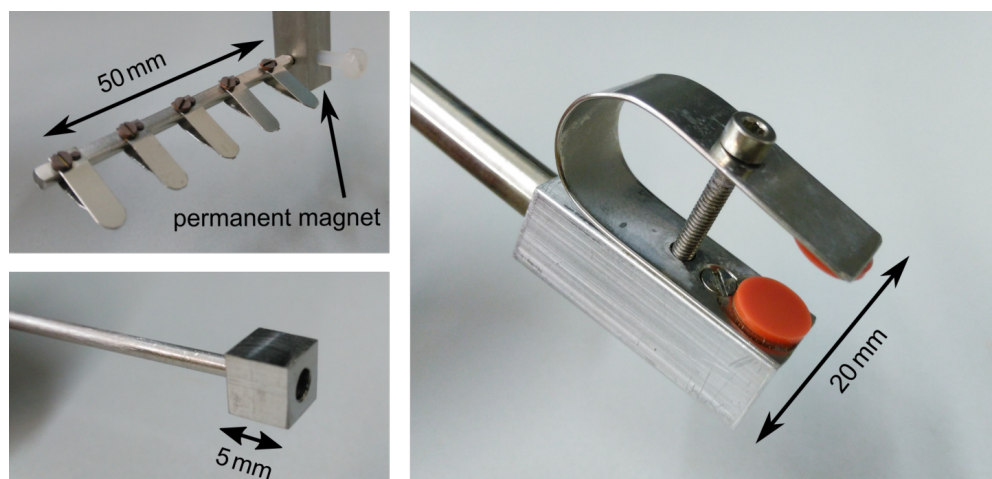
Figure 3.3: Various sample holders for the LB and LS transfer. Upper left: up to five samples can be clipped. The angle is adjustable. A steel disk with a sample can be attached to a magnet in a 5° angle. Lower left: samples can simply be hold by a aluminum block. Suitable for the *horizontal drawing up* technique only. Right: PTFE coated rubber is attached to the clips. Used for germanium preparation with LS transfer only.

Beside the conventional Langmuir-Blodgett technique (see chpt. 2.4.5), the Langmuir-Schaefer (LS) technique is commonly used. There, a sample is pushed horizontally orientated onto the water surface. It is then withdrawn carefully to transfer film material. The contact angle of the sample should be around 5°, to drain off the water. With an entirely horizontal arranged sample, the *snap off* of the water is unpredictable and may damage the already transferred film.

Due to the amphiphile orientation at the air-water interface, the hydrophobic part of the film material is pointing to the sample surface. Therefore, the LS technique is highly suitable for hydrophobic samples like graphene, but only single layer transfer protocols are feasible.

A similar technique is called *horizontal drawing up*.[199] There, the sample is stored in the subphase, when the amphiphiles are spread at the surface. The transfer is then performed in a single upstroke trough the surface. Due to the orientation of the molecules at the water surface, the transferred film will be of opposite direction as with the LS technique. Therefore, a hydrophilic sample is required. An angle of 5° must also be maintained with this technique. A second layer of molecules can be attached to the first by a subsequent LS transfer.

3.2.1 Cleaning Procedure

Frequent cleaning of the trough and all of its PTFE components is necessary to remove residues from former experiments. Simple cleaning of the empty trough is done with wipers soaked with acetone and isopropanol. Rubber gloves should be used at any time to minimize oils from the skin contaminating the apparatus. Cleanliness is very important with all the preparation and can not be overstated.

An intensive cleaning is achieved by using an alkaline addition to the subphase, for instance RBS®35 (Carl Roth), which is intended for cleaning glassware. Additional heating up to 65 °C of the alkaline subphase for 60 min is beneficial. The cleaning protocol is completed by two subsequent cycles of subphase exchanges with Milli-Q water, to avoid any residues of alkaline agent. It should be taken into account that humidity of the air around the LB trough will increase, if a dust protection is used to cover the trough during the cleaning by heat. Electric components may get damaged by the high humidity.

Removal of a remaining Langmuir film is done by vacuum. Thereto, a thin nozzle (PTPE/glass) mounted to a tube and a water pump jet is guided along the surface to take away a tiny amount of water and every kind of contamination. This procedure is appropriate to remove contamination of any kind and should be performed in advance to all experiments.

3.2.2 Sample Preparation

Appropriate pretreatment of samples that are going to be coated with the LB technique is paramount. Successful transfer of molecules from the air-water interface requires a proper chemical character of the sample surface to allow the molecules to prefer the sample to the water.

Highly oriented pyrolytic graphite (HOPG) as well as Mica (a silicate mineral) are

sheet materials containing nearly perfect basal cleavage. Freshly cleaved surfaces have been used as clean imaging substrates in AFM for a long time, exhibiting an ultra flat surface. By mechanical exfoliation (adhesive tape), sample preparation is very easy and can be realized shortly before the transfer process to get a clean sample.

Glass slides for preparation with the LB technique can be cleaned very effectively with several corrosive chemicals. A mixture of one part hydrogen peroxide (H_2O_2, 30 %) and two parts sulfuric acid (H_2SO_4) is called *Caro's acid* and forms peroxymonosulfuric acid, which is a highly oxidizing agent with the ability to peroxidize organic components.

$$H_2O_2 + H_2SO_4 \rightleftharpoons H_2SO_5 + H_2O \tag{3.1}$$
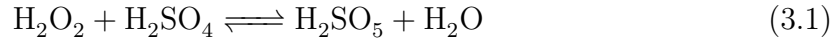
Heating up to $100\,°C$ for $30\,min$ increases the cleaning effect. Because of its fast decomposition, only fresh H_2O_2 should be used for cleaning purposes, and bubbles of oxygen should arise in the process of mixture. Samples of Si_3N_4 can also be treated with Caro's acid, though caution is advised. Arising bubbles can destroy the fragile membrane of the Si_3N_4 sample in the cleaning process.

Sample holders for transmission electron microscopy (TEM) were used to investigate substrate supported free-standing lipid membranes. The so-called *TEM grids* are available in various materials and mesh sizes up to 2000 meshes per inch, which is about $12.7\,µm$ per mesh. For even smaller apertures, TEM grids are coated with a perforated support foil (Quantifoil®) with pre-defined hole sizes ($1\,µm$ to $2 \times 8\,µm^2$ in diameter). The support foil is about 10–$12\,nm$ thick, but due to residuals from the production process the overall thickness of the support foil is about $20\,nm$.[200] No further treatments were performed before LB transfer, and all TEM grids were single used.
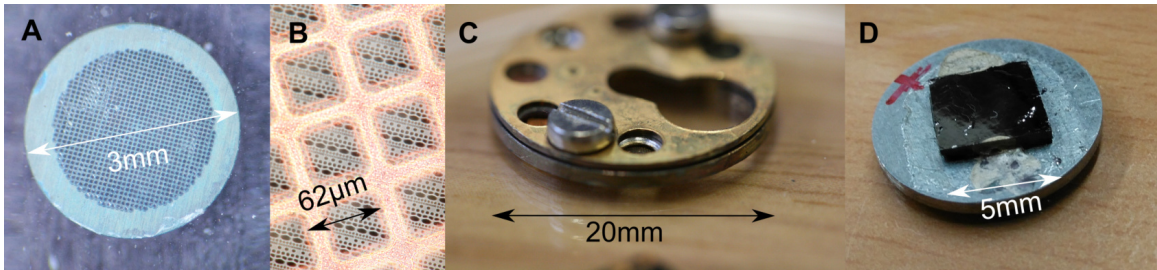

Figure 3.4: A Quantifoil TEM grid (A) with $400\,mesh$ per inch. A detailed image of the *Multi A* reveals the polymeric support foil (B), placed over a copper mesh. A two-part sample holder (C) was used to investigate the TEM grids with the HIM. For AFM studies, HOPG substrates were attached to a steel disc (D) before LB transfer. Figure C provided by D. Emmrich, Bielefeld University, Germany.

With the exception of the germanium crystal, all samples that were investigated with AFM had to be attached to a steel disc of 10 mm in diameter (Fig. 3.4D). The steel disc was then magnetically mounted to the AFM itself to prevent movement and vibration during the measurement. This is a critical step, because the firmness and solidity in the positioning of the sample is one of the limiting factors to obtain an AFM image with good resolution. The TEM grids were fixed to the disc with small amounts of glue at two spots at opposite sides so that no point of interest is damaged. HOPG samples were simply attached to the disk by their backside. An AFM with an integrated scanner to the cantilever holder was used to investigate the germanium crystals. This setup allows scanning of larger samples.

Similar preparations were made for investigations with the HIM. The TEM grids were placed into a depression of a sample holder and then secured by a metal ring of the same size in top of it (Fig. 3.4C). The ring in turn is then secured by a bolted top cover with a cutout for the TEM grid. The grid is fixed in position, largely free-standing, and easy to handle.

3.2.3 Isotherm Measurement and Monolayer Transfer

The original objective of a LB trough is to study the properties of monolayers of amphiphilic molecules. The area per molecule can be varied by moving barriers and a balance monitors the surface pressure that is effected by the molecular monolayer. Two dimensional compression of the Langmuir film can be compared to processes in thermodynamics (see chpt. 2.4.4).

After applying amphiphiles to the water surface between the barriers of a LB trough and 5 min has passed to evaporate the solvent, the barriers begin to compress the enclosed area. Preliminary calculations should be made to ensure that the monolayer is in its gaseous phase at this time. If the properties of the monolayer are unknown, it is recommended to carefully add monolayer material until the surface pressure begins to rise. That way, all parts of the isotherm are covered (Fig. 3.5).

When setting the speed of the barriers, two considerations have to be taken into account. When the speed is too high, rearrangement of the molecules is inhibited, that is, lower speeds allow better molecular packing.[201] With a more complex monolayer material, this effect becomes more critical. For a too low barrier speed, dissolution of film material into the subphase or leakage of the film material through corners of barriers take great effect. Even for very small amounts, the calculated area per molecule is then faulty.[115]

A barrier speed of $100\,\mu m\,s^{-1}$ per barrier was used for all experiments, if not stated otherwise. It follows that the area is decreased by $200\,\mu m\,s^{-1}$ (two barriers) or $12\,mm\,min^{-1}$. However, the compression rate per molecule of monolayer material is the most informative parameter and has to be calculated according to the individual material character.[202]
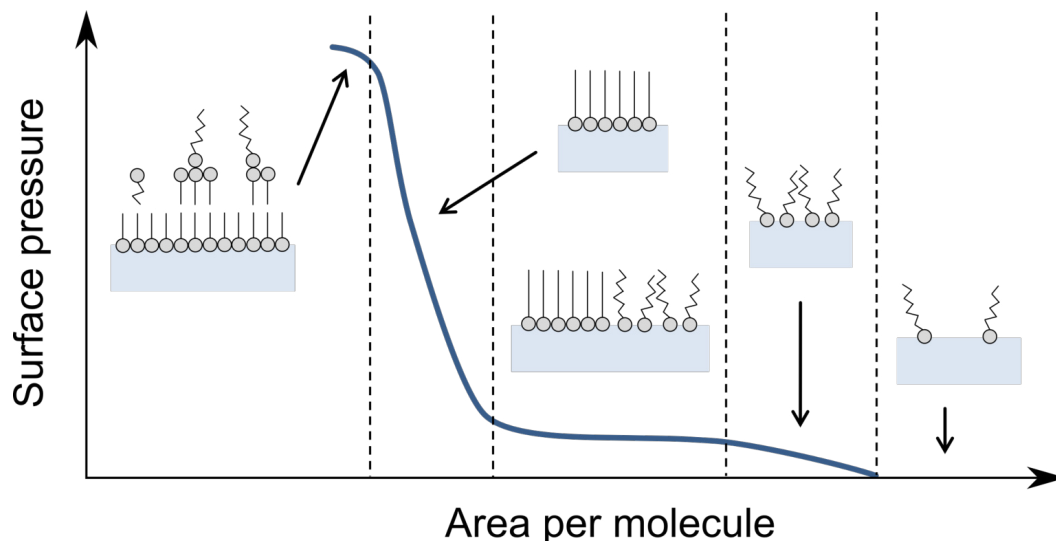

Figure 3.5: A symbolic isotherm with a typical shape, which is often recorded by compression experiments with the LB trough.

In order to take a normal isotherm measurement with the LB trough, the area is simply being compressed until the collapse point of the monolayer is reached. Further compressing at that point is contaminating the trough excessively and should be avoided. Compression has to be stopped at the desired parameters, if the monolayer is used to be transferred to a sample, usually within its solid state phase. Modern LB troughs come with a feedback control to adjust the barrier speed, shortly before the compression parameters are reached. That way, an overshot is prevented. This feedback control is also used to keep the surface pressure constant during any transfer process and to replenish monolayer material.

As described in chpt. 2.4.5, the first layer of molecules transferred to the sample is of significant character. It is the initial contact between the monolayer material and the deviant chemical composition of the sample. For a quick check on the quantity and the quality of the deposited monolayer on a solid support, the transfer ratio can be determined.[203] It is defined as the ratio between the decrease of Langmuir film area during a deposition stroke, and the area of the withdrawn substrate, if the surface pressure is kept constant during the transfer. An ideal transfer process exhibits a

transfer ratio that is equal to 1. This means that the area of the Langmuir film is decreased by the same amount of film material that is transferred to the sample surface. With some transfer techniques (mostly the horizontal drawing up), the surface of a lifter mechanism has to be taken into account.

3.2.4 Lipid Preparation

For preparation of LB films at the air-water interface and bilayer membrane experiments, the amphiphiles were dissolved in chloroform. Concentrations of 0.5–$5\,\mathrm{mg\,ml^{-1}}$ were used, depending on the substance and the purpose. High concentrated solutions are unwieldy, because of the small amount of solution that has to be applied to the trough. With low concentrated solutions, the amount of solvent, that has to evaporate at the air-water interface is too high.
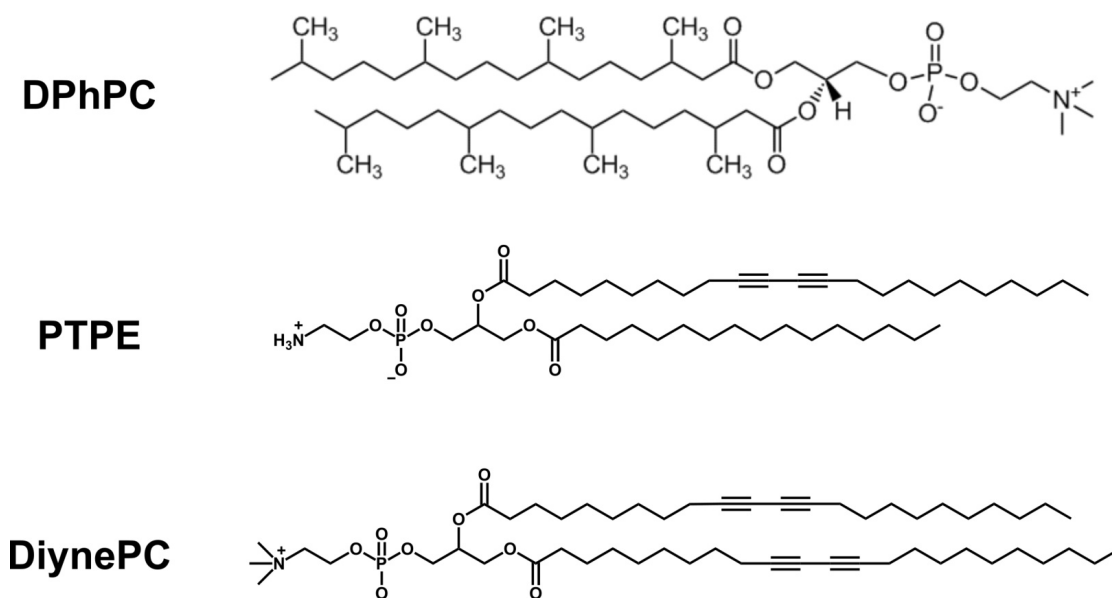
Figure 3.6: From top to down: DPhPC (1,2-diphytanoyl-sn-glycero-3-phosphocholine), PTPE (1-palmitoyl-2-(10,12-tricosadiynoyl)-*sn*-glycero-3-phosphoethanolamine), and DiynePC (1,2-bis(10,12-tricosadiynoyl)-*sn*-glycero-3-phosphocholine) were utilized in this thesis.

Solutions of lipids (Fig. 3.6) are commercially available in form of glass ampoules with inert gas above the liquid. As with all solutions, the problem is the change of concentration with time, especially with highly volatile solvents like chloroform. Calculation of the correct area per molecule from LB experiments highly depends on

the knowledge of the exact concentration. Therefore, most amphiphiles were stored as powder and solutions were prepared at short term and only small amounts (2 ml). Moreover, powder is chemically more stable in general.

Due to purity requirements, preparation of lipid solutions should only be performed with single-use flask, or at least high-grade cleaned glass ware. All flask must be of brown color to reduce the damage taken by light. All caps should be made from glass, ground glass joints are to be preferred. Final cleaning of glass ware should be performed with the same kind of solvent that is used in the preparation. This procedure dissolves all remaining residues that would otherwise be dissolved in the preparation. Laboratory gloves are essential in all steps of handling.

After the preparation, inert gas (argon) is used to fill the air above any solution. Flasks containing powder must be evacuated in a desiccator and carefully ventilated with argon. Flask for preparation should be filled with argon in advance to the preparation. Storage of lipid solutions is recommended at $-20\,°C$ in darkness. Purity, correct concentration and chemically integrity is of extreme importance and can be the difference between success and failure. Lipids must not be used after the expiration date.

3.2.5 UV Polymerizable Phospholipids

Free-standing and substrate-supported monolayers of 1-palmitoyl-2-(10,12-tricosadiy-noyl)-*sn*-glycero-3-phosphoethanolamine (PTPE) and 1,2-bis(10,12-tricosadiynoyl)-*sn*-glycero-3-phosphocholine (DiynePC) were prepared and investigated in this thesis. Phospholipids containing one or more diacetylene groups in their hydrocarbon chains can be polymerized to 2D-structures by UV-illumination. The synthesis of polymeric diacetylene (PDA) was first reported from the laboratory of G. Wegner.[204] Polymerization by UV-irradiation establishes a conjugated system[205] with light absorbing properties.[206] PDA then had been utilized for vesicles,[207] Langmuir monolayers[208,209] and self-assembled films.[210] Membranes of UV-polymerizable lipids have an advantage over conventional lipids with respect to robustness.[211]

The preparation and polymerization of diacetylene lipid membranes in this thesis was realized by LB technique. The UV-induced polymerization of diacetylene groups in the tail of hydrocarbon chains gives a possibility to improve the stability of the Langmuir film.[199,212,213] The mechanism of polymerization (Fig. 3.7) proceeds by cross-linking due to chain radical polymerization.[211]

Raman spectroscopy[214,215] and X-ray studies[216,217] indicate the formation of alternating double and triple bonds in the polymeric backbone. The diacetylene group provides

a direct and specific marker signal for vibrational spectroscopy that has been exploited to follow the polymerization of polycrystalline material using FTIR spectroscopy[204] and FT-Raman spectroscopy.[215] Other characteristic effects to the signals of acyl chains in FTIR spectra have been revealed for lipid vesicles with diacetylene groups.[218]
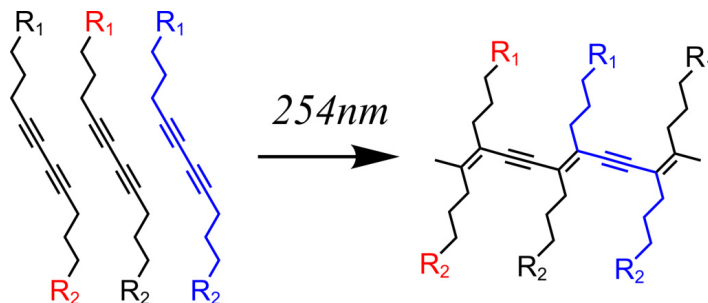

Figure 3.7: Tails of three lipid molecules are shown. They are polymerized by UV-irradiation at 254 nm. The marked red substituents result from different molecules and are linked through polymerization, the blue substituents show the origin of the new triple bond. Thinning of the layer is to scale and accompanied by a lateral expansion, which is detectable at the LB trough due to an increase of surface pressure. Polymerization of diacetylene has been explained by topochemical 1,4-polymerization.[204]

3.3 Black Lipid Membranes

The successful formation of free-standing lipid bilayer membranes supported by a horizontal PTFE septum in a microfluidic chamber can be monitored by fluorescence microscopy. In a reflected light setup, a small concentration of Rhodamine B labeled lipids is used to grant insight in the processes of membrane formation. By decreasing fluorescence intensity, the transformation of a lipid bulk to a bilayer by a process of thinning is observable. Due to the lack of fluorescence light emitted by the thin membrane, it appears black, which also fits the name *black lipid membrane* (BLM). The term is originally based on the fact that the membrane is dark in reflected light because it is only a few nanometers thick. Therefore, the light reflected from the back disturbs the light reflected from the front destructively.[219]

The centerpiece of the fluorescence microscope setup is an inverted microscope, which grants superior access to the top side of the sample (Fig. 3.8). A mercury lamp (100 W) is used as excitation light for fluorescence. By a set of filters (FS 20, Zeiss), the light first passes through an excitation filter (BP 546/12) to then being deflected

by a beam splitter (FT 560) to the sample. Fluorescence light of longer wavelength from the sample is then passing through the beam splitter and an emission filter (BP 575-640). The latter is important to remove any excitation light. This set of filters is appropriate for Rhodamin B (excitation 543 nm, emission 565 nm).

An additional halogen lamp is mounted to the top of the sample, to visualize non-fluorescent objects of the sample. A 40x objective (LD Achroplan, Zeiss) is used and an automatically movable stage (99S008, Ludl Electronics), which can be controlled either by software or manually by a joystick. A CCD camera (Imager 3LS, LaVision) is installed at the camera port of the microscope. The top part of the microscope can be protected by a Faraday cage for interference-low electrochemical measurements.
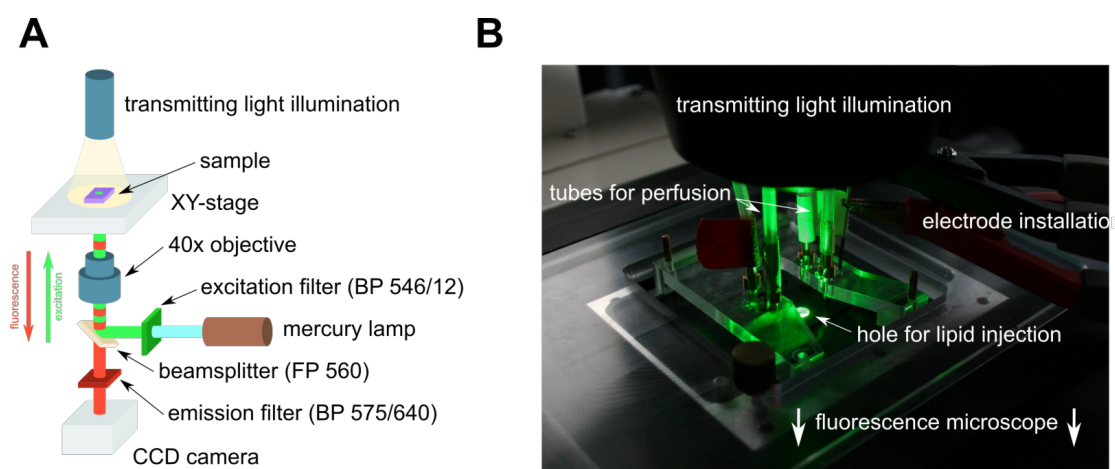
Figure 3.8: (A) Experimental setup for fluorescence. Excitation by a mercury lamp (blue line, green line after excitation filter). The beamsplitter separates excitation light and fluorescence light (red line). An emission filter prevents any remaining excitation light from reaching the CCD. (B) The green excitation light comes from below and illuminates the Ionovation chamber as well as the tubes for perfusion. The halogen lamp for transmitting light is visible in the top.

Two syringe pumps are used for perfusion of the microfluid chamber with buffer solution and lipids. They are controlled by a software and can be programmed to perform repeating processes of perfusion. Tubes are installed to connect the microfluid chamber to the syringe pumps. For interference-low electrochemical experiments, the tubes are grounded and shielded by aluminum. The injectors at the end of the tubes can be withdrawn from the microfluid chamber, to fulfill the highest requirements of electrical shielding.

3.3.1 Silver-Silver Chloride Electrodes

A proper prepared silver-silver chloride (Ag/AgCl) electrode features a constant electrode potential and should be reproducible in terms of electrochemicals properties. This has been found true within a few microvolts.[220] Renewal of the electrode may become necessary and should be done every week to meet the specifications. For that reason, the electrode should be easy to disassemble and reassemble.

First, a 0.25 mm thin silver wire is coated with a thin layer of silver chloride. Thereto, the proper cleaned wire (acetone) is made the anode in a 1 M HCl solution, platinum being the cathode. A voltage of 2.5 V is applied for 30 s. Bubbles of hydrogen should arise at the cathode. The wire is then carefully rinsed with water to dispose of any remaining HCl. The color of the freshly prepared electrode is variable, ranging from sepia to brown.
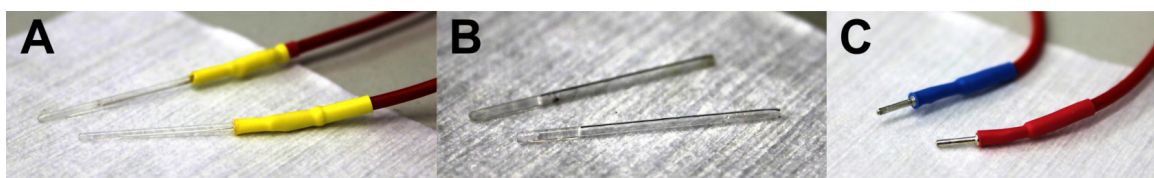

Figure 3.9: Two fully assembled (A) Ag/AgCl electrodes. Silver wire coated by $AgCl_2$ was inserted into a glass tube and secured with a shrinking tube. This connecting is reversible for future maintenance. Glass tubes (B) of 30 mm were filled before to one third with agarosegel. No air bubbles are visable. Connecters (C) are attached to the other end of the cables.

A glass tube of 30 mm with an inner diameter of 1 mm is suitable for electrode housing (Fig. 3.9). The front opening, which later will be in contact with the aqueous solution of the measurement, should be hold briefly to the flame of a Bunsen burner to slightly reduce the diameter. This will contain the agarose salt bridge.

Preparation of agarose gel is done by mixing agorose powder with buffer solution of choice. A mixture of 5 ml buffer solution and 75 mg agarose powder is heated until the agarose is completely dissolved, but it should not be overboiled, as some of the buffer will evaporate and the concentration will change. The glass tubes are then carefully submerged into the hot agarose gel. By capillary forces, the gel will instantly rise into the glass tube of about 10 mm. No air bubbles should be visible.

The gel is dried after 5 min. Gels are described in terms of percents, using a 5 % solution has proven to be a best compromise in terms of stability and conductivity. The latter also depends mostly on the concentration of the electrolyte solution. Thus,

3.5 M KCl electrolyte solution is the best choice.

However, some experiments require precise control of change in buffer concentration (all osmotic experiments). For these experiments, the salt bridge of the electrode must be prepared with the same ion concentration of the experiments to prevent any ion migration from the salt bridge to the experiment setup, or the other way around.

After waiting 5 min for the gel to be dried, 3.5 M KCl is filled into the glass tube. This can be done with a thin needle of a syringe. 18 mm of the silver chloride coated silver wire is then carefully threaded into the glass tube. A thin space between the wire and the gel should be granted. The top of the electrode should be sealed with shrinking tube to prevent buffer solution from leaking.

During handling of the electrode, exposure to direct sunlight should be avoided due to photochemical reactions of the silver chloride. A silver wire can also be prepared by electrolytic procedure. Starting from a platinum wire, the silver chloride electrode is formed by the electrodeposition of silver. Electrodes prepared in this fashion from pure solutions have a lower bias potential than does the preceding type.[92]

3.3.2 Ionovation Explorer Slide

The Explorer Slide is a commercially available microfluidic chamber (Ionovation, Germany) that is designed to generate a lipid bilayer membrane across a micro hole (50–120 μm) in a PTFE septum. The horizontal setup[221] of the Explorer Silde is highly suitable for the use in common microscopes and allows further investigations by optical tweezers or fluorescence microscopy. To form a lipid bilayer membrane, the widely established painting method[37] is used, which is related to the Montal-Mueller[38] technique. In the latter, the lipid bilayer membrane is formed in a vertical arranged manner, while in the first, it is formed in a horizontal manner.

The Explorer Slide has a multilayered design (Fig. 3.10). A PTFE septum of 25 μm thickness is the centerpiece. It contains a small aperture, which is utilized as a support for the free-standing lipid bilayer membrane. The PTFE membrane is sandwiched between a coverslide and the chamber body using a double-sided adhesive film. A channel structure is cut into the adhesive film. This creates two compartments of approximately 150 μl in size, which are representing the *trans* and *cis* sides of the membrane. These compartments are only connected by the micro hole in the PTFE septum. When a lipid solution is painted over this hole, and a bilayer forms eventually, electrodes in *cis* and *trans* allow electrophysiological recordings of the bilayer.
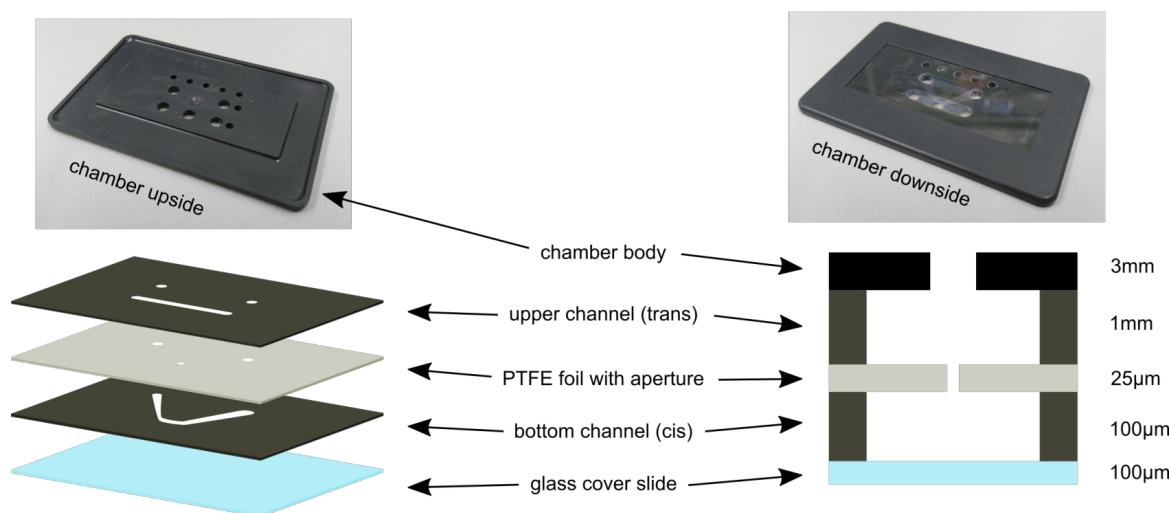
Figure 3.10: The schematic structure of the Explorer slide. A PTFE foil in the center divides the chamber into two reservoirs, connected by an aperture. The channels are formed into double-sided adhesive film. Inspired by a Figure in *Galla*.[222]

For easy access of the electrodes as well as perfusion of buffer solution, the microfluid chamber contains seven ports connected to various layers of the microfluid chamber. Two small holes are connected to the *cis* and the *trans* side of the membrane and are intended to hold the electrodes. For perfusion purposes, two additional holes are provided for each channel. The *trans* side contains an additional opening in top of the micro hole for injection of lipid solutions.

3.3.3 Experimental Setup

Except for a 14 days test period, when the commercially available setup could be used, the experiments with the Explorer Slide in this thesis were performed using a combination of home-built equipment. This includes a holder for the microfluid chamber (Explorer Slide), a mechanism to connect and disconnect the perfusion tubes, a Faraday cage, a movable stage to adjust the position of the microfluidic chamber, a syringe pumping unit and an amplifier for electric recordings. The holder for the Explorer Slide is a steel sheet containing an indentation to secure the chamber. A hole is cut out for a microscope objective to reach from the bottom for the coverslide and the micro hole in the microfluidic chamber. The holder is integrated into a movable stage to adjust the field of view into the chamber. A Faraday cage is mounted in top of the stage. The pre-amplifier for the electric recordings, which is called *headstage*, is housed in the Faraday cage to be shielded as well.
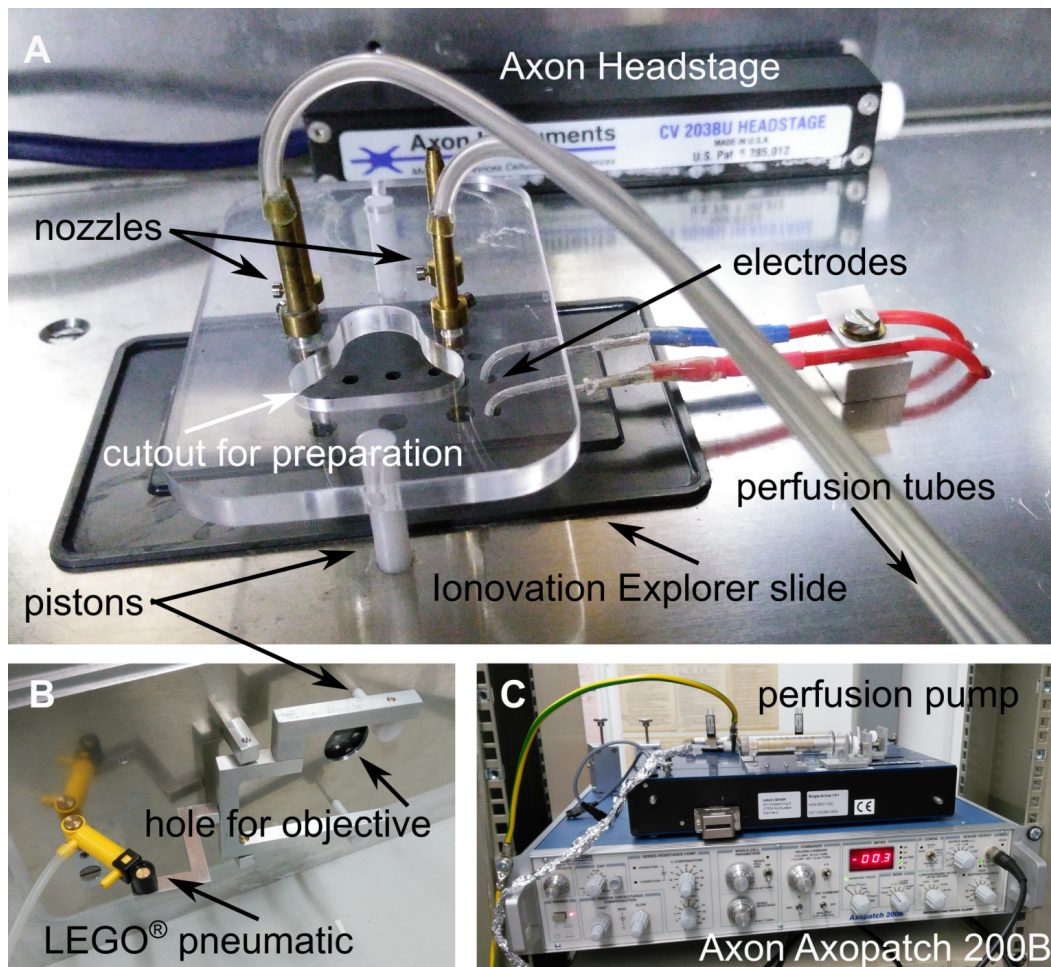
Figure 3.11: (A) Inside a Faraday cage, nozzles are mounted in a lifter above the Explorer slide. Electrodes are are guided to the slide. A cutout in the lifter allows handling wit a pipette. (B) Pistons cross the bottom to be moved by a seesaw and a LEGO® pneumatic. (C) The perfusion pump and the Axopatch are stored next to the experiment. Grounding and shielding of all involved parts is essential to reduce electromagnetic interference.

Because the metal tube nozzles that are inserted into the chamber must be withdrawn for sensitive electrophysiological recordings, an air pressure lifting device is mounted below the platform. By using air pressure through tubes, electric interference are excluded. Due to easy access, *LEGO® Technic* components were used.

Through a hole in the top of the Faraday cage, a cold light with gooseneck can be inserted to illuminate a sample, if necessary. The pumping unit for perfusion of the microfluidic chamber is stored outside the cage. Its syringe is connected by tubes, shielded by aluminum and grounded. An Axopatch 200B (Axon Instruments) was

used for electrophysiological recordings with the home-built setup, while a Heka EPC-10 (Heka Elektronik) was used for a 14 days test period.

Before an Explorer Slide can be used in an experiment, it has to be cleaned with isopropanol, to remove any residues of remaining lipids. For best results, each chamber should be used with one type of lipid only. Furthermore, isopropanol exhibits a small surface tension and flushes easily to every corner of the microchannels in the chamber. Filling with aqueous solutions is much easier after that treatment.

Buffer solution (1 M KCL, 10 mM TRIS, unless stated otherwise) is then injected into the fluid chamber using a wash bottle. High pressure is required to fill the narrow channel of the *cis* side (100 µm thick). Air bubbles must be avoided because they affect the electrical readings. The filling level should be chosen carefully. Preferably, no meniscus is visible at the openings of the fluid chamber so that the nozzles can submerge into the chamber without any spilling during the experiment. The tubes and the pumping syringe have to be filled with buffer solution, too.

Lipid solution is then added by a Hamilton pipette through the center hole of the fluid chamber. For typical concentrations of $15 \, \text{mg ml}^{-1}$, 0.1–0.2 µl are added in top of the micropore through the center hole in the microfluidic chamber. The perfusion pump is then used to wipe with the air-water interface over the micro hole. A lipid bilayer membrane is eventually formed by this *painting method* supported by the PTFE septum and can be measured electrophysiological.

Any solution of α-Hemolysin that is used for translocation experiments, must be treated with ultrasonic for a few seconds to break clusters of α-Hemolysin into individual channel proteins. Clusters are formed due to storage of solutions of α-Hemolysin after short time period and integration into lipid membranes is prohibited.

3.4 Substrate Supported Lipid Membranes

Transfer of lipids by Langmuir-Blodgett (LB) and Langmuir-Schaefer (LS) technique to substrates like HOPG, Mica, Germanium or glass was performed to study substrate supported layers of lipids in a wide variety of approaches, namely AFM, HIM, ATR, UV-VIS and light microscopy.

Polymerization of suitable lipids was performed by UV illumination with 254 nm on the Langmuir film. Dynamics, chemical as well as confirmational structure and mechanical properties were key components for the investigations.

AFM measurements were carried out at ambient conditions (20 °C) using a Nanoscope

IIIa Multimode (Digital Instruments, Santa Barbara, CA, USA) with Tap300Al-G cantilevers (BudgetSensors, Sofia, Bulgaria) in tapping mode of operation. The images were routinely treated by offset and plane correction algorithms in the software Nanoscope 5.30. Afterwards, figures were visualized by the public domain software package Gwyddion 2.44.

A scanning helium ion microscope from Zeiss (HIM, Zeiss Orion Plus) was used.

3.4.1 Fourier-Transform Infrared Spectroscopy

Attenuated total reflectance (ATR) is a powerful and commonly used sampling technique that is used in conjunction with infrared spectroscopy. The ATR setup enables samples to be examined directly in the solid or liquid state without requiring complex preparations.[223]

Fourier-transform infrared spectroscopy (FT-IR) is capable of identifying functional groups such as C=O, C−H, or N−H. Most substances can be directly recognized due to their characteristic spectrum. The sample is applied to a medium of high refractive index, like a germanium crystal. An IR beam is passing through the crystal in a way that it is reflected at least once by the internal surface in contact with the sample.

In the process of total internal reflection at the crystal, small amounts of light escape and extend a small distance of 0.5–$2\,\mu m$ beyond the surface. This short-range field is called an *evanescent wave* (Fig. 3.12). This phenomenon is leading to the term *attenuated total reflectance*, because the intensity of the reflected light is slightly reduced at this point.
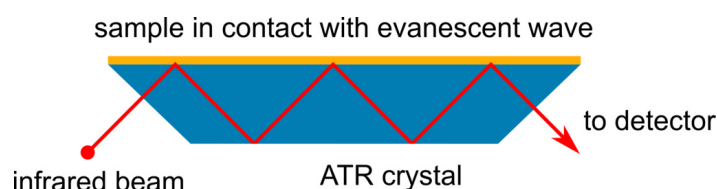

Figure 3.12: Principle of an ATR setup.

UV polymerizable lipids were investigated by FT-IR using an ATR setup to study the changes of chemical structure. Transfer of the lipid layer was carried out by Langmuir-Schaefer (LS) technique, the measurement with germanium crystals was performed by the group of Dr. T. Kottke, Department of Chemistry, University of Bielefeld.

The germanium crystal ($72 \times 10 \times 2\,\mathrm{mm^3}$) was used as internal reflection element with 17 active reflections for ATR spectroscopy in a Gateway ATR cell (Specac).

The intensity spectrum of the mounted substrate was then investigated with an IFS 66v spectrometer (Bruker Optik). This device is equipped with a mercury cadmium telluride detector exhibiting a spectral resolution of $2\,cm^{-1}$. After the intensity spectrum was captured, the germanium was removed from the spectrometer, cleaned with an argon plasma (Zepto, Diener Electronic) at $0.4\,mbar$ and $100\,W$ for $5\,min$ and then remounted to the ATR cell. With the cleaned crystal, the reference intensity for the monolayer spectrum was acquired.

For measurements with multilayered lipids, the reference intensity was measured before the coating of the IRE using the same sample. However, the best results were achieved when there was a minimum of time between intensity spectrum and reference intensity. Because preparation (including drying) of the monolayer took much more time then cleaning by plasma, the measurement of the clean sample was performed after the monolayer was measured.
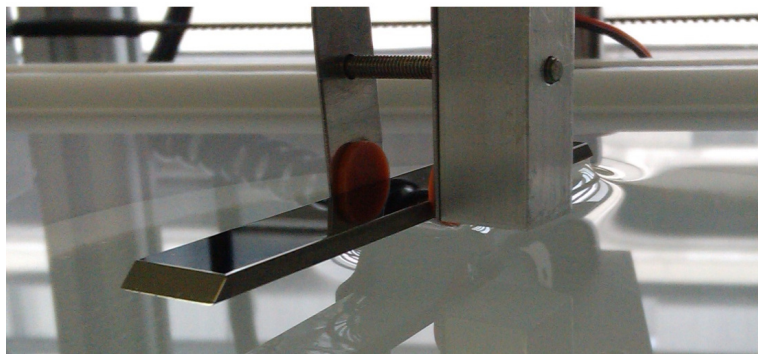

Figure 3.13: A monolayer is being transferred to a germanium substrate by LS technique. Due to to the angle of 5°, the rear part of the crystal is already in contact with the air-water interface, while the front part is not.

Monolayer preparation was performed by LS technique. Because of the high sensitivity of the ATR spectroscopy, the germanium crystal was handled with extreme care. Even contact with fresh laboratory gloves compromised the results of the sensitive apparatus. PTFE was used for any handing of the freshly cleaned germanium crystal. Two PTFE coated rubber disks are attached to the clamp to hold the crystal during the LS transfer. The crystal was placed at an angle to the water surface (5°) to drain of the water during the withdrawing (Fig. 3.13). A dipping speed of $50\,\mu m\,s^{-1}$ was used.

After the crystal was dried for $30\,min$ in the clamp, it was dried for additional $180\,min$ by a stream of dried air from a purge gas generator (Parker Hannifin 75-62) in darkness to avoid any or additional polymerization. A thermostated holder and a circulating wa-

ter bath were used to keep the temperature (20 °C) constant during the measurements of polymerization kinetics of monolayers of PTPE and DiynePC.

At this temperature, the lipids were in the gel phase.[36,224] UV induced polymerization of the lipids was done by a mercury lamp at 254 nm (4W, UVS-14 EL, Upland UVP). An UV intensity of 200 W cm^{-2} was reached at a distance of 7 cm above the germanium substrate. The intensity spectrum of the lipid layer was then recorded over a period of 120 min before and during illumination. The ATR cell was either purged constantly with dried air or argon to eliminate any effect of present oxygen. The installation of a germanium filter (Edmund Optics) limited the spectral range to below 6000 cm^{-1}, which protected the detector from scattered UV light.

Any difference spectrum was calculated from the difference between the intensity during illumination and the intensity before irradiation. The baseline correction was done using OPUS 5.5 (Bruker Optik).

3.5 Substrate Supported Free-Standing Carbon Nanomembranes

Carbon nanomembranes (CNM) made of 1,1',4',1''-terphenyl-4-thiol (TPT) were fabricated by Y. Yang, a member of the group of Prof. A. Gölzhäuser, Physics of Supramolecular Systems and Surfaces, Faculty of Physics, Bielefeld University.

The preparation is explained in detail in their publications.[33,39] Briefly, a self assembling monolayer (SAM) of TPT is formed on a gold substrate and is then crosslinked by electron radiation. The polymeric membrane is then transferred to a supporting substrate (Si_3N_4 chip), which contains a micro hole (4–12 µm) in a thin membrane. The chip is also described in chpt. 2.2.3. In this way, a supported free-standing membrane of CNM is created, which is easy to handle (Fig. 3.14).
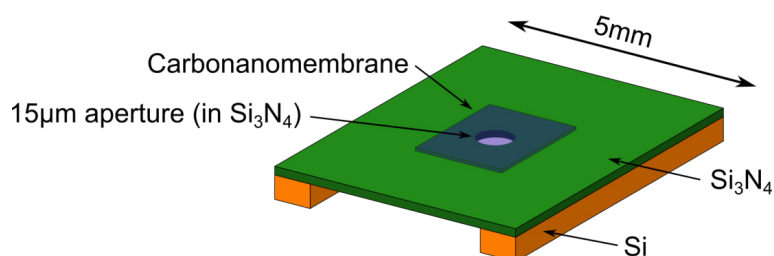

Figure 3.14: Supported by a Si_3N_4 chip, a free-standing CNM is realized, which can be used for electrophysiological recordings due to its easy handling.

The Si_3N_4 chips contain a free-standing CNM membrane and were mounted to a sample chamber for electrophysiological recordings. A simple sandwich setup of acryl glass and Polydimethylsiloxane (PDMS) as a sealant was used (Fig. 3.15).
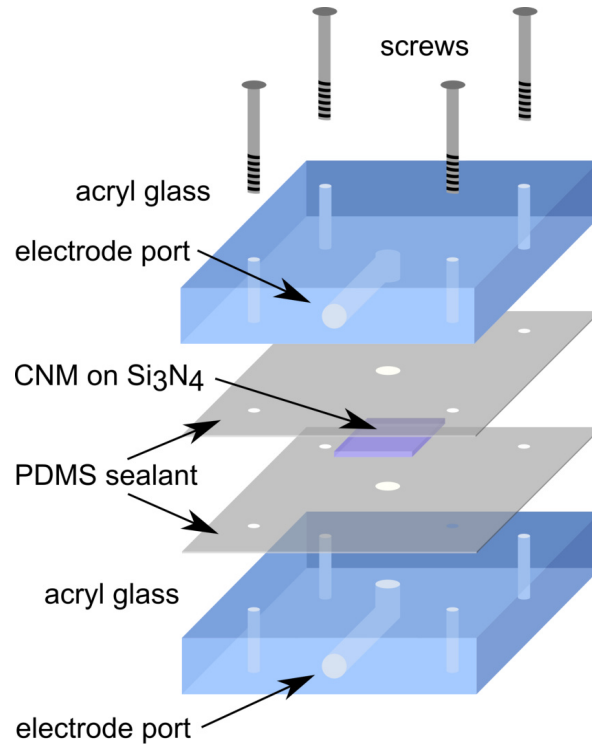

Figure 3.15: The Si_3N_4 chip (including a CNM) is embedded (purple) in an acrylic chamber. Two sheets of PDMS provide electrical sealing. A port for electrodes is available to each reservoir.

Since the absence of air bubbles is crucial, the assembly was carried out submerged in buffer solution. In this way, all liquids involved correspond concurrently to the desired buffer solution. The first step for assembling the cell is to put the bottom part of the measuring cell to the bottom of the bowl, which is filled with the buffer solution. This bottom part of the cell contains the screw thread for mounting in the final step. A pipette can be used to eliminate remaining air bubbles that are often strongly attached to the acryl glass or the PDMS. On top of this acrylic block, a PDMS sealant (1 mm thick) of the same size was put. It contains a hole for each screw thread and a center hole to connect the CNM membrane to the reservoir.

Adhesive force between PDMS and acryl glass can be raised by a treatment of oxygen plasma to the PDMS. Attaching the PDMS sealant directly to the acryl glass by adhesive tape was tested successfully.

Then, the Si_3N_4 chip was put in top of the PDMS sealant, covering the center hole completely. The chip has to be placed in the orientation that the CNM membrane is now facing upwards. If air bubbles are present, the Si_3N_4 chip can be submerged carefully in isopropanol before finally submerging into the buffer solution and put onto the PDMS sealant. Due to its smaller surface tension, isopropanol tends to avoid air bubbles and penetrates into smaller cavities like the funnel structure of the Si_3N_4 chip. Handling of the Si_3N_4 chip should be carried out with great precaution at any moment, when submerged in any fluid due to the fragile CNM membrane. After the Si_3N_4 chip had been placed thoughtfully, a second identically PDMS sealant was placed on top of the first one, enclosing the chip completely. In the final step, an acryl glass counterpart was placed on top. Through clearance holes in the latter, four screws were tightened into the bottom part of the chip. A transparent material was chosen to monitor the sample during all steps of assembly.

Electrophysiological recordings of CNM were performed using a patchclamp amplifier (Axopatch 200B, Axon instruments) and self-built silver-silver chloride electrodes.

4 Results and Discussion

The scope of this work is to establish and characterize free-standing membranes of the thickness of only a few molecules, which are then called a *2D-nanomembrane*. The meaning of the term *free-standing* is commonly understood as a structure that is not attached to or supported by another structure, in contrast to *substrate supported*, which is defined as the latter.

In this work, however, the term free-standing is used for membranes that are supported by a solid structure, but exhibit large unsupported areas.

The fabrication of 2D-nanomembranes was achieved by the Langmuir-Blodgett (LB) technique (chpt. 4.1), by a horizontal Montal-Mueller method, which is also referred to as the *painting technique* (chpt. 4.2), and from substrate supported, selfassembled layers (chpt. 4.3).

The chapter about the LB technique starts with isotherms of the substances that were utilized in this work. The quality of transferred adlayers on solid substrates was then investigated by AFM. Selfassembling properties of lipids on HOPG were studied with respect to the polymerization status by UV light. Additionally, the polymerization process was analyzed by infrared spectroscopy in an attenuated total reflection (ATR) setup. This was achieved in a cooperation with the group of Dr. T. Kottke, Department of Chemistry, University of Bielefeld. Finally, investigation of free-standing membranes from LB transfer was performed by AFM and HIM.

In chpt. 4.2, a free-standing lipid bilayer membrane was fabricated in an aqueous environment by the painting method. In a fluid chamber, a tiny amount of lipid solution is moved over an aperture by an air-water interface, which is why this technique is called painting method. Electrophysiological recordings of lipid bilayer membranes were performed with the final measurement of successful translocation of short DNA fragments through embedded α-Hemolysin.

Free-standing membranes from polymerized self-assembled monolayers are discussed in chpt. 4.3. The fabrication was done by Y. Yang from the group of Prof. A. Gölzhäuser, Physics of Supramolecular Systems and Surfaces, Faculty of Physics, Bielefeld Univer-

sity. By electrophysiological recordings, ion permeation through 1,1',4',1"-terphenyl-4-thiol (TPT) carbon nanomembranes (CNM) of various ion species was investigated with respect to their potential application for osmosis purposes.

4.1 Langmuir-Blodgett Technique

4.1.1 Surface Pressure-Area Isotherms

One of the most important properties of a monolayer is given by a chart of the surface pressure as a function of the area that is available to each molecule within the film. This is achieved by a LB trough under a constant temperature and is known as a surface pressure-area isotherm, often simply referred to as an isotherm. The film at the air-water interface gets compressed at a constant rate while the surface pressure is monitored continuously. Parameters like temperature or compression rate can impact the progression of the isotherm chart (Fig. 2.16). The recording of an isotherm of a known material can also be understood as a quick check to verify the validity of all experimental conditions. Reproducibility of the isotherm is a key feature to reproducible subsequent experiments with transferred Langmuir films.

The charts in Fig. 4.1 show a number of distinct features that are immediately apparent on examining the isotherms. The isotherms were recorded for DiynePC, but at different subphase temperatures. The compression rate for LB experiments was $100\,\mu m\,s^{-1}$ per barrier, if not stated otherwise. Using two barriers of $190\,mm$ width, $50\,\mu l$ lipid solution of $2\,mg\,ml^{-1}$, and a molar mass of DiynePC of $914.284\,g\,mol^{-1}$ the compression rate per molecule is 30–$40\,\text{Å}^2$/molecule/minute, which is commonly used.[202]

After the gaseous phase, characterized by a low surface pressure, the isotherm of $12\,°C$ subphase temperature showed a continuous transition by an increasing slope, representing a direct phase transition to a condensed phase. This is a result of a subphase temperature below the triple point of DiynePC ($T_c = 20\,°C$).[225]

The isotherm of DiynePC at a subphase temperature of $23\,°C$ (Fig. 4.1) showed a coexistence plateau between the liquid expanded and liquid condensed phases.

A transition to a solid phase was not observed and is not reported for DiynePC in literature.[226] This can be compared to the behavior of unsaturated fatty acids like oleic acid (Fig. 2.17), which also lack of a solid phase. In general, this type of isotherm is most frequently observed when studying molecules in which some distruption of the hydrophobic chain causes a difficulty in packing.[102]
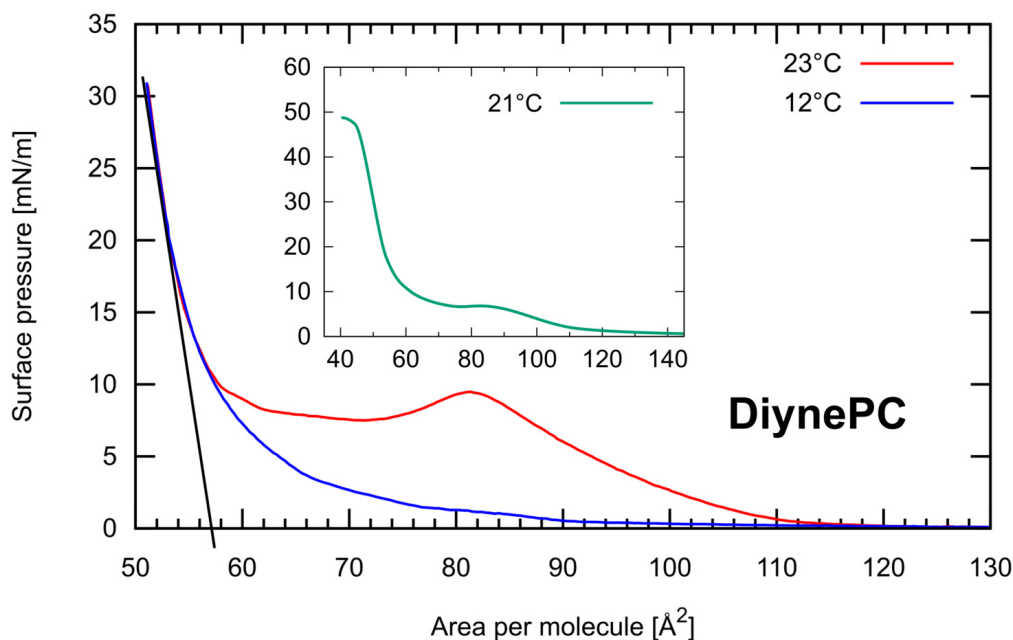
Figure 4.1: Isotherms of DiynePC, subphase temperature 12 and 23 °C. The isotherm at 12 °C showed a direct transition from the gaseous phase to the liquid condensed phase, whereas a liquid expanded phase was found for the isotherm at 23 °C with a bump in the beginning, which may be caused by impurities.[225] The linear part of the isotherm was extrapolated to zero surface pressure, exhibiting a value of $57\,\text{Å}^2$ per molecule. The inset shows a complete isotherm of DiynePC, where the collapse of the monolayer occurred at $48\,\text{mN}\,\text{m}^{-1}$. Compression rate: $30\text{--}40\,\text{Å}^2$/molecule/minute.

DiynePC exhibited a comparatively large molecular area $(57\,\text{Å}^2)$ in the condensed phase and a low triple point temperature in comparison to a similar fully saturated phosphocholine like DPPC $(47\,\text{Å}^2,\ T_c = 41\,°\text{C})$.[227] These properties are attributed to the presence of the diacetylene groups. Their size and the related kink in the molecule geometry affect the packing of the molecules.[225] The three above mentioned phases can clearly be shown and identified by fluorescence microscopy.[225,228]

The isotherm of PTPE (Fig. 4.2) came with a featureless character, comparable to DiynePC at 12 °C. The gaseous phase transferred directly to a condensed phase for the same reasons as DiynePC. The linear part of the isotherm was extrapolated to zero surface pressure and it resulted in an area per molecule of $66\,\text{Å}^2$, which is larger than the value for DiynePC, though the PC is larger than the PE headgroup.[229] The difference of molecular area may be the result of the combination of the diacetylene group and the palmitoyl chain in the PTPE lipid. While a close packaging of identical hydrocarbon chains seems reasonably, two different chains do not. A comparison of isotherms of
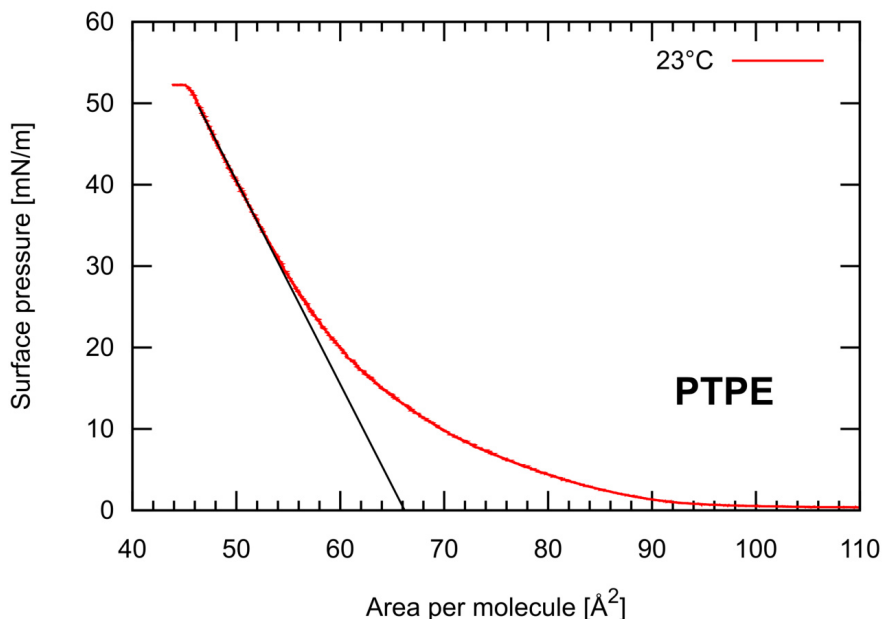
Figure 4.2: Isotherm of PTPE, subphase temperature 23 °C. The isotherm at 23 °C showed a direct transition from the gaseous phase to the liquid condensed phase. The linear part of the isotherm was extrapolated to zero surface pressure, exhibiting a value of 66 $\mathring{A}^2$ per molecule. The collapse of the monolayer occurred at 52 mN m^{-1}. Compression rate: 30–40 $\mathring{A}^2$/molecule/minute.

1,2-Dipalmitoylphosphatidylcholine and 1-Palmitoyl-2-caproylphosphatidylcholine for example, show a much steeper condensed phase for the symmetric phospholipid and a smaller molecular area compared to the asymmetrical molecule.[125] This supports the concept of a larger molecular area of PTPE due to its different chains. Varying the subphase temperature did not change the shape of the isotherm of PTPE ($T_c = 23$ °C)[36] and result in no phase transition plateau.

4.1.2 UV Polymerization of Diacetylene Lipids

UV-polymerized lipids were utilized in this thesis to improve the mechanical properties of lipid membranes. The polymerization of the lipids was carried out at the air-water interface of a Langmuir-Blodgett trough, and on substrates for spectroscopy experiments. The transfer to a supporting substrate was performed by either the Langmuir-Blodgett (LB) or the Langmuir-Schaefer (LS) technique. The process of conformational change from the monomer to the polymer is described in Fig. 3.7. Briefly, the polymerization of the Langmuir monolayers result in a conformational

change of the hydrocarbon chains of the lipids.[205] AFM studies (Okazaki et al.) revealed a thinner film thickness after polymerization which supports the accepted model of polymerization mechanics of polydiacetylenes.[230] As a result, the area per molecule in the polymerized Langmuir monolayer is of a higher value, or, for a fixed surface area, the pressure increases.[231] Consequently, the surface pressure is suitable to monitor the polymerization.
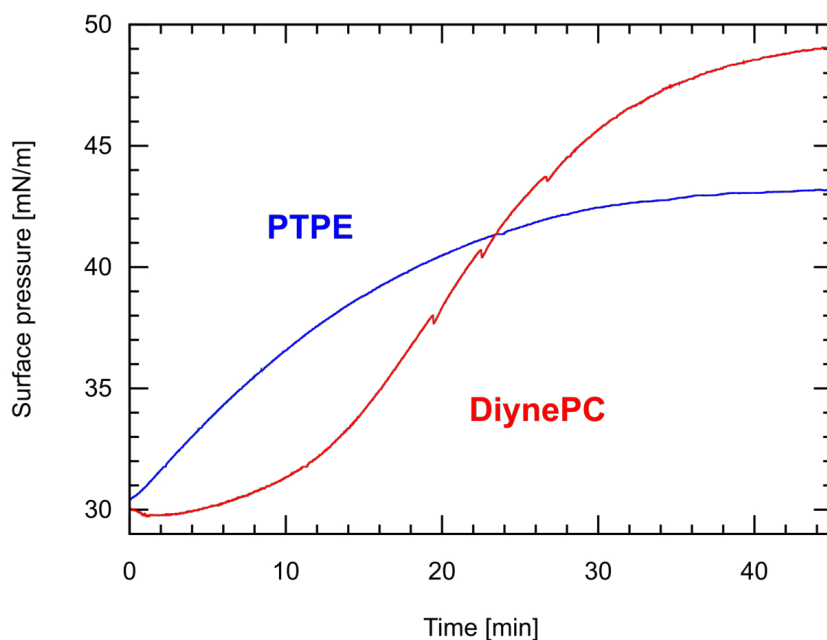

Figure 4.3: The surface pressure was monitored during polymerization of PTPE and DiynePC. The progressing polymerization of PTPE started at high speed and finally reached a saturation level, when most of the monomeric molecules were cross-linked, whereas the polymerization for DiynePC was retarded in the first 10 min of the illumination, but reached higher values in the final. Jags in the chart of DiynePC are often caused by sudden rearrangements in the film.[203]

At the air-water interface, monolayers of PTPE and DiynePC were compressed to $30 \, \text{mN} \, \text{m}^{-1}$. Polymerization was performed under constant area conditions with a fixed area per molecule (PTPE: $54 \, \text{Å}^2$ per molecule, DiynePC: $52 \, \text{Å}^2$ per molecule). This experimental setup is comparable to a film that is polymerized on a solid substrate and therefore stationary.[231] Successful polymerization of diacetylene molecules by UV light irradiation requires them to be arranged at a proper distance from each other.[232] However, steric rearrangements in the film during the polymerization can also be monitored in a constant pressure mode. The increasing area per molecule

can be investigated directly, as the barriers of the trough are give way the expanding Langmuir film (constant pressure mode).[233]

The polymerization kinetics that were measured by monitoring the surface pressure, exhibited different characteristics for DiynePC and PTPE. The rate of polymerization for PTPE was at its maximum right in the beginning as expected from an approximately first order kinetics, whereas the polymerization for DiynePC was retarded in the first 10 min of the illumination exhibiting a more sigmoidal dependence.[234]

It is known and accepted, that the polymerization starts by UV-induced formation with a free radical as initiator.[235] Chain propagation by adding monomer units and termination by recombination with another radical are therefore in direct competition. As a consequence, the frequency of termination events depends on the amount of free radicals per unit area.[235]

Because DiynePC has a high density of diacetylene groups per unit area, chain termination during polymerization can occur very likely in the beginning. This also explains the observed retarded polymerization of DiynePC in the first 10 min of illumination.

4.1.3 Spectroscopy of Lipid Adlayers

Polymerized lipids contain great amounts of conjugated systems with large π-systems, which are known for their absorption in the ultraviolet region.[236] Systems of large conjugated double bonds absorb photons of longer wavelength and the color of the compound ranges from yellow to red color.[237] The long conjugated hydrocarbon chain in beta-carotene is responsible for the strong orange color of carrots and tomatoes. Therefor, spectroscopic investigations were performed to monitor conformational changes.

UV-VIS Spectroscopy

A UV-VIS spectrometer was used to study the dynamic properties of the polymerization of DiynePC and PTPE. Commonly, spectroscopic analysis is carried out using a cuvette that contains a solution. However, the polymerization of diacetylene is restricted to areas in which the molecules are regularly packed in very specific arrangements.[238] Therefore, investigation of the lipids was performed in the form of a dried droplet applied to the outer face of a UV-VIS quarz cuvette. When the light of the spectrometer passes the residuum of the lipid solution on the cuvette, the absorbance E_λ is simply calculated from the intensity difference to a clean reference cuvette in a

second beam of the UV-VIS spectrometer by the Beer-Lambert law:

$$E_\lambda = \log_{10}\left(\frac{I_0}{I_1}\right) \tag{4.1}$$

First, droplets of several $100\,\mu l$ of DiynePC were applied to the viewing window of a quartz cuvette. Preparation and drying were carried out protected from light by aluminum foil. After an absorption spectrum of the sample was taken, illumination by a $4\,W$ UV lamp for 30–360 s was performed in a distance of $5\,cm$. This is about half the distance that was generally used with the LB trough and therefore results in a four times higher absorbed dose. This was done to shorten the exposition time with the UV-VIS to minimize further influences to the sample. It should be taken into account that the light of the UV-VIS detector is also causing a small amount of polymerization in the lipid with every data acquisition.
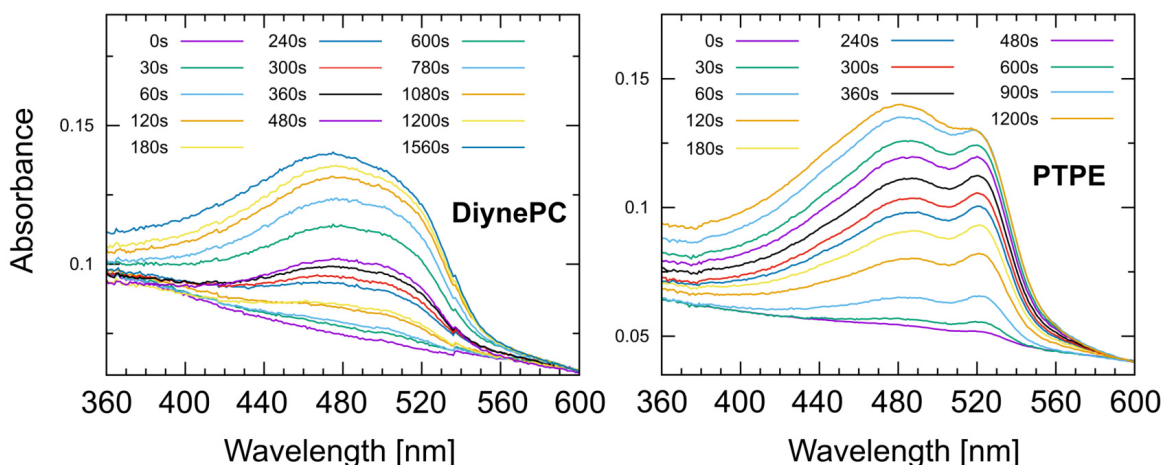
Figure 4.4: UV-VIS spectra of DiynePC and PTPE. The total time of UV illumination of each chart is given. The arise of absorption is due to polymerization and caused by a conjugated system with large π-systems in the polymer. The kink at $540\,nm$ in the chart of DiynePC is caused by the lamp change during the measurement. The magnitude of the absorbance depends on the amount of substance that was used, and is therefore neglectable.

The absorption of blue light by the lipid polymer is progressing in the process of polymerization, verified by the data of the UV-VIS spectrometer in Fig. 4.4. As the time of polymerization is progressing, the increase in absorption is reaching a final state. This is supported by observations made with the LB trough in Fig. 4.3.

The dynamic process of the polymerization can be illustrated by plotting a distinct

absorption wavelength versus the temporal development. In Fig. 4.5 the development of the absorption at 520 nm for PTPE, and 477 nm for DiynePC is shown. The rate of polymerization for PTPE is at its maximum right in the beginning, which is expected from a radical polymerization, whereas the polymerization of DiynePC is retarded.

The results are in good agreement with Fig. 4.3 and are supporting the concept that the frequency of termination events in the radical polymerization depends on the amount of free radicals. DiynePC has a higher density of diacetylene groups per unit area and chain termination can occur very likely in the beginning of the polymerization.

Since the experimental setup of the bulk lipid in the UV-VIS spectrometer is different from the LB trough, the data is not completely comparable. Furthermore, the absolute magnitude of the absorbance depends on the amount of substance that was used. The UV-VIS experiments of PTPE and DiynePC were performed on droplets of lipid solution, consequently the amount of lipids that were used for spectroscopy was different for both lipids.
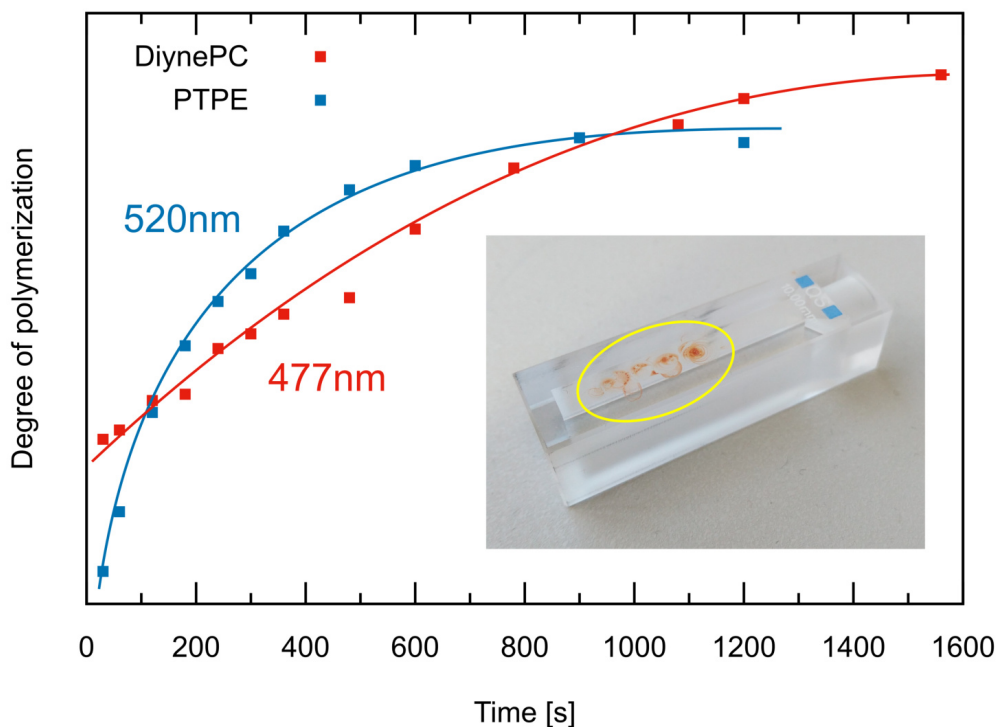

Figure 4.5: The charts illustrate the progression of polymerization, based on the data from Fig. 4.4. The absorption of the respective lipid at a distinct peak is plotted versus their temporal development. In the small insert, a cuvette featuring polymerized DiynePC is shown (yellow circle), which exhibits an intense red color from only a few droplets.

Infrared Spectroscopy

Monolayers were investigated before and after irradiation by infrared spectroscopy to study the chemical conversion. The structure of the lipid monolayers were characterized by FTIR spectroscopy using germanium in an attenuated total reflectance (ATR) setup. The lipid monolayer was transferred to the substrate by the Langmuir-Schaefer (LS) technique and dried afterwards at room temperature in the dark to avoid any polymerization.

The spectrum of DiynePC showed the characteristic signals of lipids with bands originating from C-H stretches at 2960–2850 cm^{-1}, from C=O stretches at around 1730 cm^{-1}, and from C-H bends at 1460 and 1378 cm^{-1}, as described in the literature.[218, 239, 240] Signals at 1485 and 1262 cm^{-1} arises from the headgroup.

The direct comparison to a spectrum of Dipalmitoylphosphatidylcholine (DPPC), which is a similar lipid without any diacetylene groups, reveals that the bands of DiynePC are broadened with a slight upshift in frequency of C-H stretch and a downshift of C=O (Fig. 4.6B). These bands are sensitive probes for changes in the packing, flexibility, and chemical structure of the lipids by the diacetylene moieties. Here, one contribution to the broadening is an additional band at 2937 cm^{-1} caused by the chemical variation.[218]
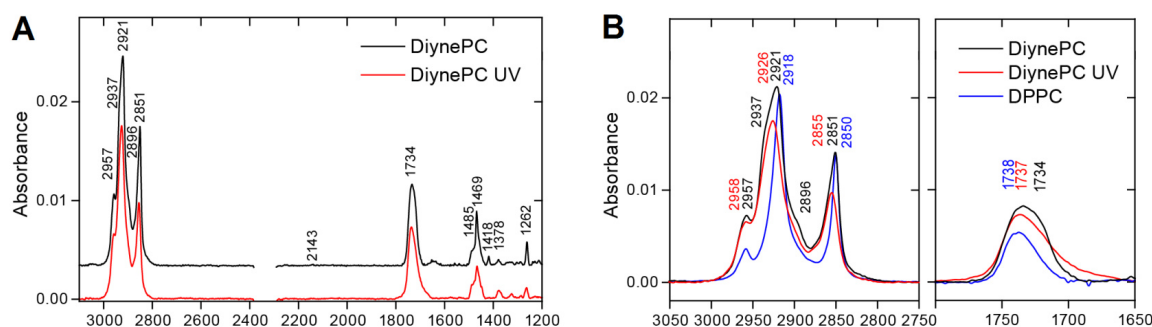

Figure 4.6: FTIR absorption spectra of lipid monolayers on a germanium substrate. (A) DiynePC was investigated in the dark and after irradiation with UV light. The polymerization induced only minor changes in the overall band pattern. The signal of residual atmospheric CO_2 at 2349 cm^{-1} was removed for clarity. (B) The spectral regions of C-H stretch and C=O stretch were selected for direct comparison of DiynePC without and with polymerization. Spectra were scaled to the integral of the C=O band. Upshifts in frequency and a decrease in absorbance were observed after polymerization. Both vibrations are sensitive to changes in the structure and packing of the lipids. A spectrum of DPPC was added for comparison and scaled by 0.5 for clarity.[36]

The UV-irradiated DiynePC showed the same overall band pattern as without treatment. The C=O and C-H stretches respond to the irradiation by a small upshift in frequency. For further analyzes of the chemical conversion taking place by irradiation, a more detailed investigation of the signal of the diacetylene group was performed. Previous FTIR spectroscopic analyses of bulk diacetylenic acids as model compounds revealed a signal at around $2139\,cm^{-1}$ that was assigned to the asymmetric stretch by quantum chemical calculations.[241] A very small signal of the monolayer at $2143\,cm^{-1}$ with a shoulder at $2150\,cm^{-1}$ was revealed that rises with increasing surface pressure during deposition from $10\text{–}30.5\,mN\,m^{-1}$ and then remained constant for a further increase to $45\,mN\,m^{-1}$ (Fig. 4.7A). Scaling the spectra to the amount of lipid using the C=O band integral, all three signal strengths were equal in intensity. This supports a differentiation of the signal from the noise level.
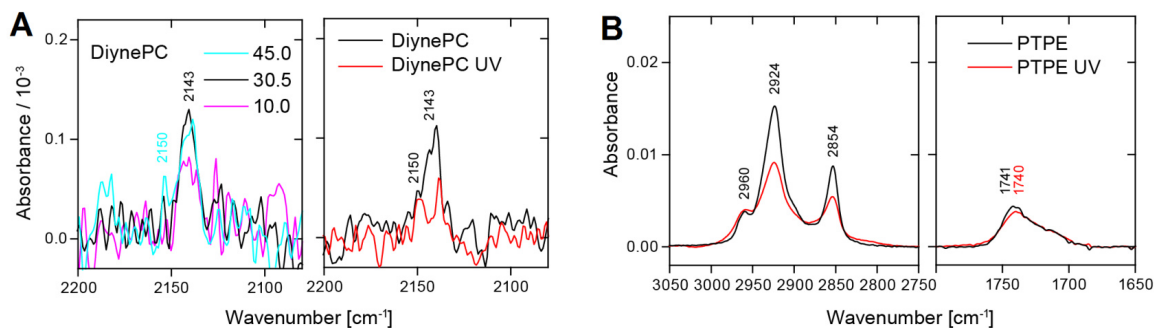

Figure 4.7: FTIR absorption spectra of lipid monolayers on a germanium substrate. (A) DiynePC was deposited at different surface pressures. An increase in signal at $2143\,cm^{-1}$ was found with an increase in pressure from 10.0 to 30.5 and 45 mN/m. This band is assigned to the asymmetric stretch of the diacetylene group. The signal strongly decreased after UV irradiation, which provides evidence for the conversion of the diacetylene. Four and three independent experiments were averaged without and with irradiation, respectively. (B) PTPE was investigated in the dark and after irradiation with UV light. Spectra were scaled to the integral of the C=O band. Changes in frequency by irradiation were observed that were smaller than for DiynePC.[36]

Irradiation of the DiynePC strongly reduced the signal of the diacetylene group and thereby provides evidence for a chemical conversion of diacetylene in the monolayer. However, this band should not be confused with that from the symmetric stretch of diacetylene, which has been observed previously by FT-Raman spectroscopy on model compounds in the bulk at around 2257 and $2220\,cm^{-1}$, respectively.[215,241] Signals of the product were not found in the analyses, which can be attributed to the small

signal strength and the expected broadening by a distribution of polymeric aromatic groups formed according to the reaction model (Fig. 3.7). An overview of the band assignments for the DiynePC monolayer is given in Table 4.1.

Analog to DiynePC, a monolayer of PTPE was analyzed by FTIR spectroscopy before and after irradiation with UV light on a germanium substrate (Fig. 4.7B). Both C-H and C=O stretches were slightly upshifted in frequency as compared to DiynePC. The band of the C=O stretch shows a strongly asymmetric distribution which is attributed to the two chemically different tails of the lipid. UV irradiation led to very minor changes in the band positions with a downshift of the C=O band by only $1\,\mathrm{cm}^{-1}$. Besides, the relative absorption of the C-H stretches with respect to the C=O stretches was reduced by illumination. These deviations might be attributed to changes in orientation relative to the substrate plane and to a chemical conversion.

Table 4.1: Selected FTIR bands of the DiynePC monolayer and their assignment.[a]

DiynePC monolayer	DiynePC vesicle[b]	DiynePC powder[b]	DiynePC theory[c]	lipids general[d]	assignment
2957	2956	2957	2953	2956	CH$_3$ asym. stretch
2937	-	2939/2934		-	CH$_2$ asym. stretch close to diacetylene
2921	2926	2917	2922	2920	CH$_2$ asym. stretch
2896	2899	2895		-	CH$_2$ sym. stretch close to diacetylene
-	-	2872		2870	CH$_3$ sym. stretch
2851	2854	2850	2873	2850	CH$_2$ sym. stretch
2143	-	-	2162	-	diacetylene asym. stretch
1734	-	-	1818	1730	C=O stretch

[a]Band positions are given in cm^{-1}. [b]Lee.[218] [c]Roman and Baranska[241]
[d]Tamm and Tatulian and references therein[240]

Conclusion

The chemical changes in the DiynePC monolayer were more easily detected than in PTPE because of the two reactive groups present. Direct changes by irradiation were identified by resolving the diacetylene signal and its reduction in the monolayer. Ad-

ditionally, the light-induced modifications in packing and structure of diacetylene-containing lipids were indirectly monitored via the C=O and C-H signals.

4.1.4 AFM of Lipid Adlayers

Film deposition and polymerization of lipid layers were monitored by parameters during the preparation with the LB trough. Based on the surface pressure, the progressing polymerization was recorded and the dynamic could be investigated.

Thorough sample preparation was performed and clean equipment was used to ensure optimal film deposition. The quantity of a film deposition can be studied by the area that is consumed by the moving barriers during the transfer. By keeping the surface pressure constant, the consumed surface area reflects the amount of film area that is transferred to the sample, which is called *transfer ratio*.[203] However, the quality of the transferred film often staid unclear. To provided further insights into the transferred films, analysis of substrate supported monolayers was conducted by AFM.
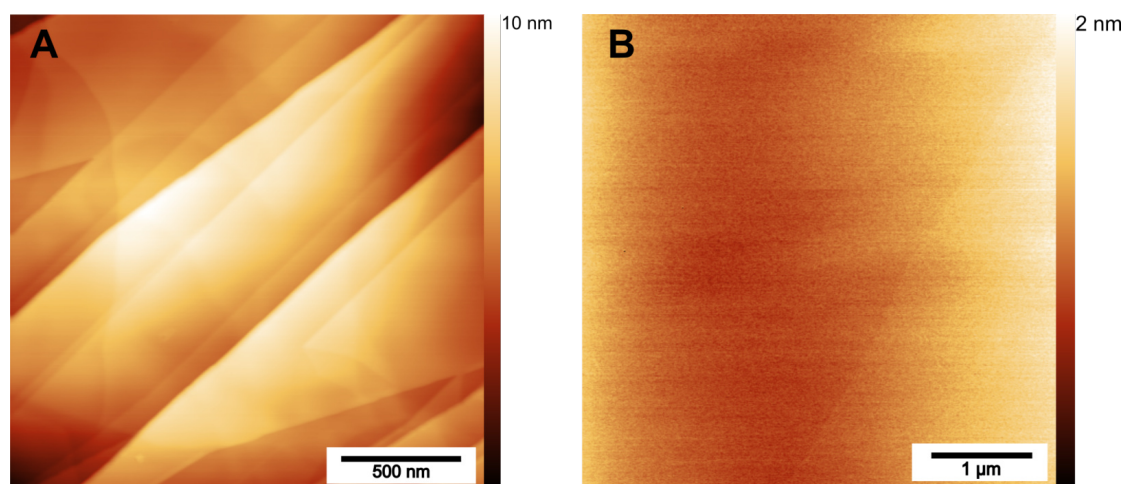
Figure 4.8: (A) AFM image of clean HOPG. Typical appearance with steps and edges. (B) AFM image of clean mica. The surface is featureless except for one step starting in the upper right corner.

Samples of *mica* and *highly oriented pyrolytic graphite* (HOPG) were used as substrates for lipid monolayers. Mica and HOPG are standard substrates for AFM studies because of their atomic plane surface (Fig. 4.8). Mica is a group of sheet silicate minerals which have nearly perfect basal cleavage. HOPG is a material that consists of many atomic layers of carbon, highly oriented among each other. Atomically clean surfaces can be obtained by removing a surface layer with a piece of adhesive tape. No further

treatment is necessary. Because of the importance of the state of polymerization of lipids in this work, all images are marked by a small icon to clarify whether the sample had been prepared by UV illumination.

Lipid Monolayers on Mica

Samples of mica were coated with polymerized PTPE (Fig. 4.9) and investigated by AFM. It turned out that large areas of mica were completely covered by the lipid. Due to a contamination on the substrate (vertical white line in Fig. 4.9A), the transfer was interrupted and areas of bare mica became visible. A line profile in a closer view (inset in Fig. 4.9B) was applied to determine the thickness of the lipid layer to be of 3.0 nm. By the phase contrast image, different material properties are revealed (Fig. 4.9C). This confirms that the images actually show areas of bare mica and a large-scale monolayer of PTPE. The transfer ratio of lipids to mica, which can be calculated from the trough parameters, was higher than 90 % for all transfers.
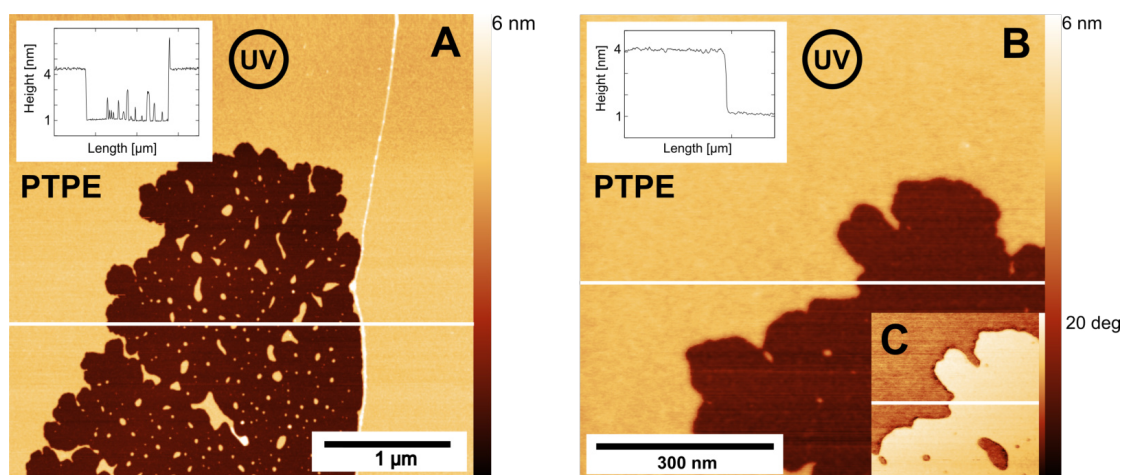
Figure 4.9: Monolayers of polymerized PTPE were transferred to mica by LB technique at $41.7 \, \text{mN} \, \text{m}^{-1}$ and 20 °C. (A) A line profile through a defect in the continuous film reveals its height of 3.3 nm. (B) A detail view of the same defect. The film thickness is 3.0 nm. (C) The phase contrast image proves that the lower area exhibits different material properties.[242] Consequently, mica is covered by PTPE.

Lipid Monolayers on HOPG

The orientation of a lipid monolayer on HOPG differs from that on mica. Because of the hydrophobic character of HOPG, the hydrophilic lipid headgroup faces away from

the HOPG. Lipid films were transferred to HOPG by the LS technique.

The unpolymerized lipid layers of DiynePC and PTPE that were transferred to HOPG showed a well organized two-dimensional network of molecularly ordered domains (Fig. 4.10). The domains exhibited different orientation angles of 60° or 120° between them. For better visualization of the dominating orientation, a 2D-Fourier Transform (2D-FFT) was performed on each AFM image.
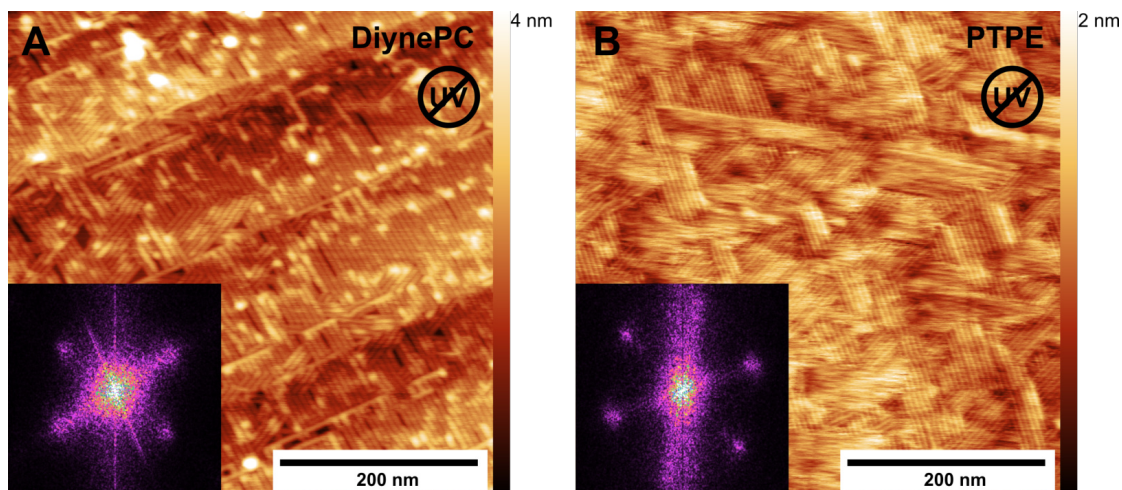

Figure 4.10: Monolayers of unpolymerized DiynePC (A) and PTPE (B) on HOPG. In comparison to monolayers on mica, the lipids exhibited organized structures showing a two-dimensional network of molecularly ordered domains. A 2D-Fourier Transform (2D-FFT) is shown (insets), indicating the presence of certain angles in the AFM image.

Briefly, FFT converts a signal from its original domain to a representation in the frequency domain. Two dimensional pixel information is transformed by a 2D-FFT to a polar representation, where information is provided based on radial distance and angle. Any periodicity in the real image is represented at a certain radial distance (and angle) from the center.

The 2D-FFT images in Fig. 4.10 confirm the 60° and 120° geometry of the structures. An additional frequency shifted by 30° in the inset in Fig. 4.10A represents parallel steps in the HOPG substrate under the lipid adlayer, which cross the image from bottom left to top right.

Investigations of many different self-assembling molecules on substrates have been reported in the past decades.[135, 243] AFM[244] and scanning tunneling microscopy (STM)[245] studies revealed that molecules like alkanes, alcohols and fatty acids organize in lamellae with the extended alkyl chains oriented parallel to a lattice axis within the basal

plane of graphite,[134, 246] although amphiphilic molecules are orientated vertically at the air-water interface of the Langmuir trough in general before the transfer process.
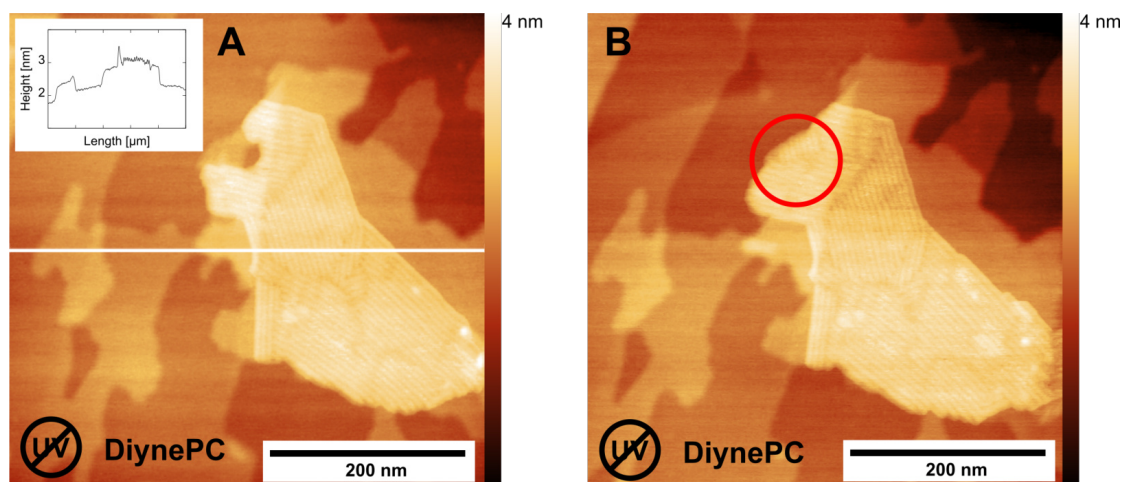

Figure 4.11: A monolayer of unpolymerized DiynePC on HOPG. (A) Structures and domains of lipids are visible with a height of 0.6 nm indicating a layer of horizontally deposited molecules with their long axis in plane with the surface. (B) A second AFM image was taken directly afterwards, exhibiting a molecular rearrangement (red circle). This image was taken by F. Heising under the authors supervision.

Molecular rearrangements of the transferred film material are reported.[247, 248] Structural rearrangements within LB films on silicon single crystals have been reported.[249] Molecular structures and domains (Fig. 4.10) are the result of these mobile monolayer molecules after the LB preparation. In this work, rearrangements even during the AFM measurement were detected (Fig. 4.11).

Although, amphiphilic molecules are orientated vertically at the air-water interface of the Langmuir trough, layers of unpolymerized DiynePC and PTPE were found to be arranged in a horizontal configuration. Line profiles (4.11) revealed that the lipid adlayer on HOPG was 0.6 nm thick, which is much smaller than the DiynePC chain length ($\approx$2.5 nm).[230] Thus, a monolayer structure with vertically oriented hydrocarbon chains can be excluded. However, the film thickness of 0.6 nm is consistent with the DiynePC chains lying parallel to the HOPG basal plane.[250]

A close-up scan of unpolymerized DiynePC and PTPE on HOPG is shown in Fig. 4.12. The length of periodicity between neighboring lamellae was estimated to be 6.2 $\pm$ 0.6 nm for DiynePC, and 6.0 $\pm$ 0.5 nm for PTPE. This is about twice the length of a PTPE molecule (Fig. 4.9).
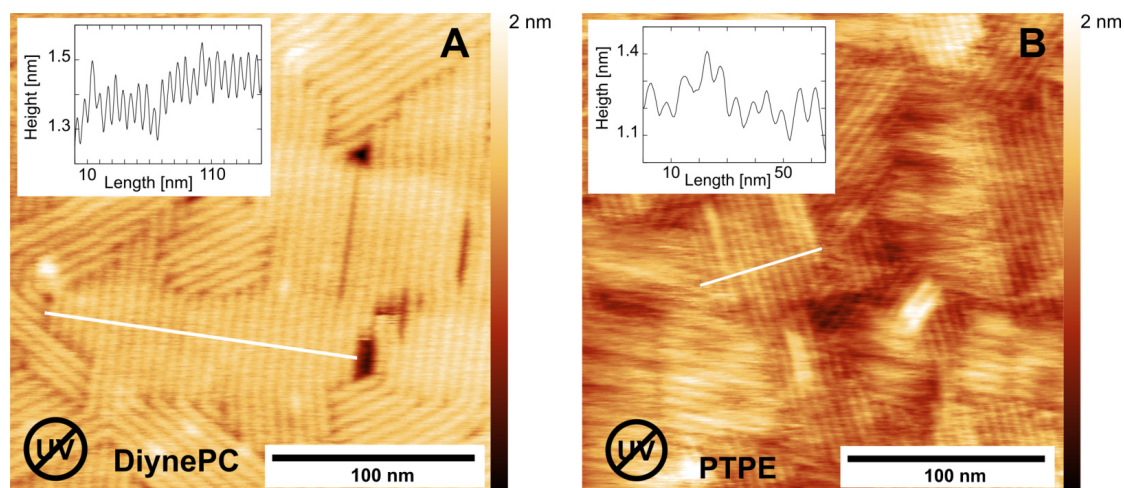
Figure 4.12: AFM images of unpolymerized layers of DiynePC (A) and PTPE (B) coated onto HOPG. Triangular pattern of lipid domains are observable, showing well ordered lamellae, displaying the threefold symmetry of the HOPG lattice. Structural periodicity is $6.2 \pm 0.6\,\mathrm{nm}$ (DiynePC) and $6.0 \pm 0.5\,\mathrm{nm}$ (PTPE), line profiles are given in the insets.
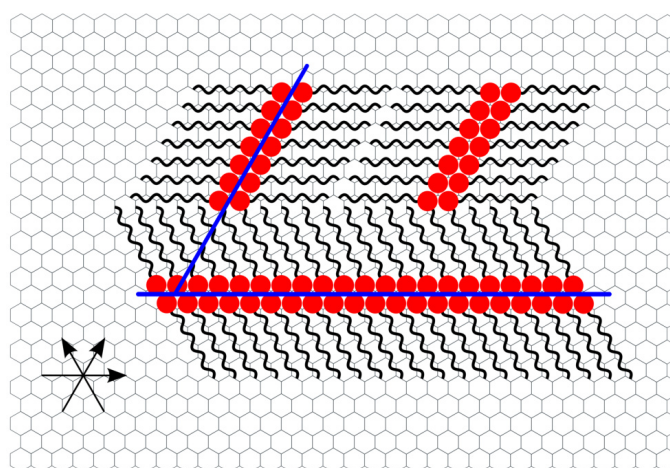
Figure 4.13: Scheme of a monolayer of lipids on HOPG. Red circles label headgroups and curved lines represent hydrocarbon chains. The arrows denote the crystallographically equivalent graphite axes with 3-fold symmetry. The hydrocarbon chains orient horizontally along the substrate axes parallel to each other, while the head groups organize into straight lamellae.

Based on the chemical structure (Fig. 3.6), DiynePC is slightly larger. The structural periodicity of the lipid adlayers supports the accepted model[245, 251] of horizontally arranged lipids in a head-to-head configuration (Fig. 4.13). There, the alkyl chains of lipids are packed parallel in a side by side manner. The head groups of the molecules

then form parallel lamellae, which appeared higher in the AFM image because of their size and polar character. The molecular alkyl axis and the lamella direction cross each other at an angle, which is reported to be 60° or 90°, depending on the molecule.[251]

Next, polymerized monolayers of DiynePC and PTPE were transferred to HOPG. The DiynePC monolayer was first polymerized and then transferred by LS technique to HOPG (Fig. 4.14A). It showed a patchy layer with few defects. The close-up verified that no alignments are visible (Fig. 4.14B), except for very few remaining structures in the voids of the polymerized film. Those aligned structures were most likely caused by unpolymerized lipids, which could freely migrate during LS transfer and thus moved in the voids of the polymerized DiynePC layer. The film of polymerized DiynePC was 2.7 nm thick, which is in good agreement with other AFM investigations.[230] There, a double layer of polymerized DinyePC on HOPG was found to be 5.1 nm thick.
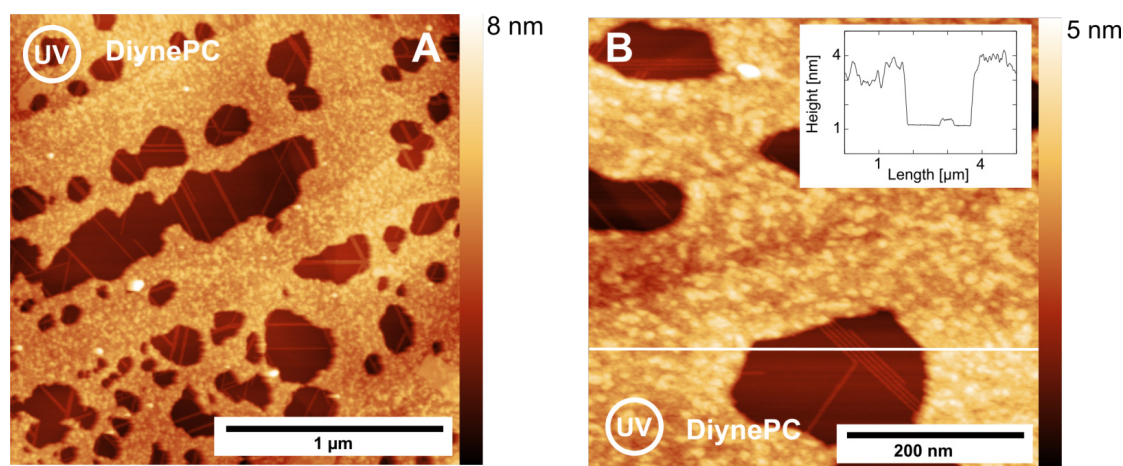

Figure 4.14: AFM image of polymerized DiynePC monolayers on HOPG. (A) No geometrically alignments are visible, except for very few lamellae in the uncovered areas. (B) The thickness of the layer is 2.7 nm and 0.3 nm for the lamellae.

In comparison to an unpolymerized layer, a smaller thickness of the polymerized layer is expected. This is caused by the mechanism of polymerization (Fig. 3.7), where the vertical molecular axis is tilted at a 36° angle.[252]

A monolayer of polymerized PTPE on HOPG is shown in Fig. 4.15. UV illumination was performed before LS transfer. Fig. 4.15A shows a complete surface coverage with only a few defects. The film looks homogeneous and grainy, similar to a polymerized layer of DiynePC. However, the close-up in Fig. 4.15B reveals lamellar structures that are not limited to defect areas but throughout the entire film.

The 2D-FFT inset is based on the intact film only and the defect areas are excluded.

The 2D-FFT confirms a slight domination of certain angles in the intact film and indicates a different behavior from a monolayer of polymerized DiynePC.
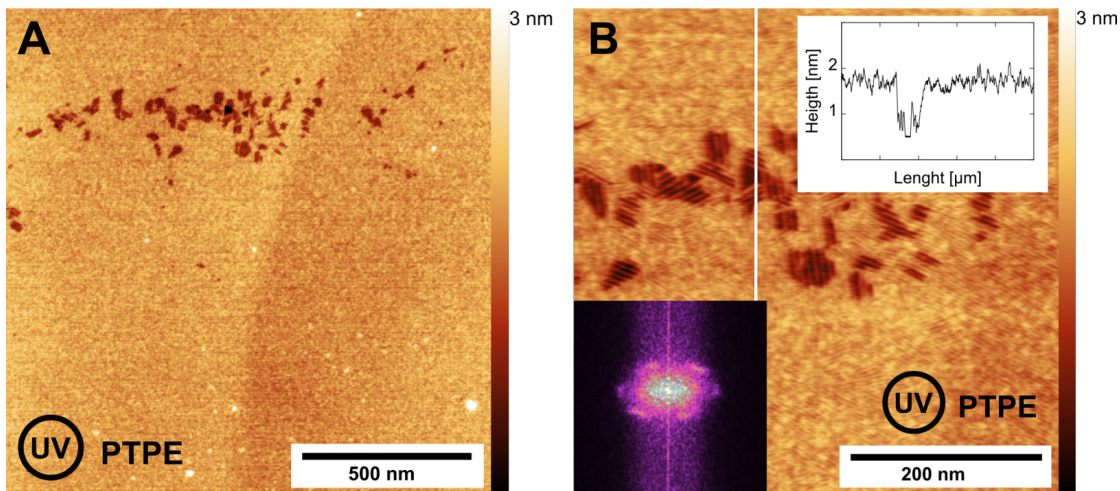

Figure 4.15: AFM image of polymerized PTPE monolayers on HOPG. (A) No geometrically alignments is visible, except for very few lamellae in defective areas. (B) At a close view of the same sector, slight lamellar structures in the intact film become visible. This is confirmed by a 2D-FFT analysis of the intact film. The thickness of the layer is 1.3 nm.

The different appearance of polymerized adlayers on HOPG is most likely caused by the higher density of polydiacetylenes in DiynePC compared to those of PTPE. Based on the molecular structure, a filamentous 1D-polymerization for PTPE is to be expected, whereas DiynePC lipids can polymerize in a 2D-mesh-like structure. Therefore, the resulting monolayer of polymerized PTPE remained more fluid-like and could align to the atomic structure of HOPG.

In contrast, adlayers of polymerized DiynePC exhibited a stiff and solid-like appearance with no molecular alignment to HOPG. This is most likely caused by the higher polymerization degree for DiynePC, containing more diacethylene groups per molecule. This concept is also supported by the film thickness of only 1.3 nm of a polymerized PTPE monolayer (DiynePC: 2.7 nm), which is not as rigid as polymerized DiynePC. Consequently, the film tends to align to the HOPG, reducing its thickness.

Conclusion

The AFM investigation of lipid layers on mica and HOPG confirmed successful transfers of unpolymerized and polymerized Langmuir films of DiynePC and PTPE. While lipid monolayers on mica showed homogeneous and featureless layers, monolayers on

HOPG revealed well organized films with a two-dimensional network of molecular ordered domains. The domains display the threefold symmetry of the HOPG lattice. The film thickness for unpolymerized monolayers was much smaller than the chain length of the lipid. Thus, a lying configuration of the lipids is assumed. The film thickness is consistent with the lipid chains lying parallel to the HOPG basal plane. The distance between neighboring, repetitive lamellae confirmed the accepted model of a head-to-head configuration. Polymerization resulted in a rigid film and prevented (DiynePC) or reduced (PTPE) the ability of self assembling.

4.1.5 Free-Standing Lipid Membranes

In the previous chapters, the successful polymerization of DiynePC and PTPE was verified by spectroscopic techniques and LB trough preparation. The quality and the appearance of the transferred Langmuir films were investigated by AFM and distinct differences were found. There, the monolayers were studied as adlayers in a supported setup on a substrate (HOPG, mica).

In the following chapter, the lipid monolayers were investigated in a pore-spanning setup, that is, free-standing. Supported by a perforated sample (TEM grid, Quantifoil), the mechanical properties of polymerized DiynePC and PTPE were investigated by helium ion microscopy (HIM) and AFM.

Measurements were performed under ambient conditions (AFM) and within a time period of 12 h after the LB preparation. Polymerization of lipid monolayers at the LB trough was carried out at a subphase temperature of 16 °C. After the preparation by LB transfer, the sample was dried at least 30 min under ambient condition. Subsequently, the sample was analyzed by HIM. Visualization by HIM was performed not only for high quality data, but also for a verification of a successful preparation of the polymerized lipid monolayer. Because AFM measurements are much more time consuming, HIM images were used to identity regions of high interest to be studied purposively by AFM afterwards.

Preliminary experiments were performed with 1,2-diphytanoyl-sn-glycero-3-phosphocholine (DPhPC) to evaluate the mechanical properties of a non-polymerizable lipid membrane. A *Quantifoil multi A* TEM grid containing various apertures (1 µm up to 2×8 µm^2 in diameter) was utilized as a supporting sample.

DPhPC is a phospholipid without any polymerizable groups and is often used as a model membrane, because of its unique properties, such as high chemical and physical stability, low water permeability, and no gel-to-fluid phase transition at ambient tem-

perature.[253] Mechanical behavior of pore-spanning membranes of DPhPC has been studied by AFM in aqueous environments.[254] There, highly ordered silicon substrate exhibiting pore radii ranging from 225–600 nm were utilized as a supporting material for free-standing lipid membranes.

Investigation with HIM

In contrast to membrane experiments in aqueous environments, a free-standing lipid membrane in air is much more fragile. Membranes of DPhPC are primarily stabilized by weak van der Waals interactions.[255] In this context, intact membranes of DPhPC were not to be expected in HIM.
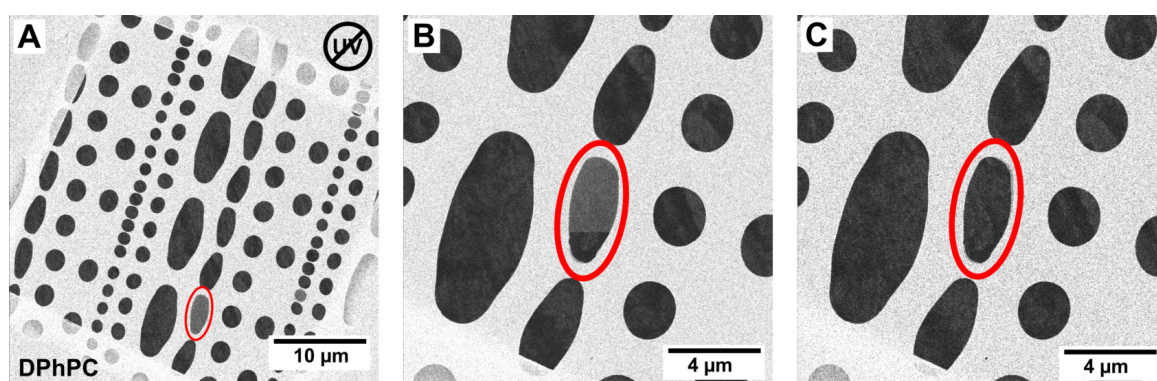
Figure 4.16: Free-standing monolayer of DPhPC on a Quantifoil grid. LB transfer at $40\,\mathrm{mN\,m^{-1}}$ and $16\,^{\circ}\mathrm{C}$. (A) Very few intact pore suspending membranes were found (red circle). (B) In a close-up, the membrane burst during the scan and created an (artificial) image of a half intact/broken membrane. (C) A further scan revealed the complete ruptured membrane.

Inspected in the HIM (4.16), free-standing membranes of DPhPC were found to be very unstable and disrupted instantly. AFM measurements were not performed.

Investigation of UV polymerized lipid membranes of DiynePC and PTPE in the HIM revealed successful formation of robust pore-spanning monolayers up to $8 \times 2\,\mathrm{\mu m^2}$. In contrast to the DPhPC monolayers, the membranes were found to remain intact for several hours both under laboratory and high vacuum conditions.

Fig. 4.17 shows polymerized membranes of DiynePC and PTPE taken by HIM, where apertures of various sizes are suspended. In rare cases, the polymerized monolayers were locally damaged during the scan with higher energy per unit area, allowing to investigate the behavior of forming defects. Although punctures were occurring, most parts of the membrane remained intact. Images of DiynePC membranes (Fig. 4.17A)

revealed a high beam resistance and stability. The geometry of defects (marked by a red circle) was irregular, indicating a high-grade cross-linked and stiff membrane.
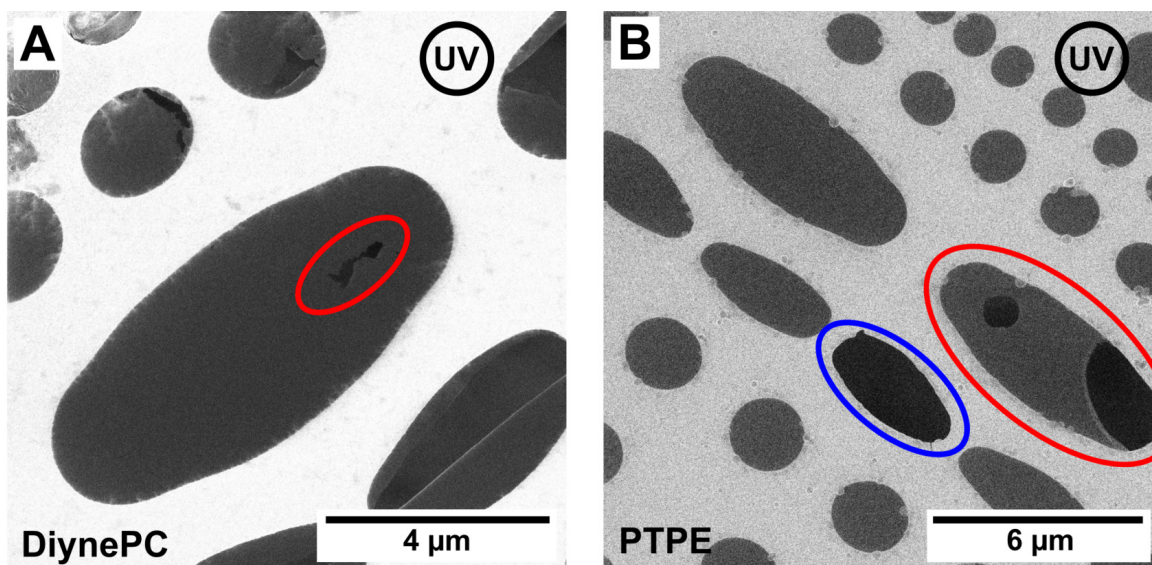

Figure 4.17: Images of polymerized DiynePC (A) and PTPE (B) lipid monolayers on a Quantifoil TEM grid. UV polymerization time: 45 min. Most membranes of DiynePC were intact, but some exhibited elongated ruptures (A) (e.g. red circle), ion dose: $7.25 \times 10^{13}\,\text{cm}^{-2}$. Membranes of PTPE (B) were intact, one pore (blue circle) is not covered, defects (red circle) are circular, ion dose: $5.44 \times 10^{12}\,\text{cm}^{-2}$.

In comparison, membranes of polymerized PTPE (Fig. 4.17B) showed less defects, which were exclusively circular and smooth in shape (red circle). One pore (blue circle) was not covered. While membranes of DiynePC got only locally damaged during a close-up scan, small ruptures of PTPE membranes ended up in a much larger defect of invariably circular shape. The HIM images highly support the assumed model of a stiffer DiynePC membrane, attributed to the higher amount of diacetylene groups per molecule in comparison to polymerized PTPE membranes.

Investigation with AFM

Membrane-covered and uncovered voids were also imaged with AFM. Successful formation of pore-spanning polymerized PTPE membranes can be seen in Fig. 4.18, where several apertures of a Quantifoil TEM grid are covered by polymerized PTPE. Apertures up to $8 \times 2\,\mu\text{m}^2$ could be scanned. Although there was a moderate interaction of the AFM-tip with the sample under ambient conditions, the membranes were kept intact during scanning. The line scan profile for PTPE taken from Fig. 4.18B reveals

a distinct downward bending of the membrane during AFM scanning as a consequence of the applied forces by the AFM cantilever and gravitational forces.
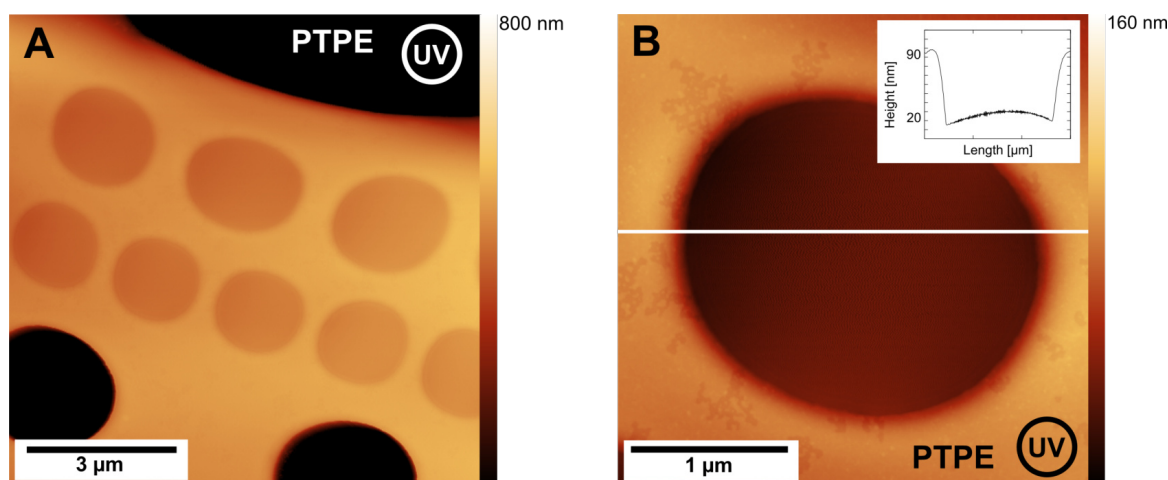

Figure 4.18: AFM scan of polymeric pore-spanning PTPE. (A) Several membranes up to $2\,\mu m$ in diameter are intact. (B) Close-up of a $2\,\mu m$ membrane, which bent down to $70\,nm$ along the line profile (inset). This is the same sample as in Fig. 4.17B.
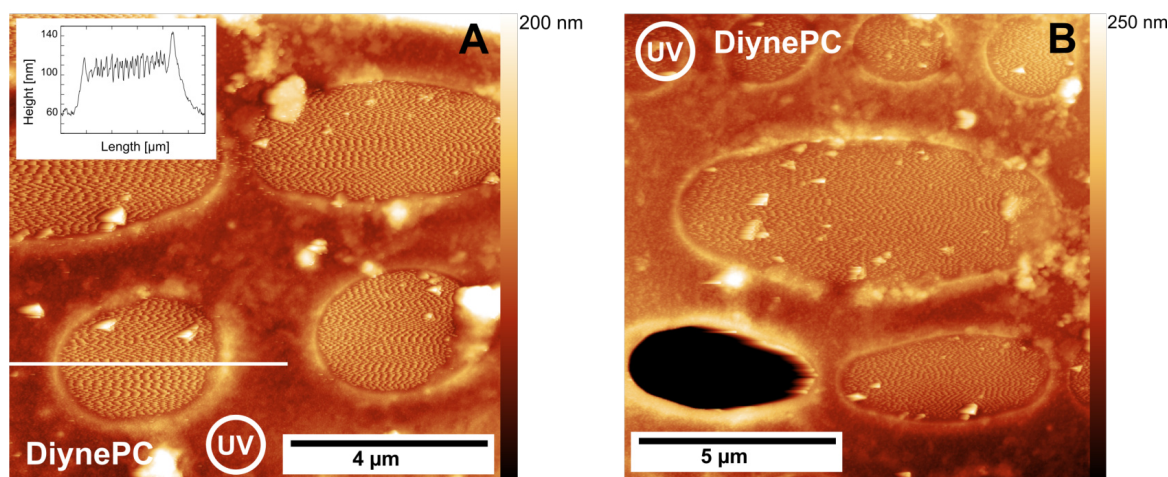

Figure 4.19: AFM scan of polymeric pore-spanning DiynePC. (A) Several membranes up to $4 \times 2\,\mu m^2$ in diameter were found to be intact. Oscillations of the membrane due to the tapping image mode and resulting resonance are visible. (B) An intact membrane of $8 \times 2\,\mu m^2$ is shown. In contrast to PTPE, the DiynePC membrane exhibited a constant height level with no sagging. This is the same sample as in Fig. 4.17A.

Pore-spanning membranes of polymerized DyinePC are shown in Fig. 4.19, where several intact membranes were covering the apertures of a Quantifoil TEM grid. Again, apertures up to $8 \times 2 \, \mu m^2$ could be scanned successfully. In contrast to PTPE membranes, the line scan profile for the polymerized DiynePC membrane in Fig. 4.19A exhibits a constant height level with oscillations of the membrane due to the tapping image mode and resulting resonance. These observations can be explained with a stiffer and more rigid DiynePC membrane, which complies with the higher density of polymerizable diacetylene groups available.

Conclusion

Free-standing polymerized lipid membranes of DiynePC and PTPE were prepared and characterized by HIM and AFM. Due to covalent bonds in the polymeric membrane, advanced mechanical properties allowed pore-spanning membranes in the order of micrometers, not achievable with ordinary lipid membranes. In contrast, unpolymerized DPhPC could not form stable membranes. The AFM investigation clearly revealed robust membranes for DiynePC and PTPE with different characteristics, and the mechanical properties could be attributed to the amount of diacetylene groups per molecule. This is also supported by AFM images of adlayers of DiynePC and PTPE on HOPG, where polymerized DiynePC exhibited a rigid structure after polymerization showing no alignment to the underlying crystalline structure of the HOPG. In contrast, polymerized PTPE organized into lamellae, indicating a flexible structure.

4.1.6 Layers of Single-Molecule Magnets

Single-molecule magnets are a class of molecules that show a hysteresis in their magnetization of pure molecular origin.[256] Molecules with a single molecular character keep a remnant magnetization after the external field is switched off. Such a remanence in the magnetization is known from ferromagnetic materials. In a conventional magnetic material, the remanence is a cooperative 3D effect, while it is of purely molecular origin in single magnetic molecules.[257]

Organizing and preparing such molecules into structured layers for various applications[258] can be performed with the Langmuir-Blodgett technique. By measuring the area per molecule at the air-water interface, molecular arrangements can also be studied. AFM images help to reveal further details of a substrate supported adlayer of molecular magnets.

Surface Pressure-Area Isotherms

This project is a collaboration with the group of Prof. T. Glaser, Inorganic Chemistry of the Chemistry Department, Bielefeld University. The properties of LB films of molecular magnets were investigated. This project was intended to be the initial experiments for the utilized molecule.
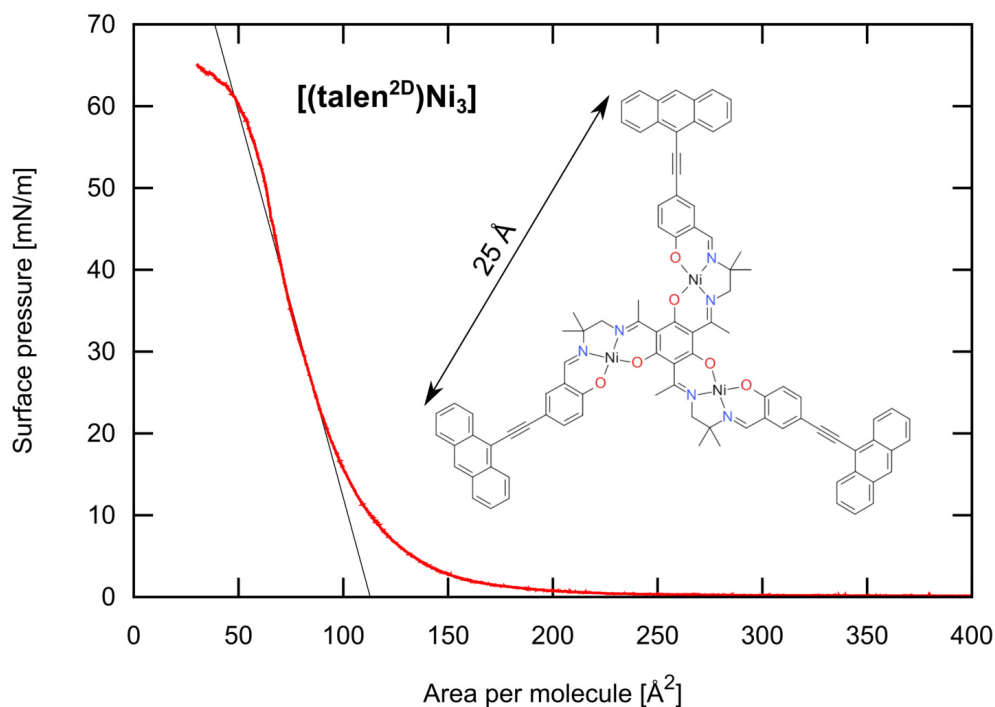

Figure 4.20: Isotherm of $[(talen^{2D})Ni_3]$ dissolved in chloroform. Subphase temperature: 25.6 °C, compression rate: $200\,\mu m\,s^{-1}$. Average molecular area (out of four isotherms): $118\,\text{Å}^2$. Inset: Molecular structure of the Ni^{II}_3 complex $[(talen^{2D})Ni_3]$.[257]

Synthesis of the single-molecule magnets was performed by Dr. J. Oldengott from the Glaser group. The single-molecule magnet used in this chapter is the Ni^{II}_3 complex $[(talen^{2D})Ni_3]$ with the molecular formula $C_{93}H_{72}N_6O_6Ni_3$. It consists of an inner magnetic core of three nickel atoms with three surrounding organic ligands (inset in Fig. 4.20). Three anthracene functional groups are attached via carbon triple bonds. By UV illumination, anthracene can photodimerize with adjacent anthracene groups of neighboring molecules.[259]

The Ni^{II}_3 complex $[(talen^{2D})Ni_3]$ has a molecular weight of $1545.69\,g\,mol^{-1}$ and exhibits a light orange color. The substance was dissolved in chloroform to a final concentration of $0.08\,mg\,ml^{-1}$ and stored at -20 °C in the dark.

A typical surface pressure isotherm is shown in Fig. 4.20. Extrapolation of the condensed phase revealed a molecular area of $118\,\text{Å}^2$ in this state. This is too small for a planar orientated molecule of $[(\text{talen}^{2D})\text{Ni}_3]$, which is of triangular shape exhibiting an edge length of $25\,\text{Å}$.

To gain a more detailed insight into the LB film and the molecular arrangements, AFM images of a transferred monolayer in the condensed phase of $[(\text{talen}^{2D})\text{Ni}_3]$ were taken.

Investigation by AFM

Langmuir films of $[(\text{talen}^{2D})\text{Ni}_3]$ were transferred by LS technique to HOPG samples at a film surface pressure of $40\,\text{mN}\,\text{m}^{-1}$ under ambient conditions and a subphase temperature of $23\,^\circ\text{C}$.
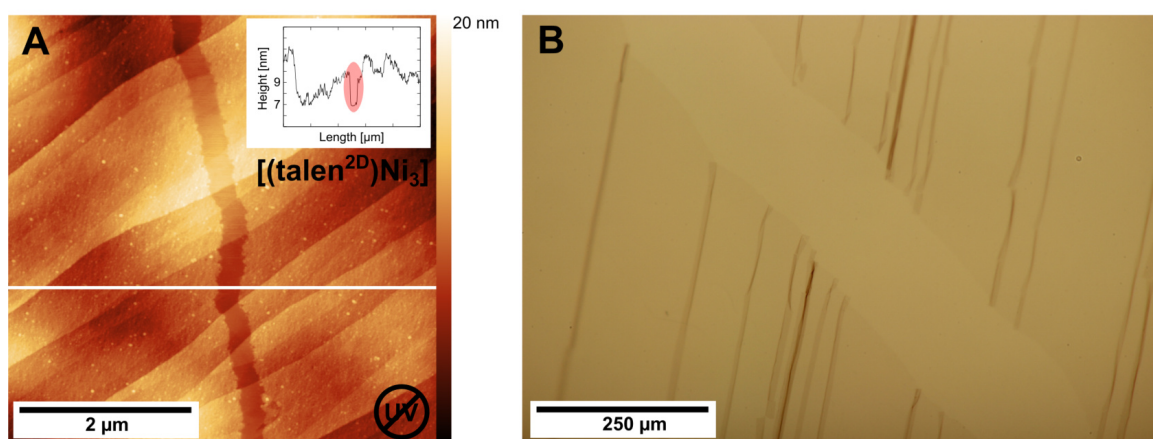

Figure 4.21: (A) AFM image of a $[(\text{talen}^{2D})\text{Ni}_3]$ monolayer on HOPG $(40\,\text{mN}\,\text{m}^{-1})$. Bare HOPG is visible due to a fissure in the monolayer, revealing the film height of 2.5 nm. (B) Light microscope image shows a folded film and a fissure.

First, the film was inspected in a light microscope, revealing a large area monolayer with folding and fissures in the film. Based on AFM images (Fig. 4.21A), the film thickness was determined to be 2.5 nm. This is far too high for a flat monolayer. However, such film thickness is reasonable in the case of an upright, lined up configuration of molecules across the surface. There, each $[(\text{talen}^{2D})\text{Ni}_3]$ molecule is orientated in a vertical manner at the air-water interface.

Further AFM measurements were performed using a smaller surface pressure of the Langmuir film. At $20\,\text{mN}\,\text{m}^{-1}$, a film height of only 0.6 nm was measured in the monolayer (Fig. 4.22). This is consistent with a film of horizontally arranged, planar
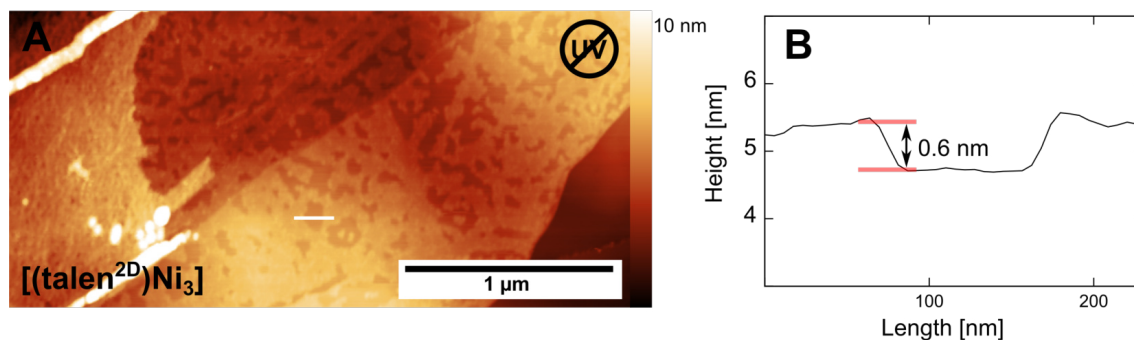
Figure 4.22: Preparation of a $[(talen^{2D})Ni_3]$ on HOPG transferred at lower surface pressure $(20\,mN\,m^{-1})$. (A) A film height of only $0.6\,nm$ was measured, which fits well in the model of a horizontally arranged planar molecule.

molecules. However, film thicknesses of $2.5\,nm$ were also found in the same sample. Thus, the results are indicating two different molecular configurations in the same monolayer. A reduction of the temperature to $4\,°C$ had no significant influence on the arrangement of the film and similar images were taken.

The coexistence of two different phases in a Langmuir film is often found during phase transitions[123, 260] and can result in two different molecular arrangements within the same Langmuir film.

UV Illumination

Though the transfer of Langmuir films is a promising way to cover surfaces with layers of single-molecule magnets, a necessary orientation of the molecules is hard to achieve. Intermolecular arrangements are only linked by weak forces, which makes the process of transfer to substrates difficult.[261]

The group of Prof. T. Glaser fabricated single-molecule magnets with anthracene units to create a covalently linked 2D-polymer. Similar molecules were reported to be strong enough to build up free-standing membranes over a hole.[262]

When irradiated with UV light $(360\text{–}370\,nm)$,[263] anthracene undergoes a photochemically dimerization to form dianthracene.[264] Illumination of a Langmuir film of $[(talen^{2D})Ni_3]$ forms a 2D-polymer with advanced mechanical properties.

Polymerization of $[(talen^{2D})Ni_3]$ was achieved at the air-water interface using a UV light source of $365\,nm$ (UVP 3UV, $8\,W$) at a distance of $11\,cm$. During the illumination of $30\,min$, the surface pressure $(50\,mN\,m^{-1})$ remained constant. Transfer of the monolayer was performed by the LS technique at a subphase temperature of $25.6\,°C$.

In Fig. 4.23, a fissure in the monolayer is shown and a line profile (inset) reveals a film

thickness of 3.5 nm. This is 1.0 nm bigger than an unpolymerized monolayer shown in Fig. 4.21. The results indicate that the polymerization of a highly compressed Langmuir film of [(talen^{2D})Ni$_3$] resulted in a 2D-polymer in which the molecules are arranged in a vertically orientated structure. This film was found to be of even higher thickness than a highly compressed film of monomeric [(talen^{2D})Ni$_3$].

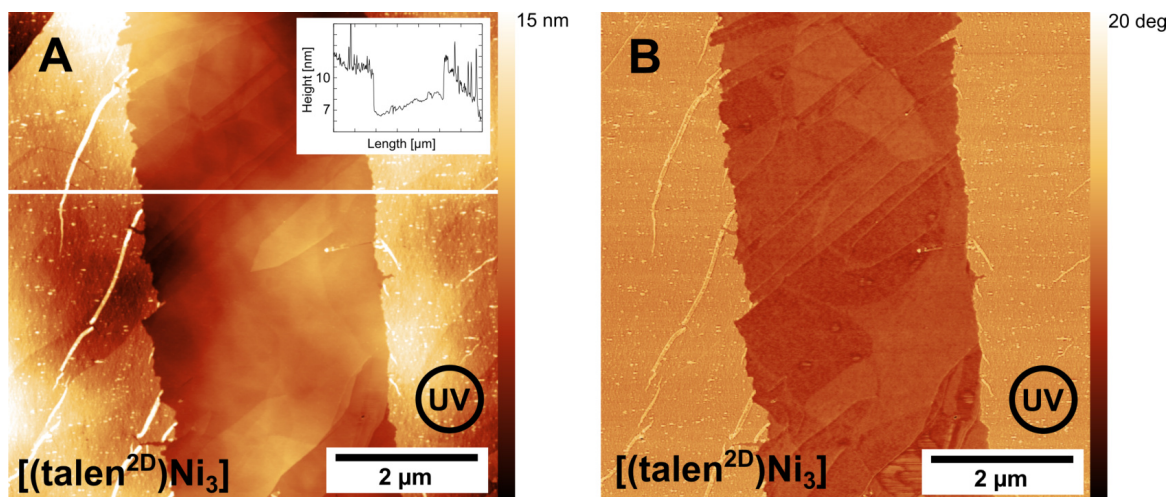Figure 4.23: Preparation of a polymerized [(talen^{2D})Ni$_3$] on HOPG. Surface pressure: (50 mN m^{-1}), 30 min illumination with 365 nm at the air-water interface, subphase temperature: 25.6 °C. (A) Close-up of a fissure in the monolayer exposing the HOPG surface underneath. The film exhibits a height of 3.5 nm. (B) The phase image verifies the bare HOPG under the adlayer by a distinct material contrast. This image was taken by M. Eickmann under the authors supervision.

Investigation by HIM

Finally, the potential of polymerized [(talen^{2D})Ni$_3$] as a free-standing membrane was investigated. A polymerized Langmuir film was transferred to a TEM grid (Quantifoil multi A) containing various aperture sizes to test the mechanical properties of the 2D-polymer of single-molecule magnets.

Inspected in the HIM (Fig. 4.24), the polymerized [(talen^{2D})Ni$_3$] monolayer was able to successfully suspend apertures up to $2 \times 8 \, \mu m^2$. Integrity of the film can be identified by the contrast to defects in the film.
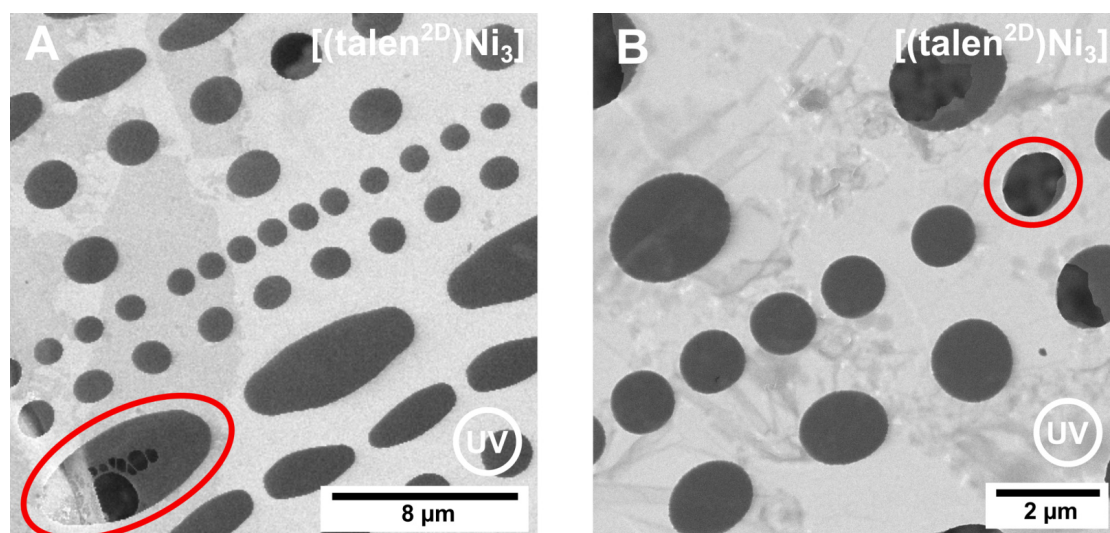
Figure 4.24: Polymerized free-standing monolayers of [(talen^{2D})Ni$_3$] suspended apertures of a Quantifoil TEM grid. (A) Contrast optimized image with almost complete coverage of the holes. (B) Several suspended apertures. The red circles highlight ruptured membranes.

Conclusion

Monolayers of single-molecule magnets, fabricated by the group of Prof. T. Glaser, were investigated at the air-water interface of a LB trough. They were then successfully transferred to samples and imaged by AFM and HIM. The AFM study indicated an upright, that is vertical, orientation of the triangular molecules at the air-water interface at height compression. A reduction of the temperature to 4 °C had no significant influence on the arrangement of the film. Transfer of polymerized [(talen^{2D})Ni$_3$] monolayers allowed free-standing membranes, inspected by HIM.

After the experiments of this thesis, Dr. J. Oldengott performed further studies on single-molecule magnets with several new developments. New mixtures of solvents for a better spreading behavior at the air-water interface of the LB trough were discussed. Modifications of the ligands in the [(talen^{2D})Ni$_3$] molecule lead to several improvements of the project.[257]

4.2 Lipid Painting Technique

So far, the conventional LB technique was used in this thesis to suspend small apertures on a TEM grid sample. However, the preparation is quite time consuming and immediate check of successful membrane formation requires considerably investigations.

Furthermore, electrophysiological experiments on membranes require an aqueous environment, whereas LB transfer protocols usually result in a sample that has been withdrawn from the aqueous phase in the final preparation step.

In this chapter, a microfluidic chip containing two reservoirs that are separated by a PTFE septum is used to form a planar lipid bilayer using the *painting method*.[38] There, a small amount of lipid solution is moved over a tiny aperture in the PTFE septum by an air-water interface to form a lipid membrane, which is why this technique is called painting method.
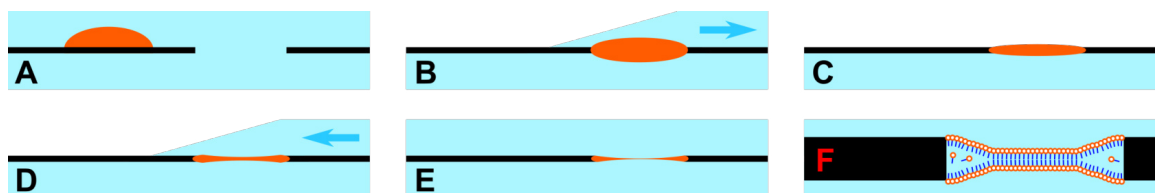

Figure 4.25: Schematic sketch of the bilayer formation procedure in the fluid chamber. (A) A droplet of lipid solution (orange) is applied onto the PTFE septum next to the aperture. (B) By removing the buffer solution from the upper reservoir, lipids slip into the aperture forming a plug. (C) The solvent (n-decane) is evaporating from the lipid plug. (D) Refilling the reservoire drags further solvent and lipids from the lipid plug. (E) Thinning process of the plug is proceeding. (F) The thinning process reaches a final state of forming a bilayer.

Planar lipid bilayers, which are also called black lipid membranes (BLMs), have been successfully used for electrophysiological analysis of membrane proteins,[265] including functional analysis of ion channels,[266] and DNA identification using nanopores.[267,268] Unlike supported lipid bilayers, which are attached to a surface, BLMs are free-standing and have excellent electric sealing properties that are capable of recording signals through single channel proteins by Coulter counter experiments.

4.2.1 Formation of Bilayer Lipid Membranes

A commercially available fluid chamber (Ionovation GmbH) was used for all experiments in this chapter. This fluid chamber was implemented into a home-built as well as into the commercial available setup (see chpt. 3.3.2 for details). Electrical measurements were made with Ag/AgCl electrodes connected to each side of the chamber by 3.5 M KCl agarose bridges. Data were acquired at frequencies of 10 kHz or greater and low pass filtered at 10 kHz. Optical examinations of planar membranes were performed

with a Zeiss Axiovert 200 microscope. The apparatus was either placed in a home-built Faraday cage or in the housing of the Ionovation Explorer to minimize electrical noise. The entire apparatus was placed on an isolation table (S-2000A, Newport).
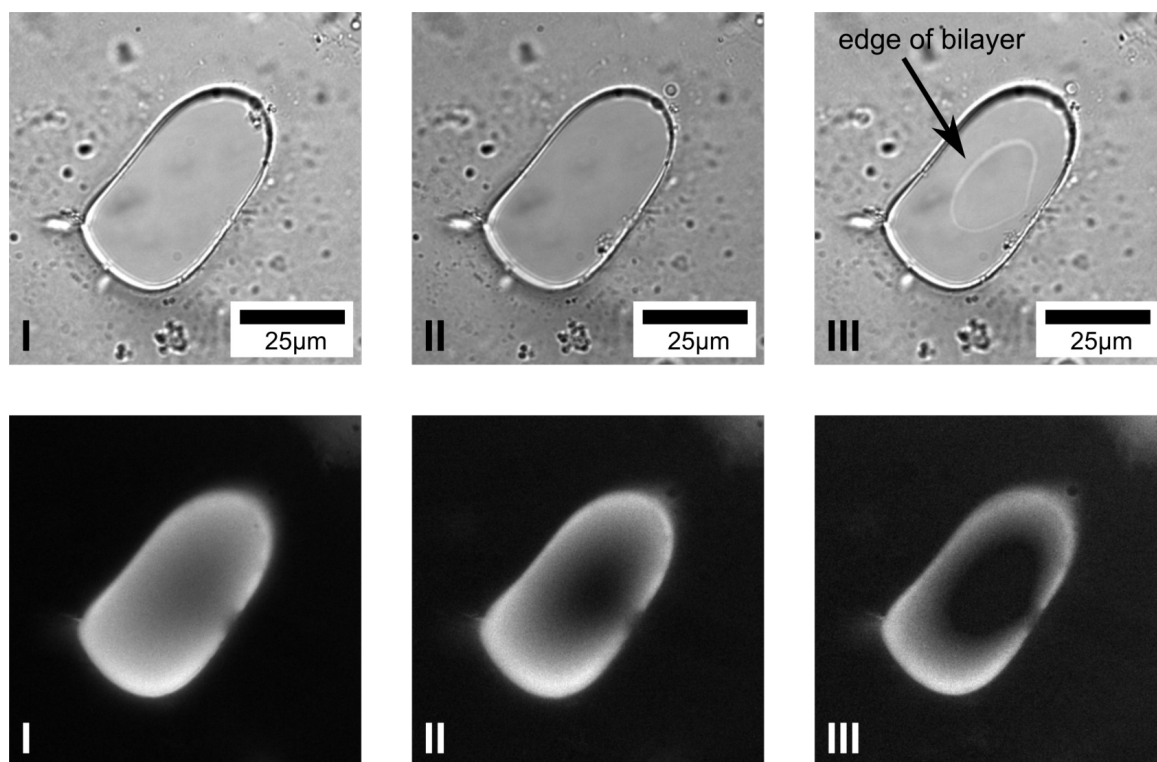

Figure 4.26: The thinning process of the lipids within the aperture can be monitored by fluorescence light, if marked with small amounts of Rhod-DOPE in the lipid solution. Images in top of each other (top: transmitting light, bottom: fluorescence light) were taken immediately after each other. (I) The aperture is filled with high amounts of lipid solution. (II) While the transmitting light image is unchanged, the center of the lipid area is starting to fade out in the fluorescence image. (III) The typical white ring, which is the edge of the bilayer, is visible in the transmitting light image. Almost no fluorescence light is detectable in the corresponding fluorescence image. Exposure time of the fluorescence images: 5 s.

The formation of a lipid bilayer in the fluid chamber is illustrated in Fig. 4.25. Lipids (DPhPC, PTPE, DiynePC) were dissolved in n-decane of $15\,\mathrm{mg\,ml^{-1}}$. Typically, 0.1–0.2 µl were added next to the micropore through the center hole in the microfluidic chamber, which was flushed and filled with electrolyte solution prior. The subsequent process of bilayer formation can also be observed by fluorescence light, if small amounts of Rhod-DOPE are applied to the lipid solution (Fig. 4.26).

Under optimal conditions, formation of a bilayer lipid membrane took only 30 s, start-

ing with the application of the lipid solution to the fluid chamber. This time scale is commonly described in literature.[269] Prepared bilayer were stable for several hours. Successful preparation depended on the use of freshly prepared lipids (preparation of a fresh solution on every Monday). The $15\,\mathrm{mg\,ml^{-1}}$ lipid solution should be stored in a brown glass bottle (single use) covered by aluminum foil at ambient conditions. Storage in the fridge is not recommended, because the humidity is high and water may dissolve into the lipid solution, which can result in damage of the lipids.

First experiments under the guidance of a predecessor were carried out with lipids that had expired for over 3 years and resulted in very limited success.
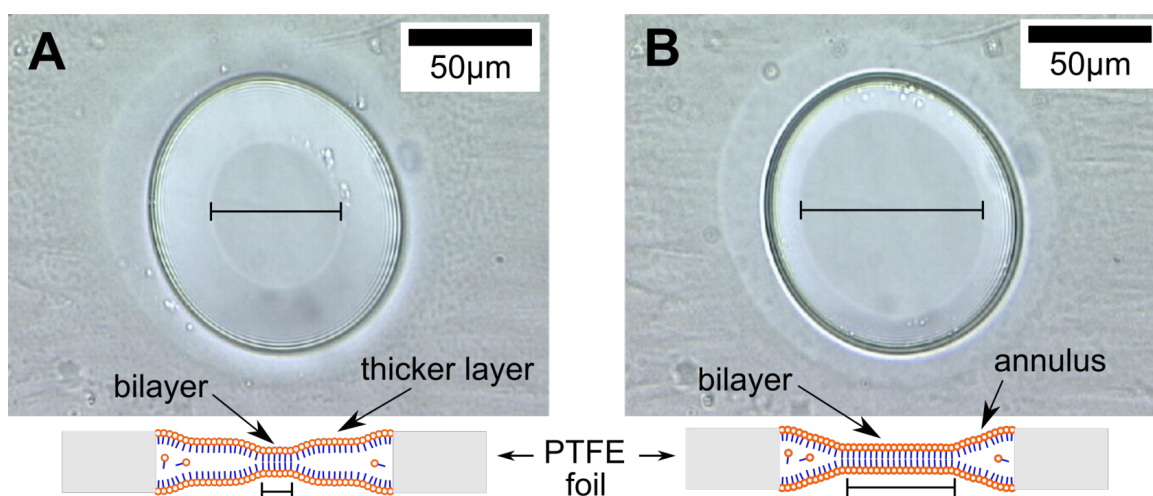

Figure 4.27: Formation of a lipid bilayer in the Ionovation fluid chamber. (A) After a pumping cycle, a bilayer has already formed in the center, which can clearly be identified by its surrounding white ring. (B) After a few seconds, the bilayer area has enlarged to a final state.

A lipid bilayer is shown in Fig. 4.27, which is surrounded and clearly defined by a white ring (annulus). This annulus is required to maintain stability by acting as a bridge between the lipid bilayer (5 nm) and the thick surrounding material, which is several micrometers thick and contains a mixture of solvent and lipids. It can be visually differentiated from the thin membrane.[270] The border of the two phases is also called *Plateau-Gibbs border*.[271] Since the annulus has an average thickness much greater than that of the bilayer, it is universally assumed that the electrical and permeability characteristics of the system are determined by the bilayer portion of the film. For instance, the electrical membrane capacitance is reciprocal proportional to the thickness of the membrane.

4.2.2 Capacitance of Lipid Bilayers

Since the thickness is the most characteristic parameter of a bilayer in contrast to the surrounding multilayer area, the successful formation of a lipid bilayer can be monitored by the capacitance.[272, 273] Specific electrical capacitance was measured using a Heka EPC-10 or a Hameg LCR Meter HM8018. There, an alternating ramp voltage was applied to the membrane and the resultant current was measured to determine the membrane capacitance. The membrane can be modeled as a parallel plate capacitor, with the capacitance given by:

$$C = \epsilon_0 \epsilon_r \cdot \frac{A}{d} \tag{4.2}$$

where ϵ_0 is the permittivity of free space $(8.854 \times 10^{-12} \, \mathrm{F \, m^{-1}})$, A is the membrane area, d is its thickness and ϵ_r is the dielectric constant of the hydrophobic chain region of the lipid membrane $(\epsilon_r = 2.1)$.[274, 275]

The membrane thickness can then be estimated based on the measured values and is 20–46 Å for the results of DPhPC in this work. Since the dielectric constant for lipids varies in the literature, calculations with higher values $(\epsilon_r = 3.0)$[269] lead to thicker membranes (29–66 Å). Experimental data of membrane thickness by X-ray is reported and show a thickness of DPhPC membranes of 47.7–48.5 Å.[276]
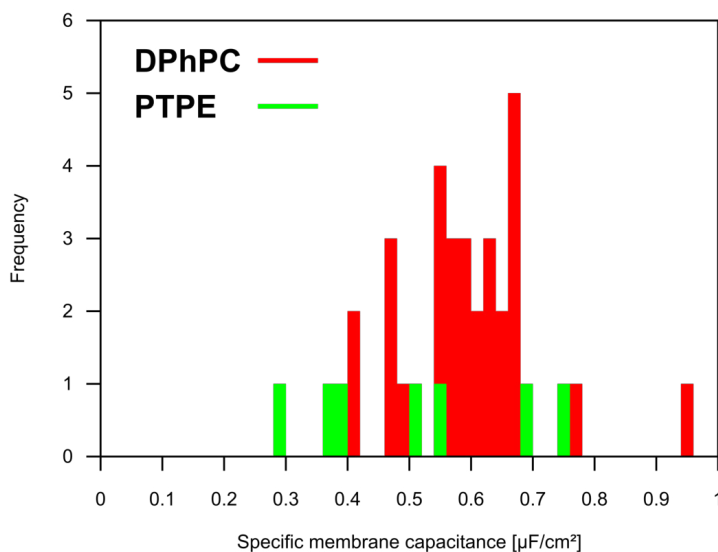

Figure 4.28: Specific membrane capacitance of DPhPC as well as PTPE bilayer. No significant difference were found between bilayers of PTPE and DPhPC.

The capacitance of more than 35 lipid bilayer was taken at laboratory conditions (20 °C) using a TRIS buffer (1 M KCL, 10 mM TRIS). Membrane area was calculated

from images and the specific membrane capacitance was then calculated. The results are shown in Fig. 4.28 and are in good agreement with literature.[277–279] No significant differences was found between bilayers of PTPE and DPhPC. The lipid membranes consistently have seal resistances of tens of GΩ and greater.

4.2.3 Incorporation of alpha-Hemolysin

Once a lipid bilayer has formed, $2\,\mu l$ of α-Hemolysin solution ($5\,\mu g\,ml^{-1}$, α-H soluted in deionized water) was added to the fluid chamber. A glass syringe was used to place the solution directly in top of the bilayer. Before application, solutions of α-Hemolysin must be treated by ultrasonic for $5\,s$ on low intensity, because of the tendency of α-H to exist in aqueous solution in the form of aggregates.[280]
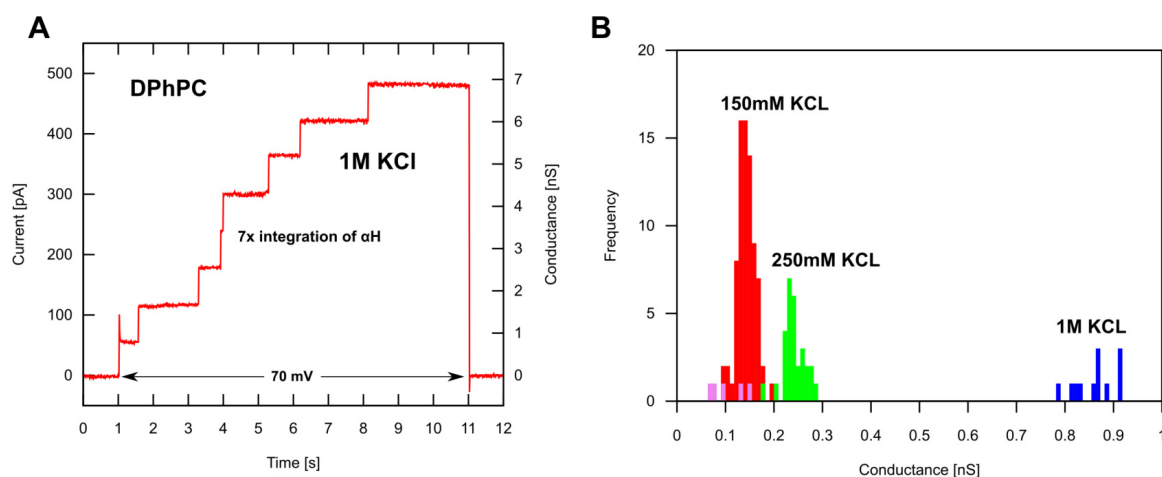

Figure 4.29: (A) Incorporation of seven α-H into a bilayer of DPhPC. The second y-axis illustrates the conductance. The very first step (and the overshoot) is caused by the voltage that was applied after the first second and cut off after 10 seconds. (B) The histogram shows conductances of α-H incorporated in DPhPC (red, green, blue) and PTPE (purple).

Shortly after application of α-H to the fluid chamber, steps in the current signal were observable. Each step is corresponding to an incorporation of an α-H molecule into the bilayer. Fig. 4.29A shows the incorporation of seven α-H molecules into a lipid bilayer of DPhPC using an electrolyte concentration of $1\,M$ KCL. The histogram of Fig. 4.29B demonstrates the dependency of the conductance on the electrolyte concentration, which is approximately linear in this regime.[281, 282] The experimental data is consistent with previous work.[269, 283]

4.2.4 Free Translocation of Oligonucleotide

After a lipid bilayer has formed in the fluid chamber and the application of α-H lead to the incorporation of a single transmembrane protein, the fluid cell was flushed extensively with fresh buffer solution to prevent further channel incorporation. For precise electrophysiological recordings, the metal ducts were raised and withdrawn from the fluid chamber during any measurement.
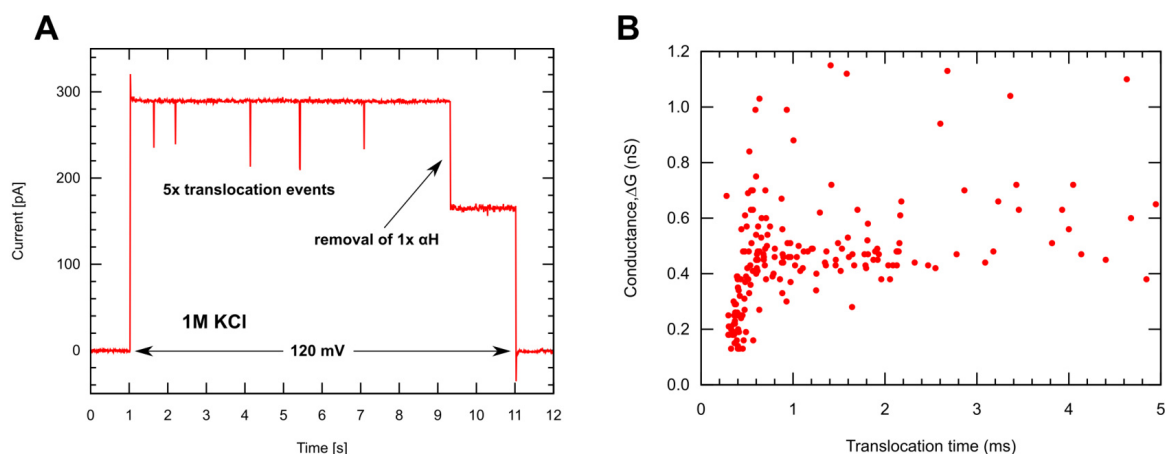

Figure 4.30: (A) Five translocation events of oligonucleotides through α-H are visible. (B) The Decreasing current signal (drop of 1 nS) indicates the removal of an α-H protein from the membrane during the measurement.

Oligonucleotides (5'-AGGTCGCCGCCCT-T-3', 'T-T' = 51 thymine) of 10 µM were used for translocation experiments. About 10 s after the DNA oligos were added, numerous short-lived current blockades occurred (Fig. 4.30A). The magnitude of the blockades varied and the current was reduced by 20–90 %. The blockades lasted from 400 µs to several thousand microseconds.

The distribution of translocation times as well as conductances is shown in the scatter plot of Fig. 4.30B. Each individual dot in the diagram represents a DNA translocation event. The data can be diveded into three classes: fast events that exhibit a low change of conductance can be interpreted as single, unfolded DNA molecules translocating through the α-H pore, short translocation events consisting of high drop of conductance, which are triggered most likely by DNA molecules that are folded in some way, and very fast events that populate the plot at the lower left corner of the plot. They exhibit a very low dwell times of around 0.4 ms and very small conductance drops. These events are assumed to be a result of DNA collisions with the pore or translocation of small DNA fragments. Further blockages of extreme long time were

most likely caused by polynucleotides that entered, but could not directly traverse the channel.[22] The shape of the plot fits very well into existing literature.[284, 285]

UV Illumination of DiynePC Bilayer

Final experiments using the Ionovation fluid chamber were taken to investigate the possibility of UV-induced polymerization of DiynePC bilayer membranes within an aqueous environment. Due to the thinning process during polymerization of membranes of diacetylene lipids, progressing polymerization should be detectable by monitoring the membrane capacitance. Subsequently, the possibility of α-H incorporation into the polymerized bilayer would have been investigated.

Formation of PTPE and DiynePC bilayers was successful using the same treatment procedure as for DPhPC membranes. Because the fluid chamber was filled with electrolyte solution, UV-illumination had to be applied through various layers of electrolyte. Thereto, the UV lamp was positioned as close as possible directly above the central opening of the fluid chamber. Because of the electric field of compartments within the UV lamp, electrophysiologically measurements could not be recorded at the same time without major disturbances of the electric signal.

Initial tests of polymerization of DiynePC bilayer membranes resulted in ruptured membranes after short time of illumination. Polymerization through water was then tested in a simplified experiment. There, several droplets of DiynePC solution were applied to the back side of quartz petri dishes (Fig. 4.31). These dishes were filled with: (i) deionized water, (ii) no filling (reference test), and (iii) degassed water saturated with argon. Since polymerization of DiynePC results in an intense red color (see Fig. 4.5), this setup tested the ability of UV light to penetrate the various settings. However, illumination trough deionized water that contains oxygen did not resulted in a red sample. Only the samples illuminated trough air and oxygenfree water showed an intense red color. Consequently, successful polymerization requires buffer solution that has to be depleted of oxygen by purging it with argon. This has already been reported for similar studies.[286]

Unfortunately, despite many illuminated DiynePC bilayer membranes, no indication of successful polymerization by capacitance recordings were taken. Some of the most promising measurements of illumination of DiynePC bilayers resulted in insignificant changes of the membrane capacitance, which should increase for approximately 20 % analogous to a reduction of the membrane thickness of 20 %.[69]

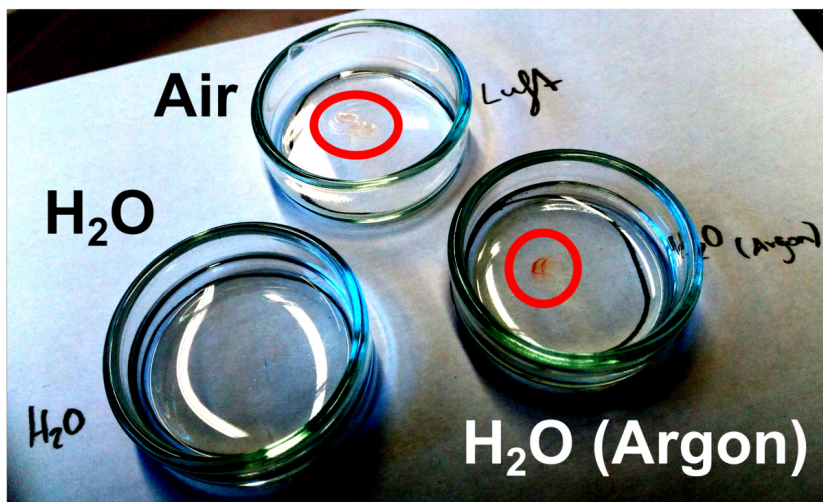It should be taken into account, that variations of the membrane capacitance can also

Figure 4.31: Droplets of DiynePC were applied to the back side of quartz glass dishes. The dishes were then filled with: deionized water (marked H_2O), no filling (marked air) and degassed water saturated with argon. Successful polymerization of DiynePC trough the dishes resulted in an intense red color (red circles) for the empty dish and the one that is filled with degassed water. The color has been optimized for better contrast.

be the result of a variation of the membrane area and can not exclusively be assigned to a process of membrane thinning, caused by the polymerization.

Membranes that were illuminated for 30 min by UV-light showed no indication of a higher mechanical stability.

Conclusion

The formation of lipid bilayer membranes from DPhPC and PTPE using a commercially available fluid chamber was successfully performed. For housing of the fluid chamber, a home-built experimental setup was established as well as (for a period of 14 days) a commercially setup was used (*Ionovation Explorer*). Lipid bilayer membranes were investigated electrophysiologically and specific membrane capacities were recorded in agreement with literature. No differences between DPhPC and PTPE could be detected. Conductance of α-Hemolysin that incorporated into the lipid bilayer was analyzed in dependence of the buffer concentration. Using α-Hemolysin, nanopore sensing experiments of free translocation of short DNA fragments were performed. The measured translocation statistics is consistent with prior work.

Initial experiments of UV-induced polymerization of lipid bilayers in aqueous environments were carried out, but were limited due to ruptured membranes during the UV-illumination. The usage of electrolyte solution free from oxygen has proved to be substantial for effective polymerization in aqueous environments.

4.3 TPT Carbon Nanomembranes

Until this point, all membranes described so far have been utilized for separation as well as a platform for transmembrane proteins. Membranes made of lipids are flexible due to their fluidity, especially in liquid environments, but fragile in general. By polymerization of membranes made of diacetylene lipids, the mechanical properties were increased. Solid-state membranes on the other hand come with superior mechanical stability and the advantage of chemical resistance.

The next chapter contains the results of a collaboration with the group of Prof. A. Gölzhäuser from the Supramolecular Systems and Surfaces of the Faculty of Physics of Bielefeld University. Recordings were performed together with Y. Yang. Membranes were fabricated from selfassembled carbon-rich molecules and crosslinked by electron illumination. In electrophysiological recordings, the permeation of various ions through carbon nanomembranes was investigated with respect to their potential application for water purification purposes.

4.3.1 Ion Permeance of CNMs

The ion conductance of 1,1',4',1"-terphenyl-4-thiol (TPT) carbon nanomembranes, henceforth simply referred to as *CNM*, was estimated by electrophysiological recordings across the membrane. Therto, the CNM was implemented to a transparent acrylic chamber (see chpt. 3.5). A current-voltage characteristic was then performed to determine the conductance. This was performed with various ion solutions of $1\,M$ concentration in milliQ water (NaCl, KCl, LiCl, $MgCl_2$ as well as HCl).

The fluid chamber was filled completely with the corresponding salt solution containing no other ions. The membranes were mounted to the fluid chamber in the subphase of a bowl, completely filled with salt solution. That way, no other ions are present at all. A concentration of $1\,M$ was chosen, because at low salt concentrations, low currents are even harder to detect. A higher salt concentration is hard to handle, because of crystallization on all involved surfaces due to evaporation of the salt solution.
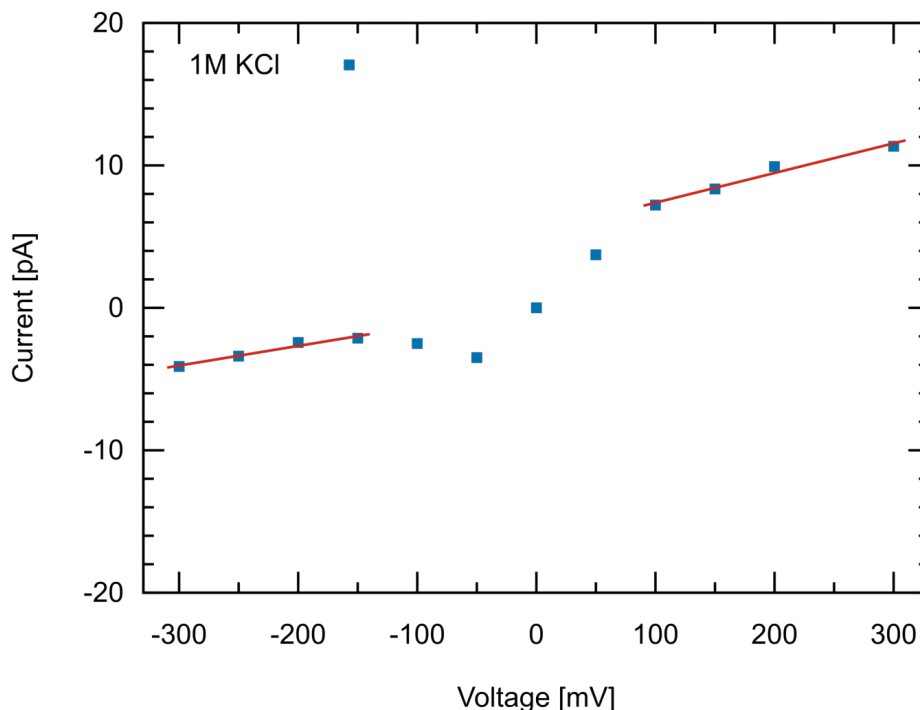
Figure 4.32: Current-voltage characteristic of a chip with a 200 nm thick Si_3N_4 membrane. The membrane contained no hole and no CNM was involved. Data points of positive voltage were recorded first. Because of surface charging processes,[287] first values of negative voltages are reduced. Linear fit of two sectors (red lines) exhibited electrical conductances of 13 pS and 20 pS, respectivly.

First, a current-voltage characteristic of a chip without any hole or CNM was taken (Fig. 4.32). This important test verified the impermeability of the bare chamber, its sealant and the Si_3N_4 chip. The membrane of the Si_3N_4 chip is 200 nm thick and not permeable for any ions or water. The result is the lowest limit of electric conductivity, that can be accomplished by this setup. All experimental data were recorded with Ag/AgCl electrodes and an Axopatch 200B patch clamp amplifier, if not stated other. The bessel filter of the Axopatch was set to 5 kHz, since high time resolution was not necessary for the experiments but low noise signal. The sample rate was 1 kHz for all measurements and the measurement period for each data point is of several seconds. Therefore, the *standard error of the mean* (SEM) for each data point is very small (0.5 pA) and has been included within the small squares in the graphics.

Besides all precautions and technical adaptations, a small amount of current is always passing through the chamber. The PDMS sealant, for instance, had to be perforated

for the four screws, and another hole is cut out for the Si_3N_4 chip to be placed. Along very small water channels, an electric current is feasible.

Next, a Si_3N_4 chip containing a $15\,\mu m$ hole in its membrane is measured to grant an estimation of an upper limit of the electric conductivity, that can be accomplished by this setup (Fig. 4.33). Similar Si_3N_4 chips are later used in all CNM experiments.
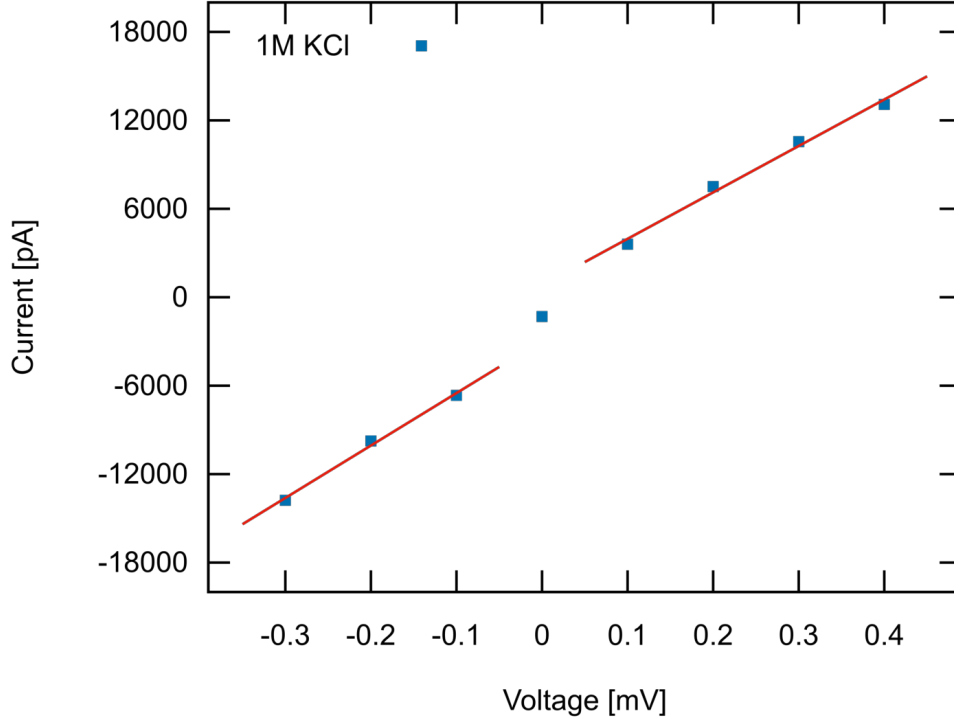

Figure 4.33: Current-voltage characteristic of a chip with a $200\,nm$ thick Si_3N_4 membrane. The membrane contained a $15\,\mu m$ hole and no CNM. Data points of positive voltage were recorded first. Linear fit of two sectors (red lines) exhibited electrical conductances of $3 \times 10^7\,pS$.

The electrical conductance of a single nano- or micropore in dependence of the specific conductivity of their aqueous environment can be calculated[288–290] by the following equation:

$$G = \sigma \left[\frac{4l}{\pi d^2} + \frac{1}{d} \right]^{-1} \tag{4.3}$$

Here, the bulk conductivity σ ($10.5\,S\,m^{-1}$ at $23\,°C$[281]) is the reciprocal of the bulk resistivity ρ, d is the diameter of the pore, and l is the thickness of the membrane. The first term in the bracket is representing the electric resistance of the channel itself, while the second term represents the access resistance of the pore. For larger pore

diameters (>15 nm), the access resistance becomes the dominant contribution.[288, 291] Further influences on the total resistance, like resistance of the electrodes or the wire connection are considered to be of insignificant impact, due to the high resistance of the total system.

A Si_3N_4 chip containing a 15 µm hole should exhibit a conductance of 15×10^7 pS (Eq. 4.3), which is in good agreement with the measurement (3×10^7 pS). It should be taken into account that the shape of the actual hole in the membrane is not completely spherical, as presumed in the theoretical model and therefore results in a lower electrical conductance.
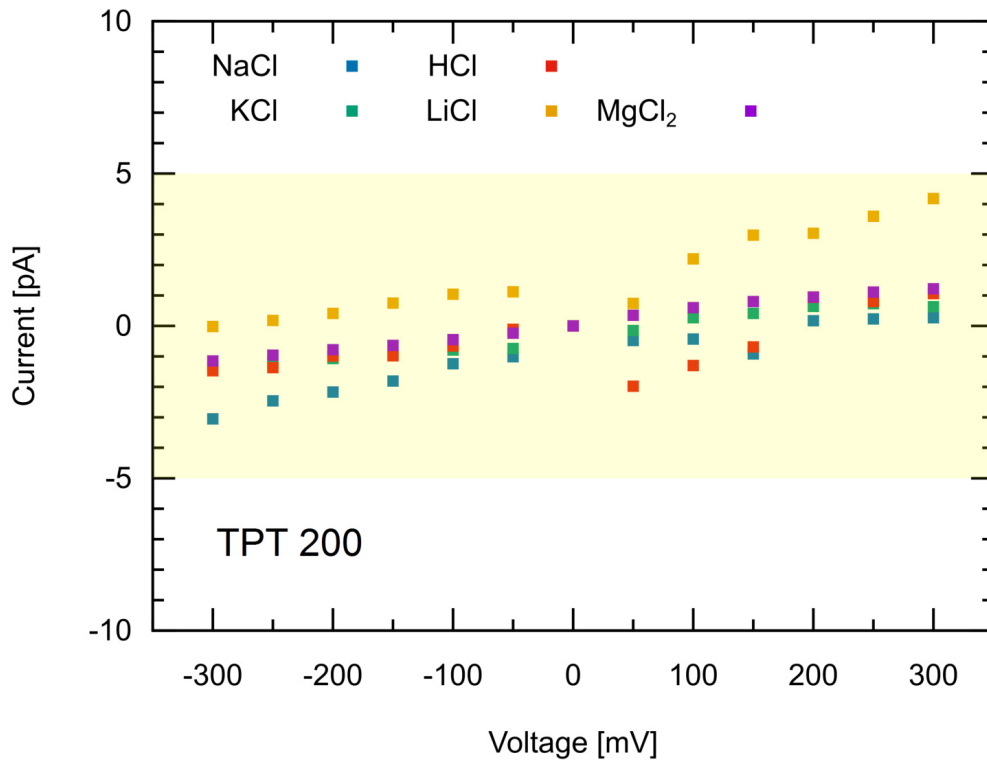

Figure 4.34: Current-voltage characteristic of a Si_3N_4 chip with a 200 nm thick membrane containing a 15 µm hole that is covered by a CNM. Data points of positive voltage were recorded first. The light yellow box represents an electrical conductance of 14.3 pS. The conductance recordings of all the used ion salt solutions are included in this range, and therefore of equal or smaller value. The electrical transmembrane resistance is higher than 70 GΩ. CNM sample *TPT200* was used for this data.

The ion permeability of CNMs was then tested in the same way as the bare Si_3N_4 chip was previously tested. Solutions of 1 M NaCl, KCl, LiCl, $MgCl_2$ and HCl were tested. Careful exchange of the salt solution between each series is necessary. This was

done using a syringe and a needle. Several iterations were performed to replace the remaining salt from the previous experiment. Maximum precautions are necessary to avoid damaging the CNM through this step. Air bubbles must be removed thoroughly afterwards, as they may seal the small channel of the acrylic chamber. If air bubbles would block parts of the membrane, this would lead to low or zero conductance, even with the use of a ruptured CNM.
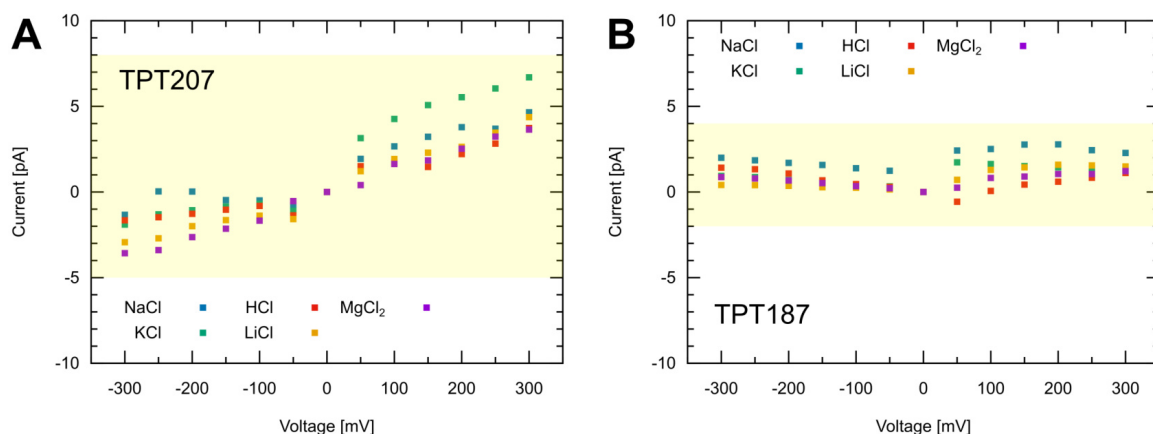

Figure 4.35: Current-voltage characteristics of Si_3N_4 chips with a 200 nm thick membrane containing a 15 µm hole that is covered by a CNM. Data points of positive voltage were recorded first. The light yellow box represents an electrical conductance, which acts as an upper limit for the conductance of all the used salt solutions. (A) The conductance of the yellow box is 18.6 pS. The charts of some measurements (e.g. NaCl) are not continuously positive in the range of negative voltages. This is due to charging effects, as positive voltages were recorded first.[287] (B) The conductance of the yellow box is 8.6 pS. In this diagram, the negative range of all five test series exhibits a negative slope, most likely caused by charging processes due to positive voltages.[287] For larger negative voltages, the effect begins to disappear due to disappearance of the charges. CNM samples *TPT207* and *TPT187* were used for this data.

By comparison of Fig. 4.32 on the one side, and Figs. 4.34, 4.35 and 4.36 on the other side, the electrical conductance of the CNM is of the same magnitude as for the Si_3N_4 chip with an intact membrane of 200 nm thickness and no hole. The remaining amount of conductance is due to the leakage of the acrylic chamber, which is not completely neglectable but of a very low value. Consequently, the utilized ions are not able to permeate the CNM. More precisely, a CNM is as permeable as a 200 nm thick membrane.
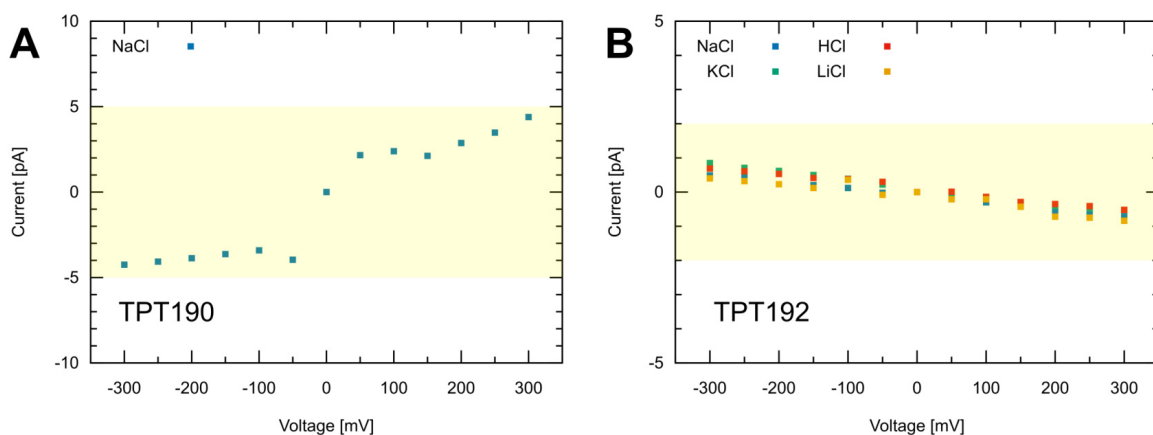
Figure 4.36: Current-voltage characteristics of Si_3N_4 chips with a 200 nm thick membrane containing a 15 μm hole that is covered by a CNM. Data points of positive voltage were recorded first. The light yellow box represents an electrical conductance, which acts as an upper limit for the conductance of all the used salt solutions. (A) The conductance of the yellow box is 14.3 pS. Because the CNM ruptured after the use of NaCl, this diagram only shows one chart of data. The noticeable behavior at small voltages disappeared for higher values and can be understood as a charge-related phenomenon.[287] (B) The conductance of the yellow box is 5.7 pS. The negative slope of the data in this chart is only explainable due to measurement uncertainty. Because the CNM ruptured after the use of LiCl, this diagram shows no chart of $MgCl_2$. CNM samples *TPT190* and *TPT192* were used for this data.

In some of the data presented in this chapter, the current-voltage characteristics exhibit a negative slope, which occurs predominantly in the negative voltage range. In most cases, this is due to charging processes caused by positive voltages that were investigated before the negative values.

The procedure to start with positive voltages from zero by increasing increments of 50 mV was chosen to obtain unsophisticated values unaffected by (smaller) previous ones. Starting with −300 mV and ascending values would have caused even more charging effects that would have affected all the following values.

It should be noted that similar experiments with nanopores of several nanometers in diameter using a 1 M salt solution would result in much higher currents and therefore are less affected by charging effects.[292]

The data in Fig. 4.36B shows a continuous negative slope in a current-voltage characteristic, which can only be explained by measurement uncertainty. However, the results support the assumption of an impermeable CNM with respect to ions.

4.3.2 Membrane Verification

The proof of the impermeableness of a CNM for various kinds of ions is linked to a different kind of proof: the experimental data that has been shown in the last chapter were indeed obtained by measuring a CNM rather than any other phenomena that simply blocked all the current in the current-voltage characteristics. Like for instances an air bubble or any other systematic error that simply has been overseen.

The most convincing verification would be a rupture of the CNM during any current-voltage characteristic. An electrical breakdown that happens during the experiment, and after that rupture, the intactness of the supporting Si_3N_4 membrane of $200\,nm$ thickness has to be assured as well.
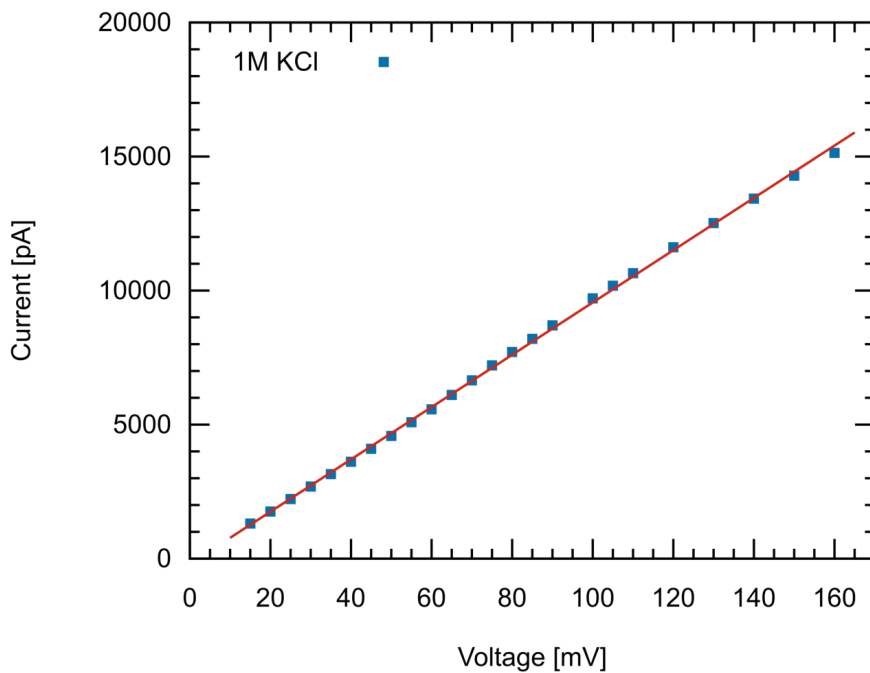

Figure 4.37: Current-voltage characteristic of a Si_3N_4 chip with a $200\,nm$ thick membrane containing a $15\,\mu m$ hole that is covered by a CNM. The electrical conductance is $10^5\,pS$ and very high in comparison to the prior results. CNM sample *TPT186* was used for this data.

In all the previous measurements, the conductance of an intact CNM was always below $20\,pS$. A value of $10^5\,pS$ in Fig. 4.37 indicates an anomaly. Calculated by equation 4.3, a total defect area of $\sim0.6\,\mu m^2$ in the CNM is feasible. Further recordings using increasing voltages lead to a continual increase of the current at $180\,mV$, which can be interpreted as a growing process of the defect in the CNM (Fig. 4.38).
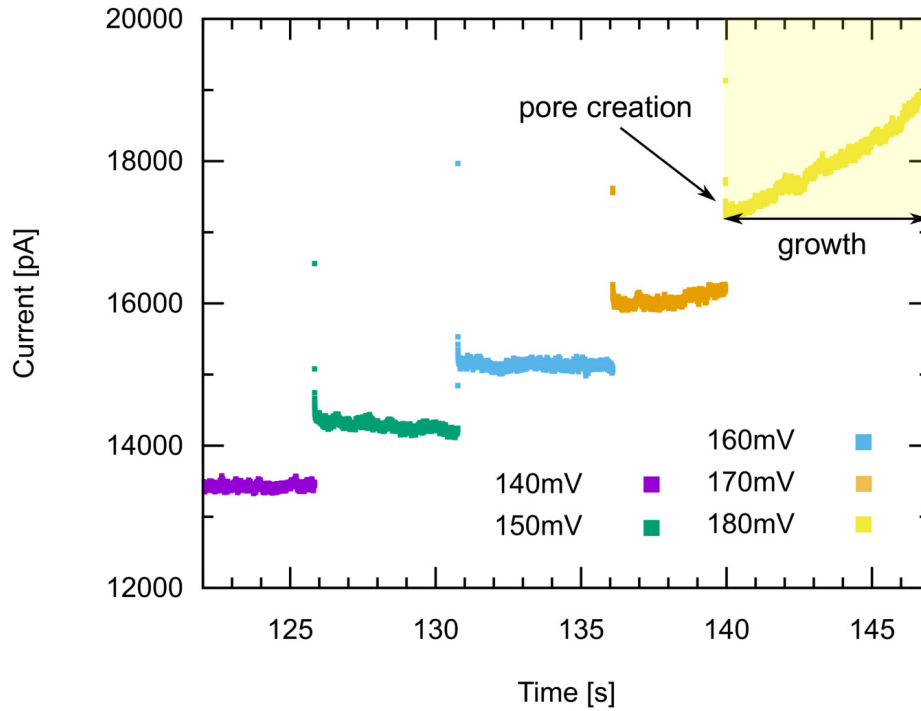
Figure 4.38: After the data from Fig. 4.37 had been recorded, an increasing current was detected starting at 180 mV (light yellow box). A growth of defective areas within the CNM is most likely. The upper limit of the measuring range was reached and prevented further investigation. CNM sample *TPT186* was used for this data.

Further investigation revealed that an intact CNM can withstand up to 50 V. Thereto, the electrodes were removed and replaced with simple metal wire electrodes to conduct a voltage from a voltage source supplying up to 50 V DC. All voltages were supplied for at least 120 s. After each applied voltage, the CNM was found to be intact by measuring the electrical conductance.

After no electrical breakthrough could be achieved, the complete fluid chamber was submerged in a ultrasonic bath for 5 s at the lowest possible power parameter. A subsequent electrical test revealed that the CNM had been destroyed. However, an investigation in a light microscope revealed an intact Si_3N_4 membrane. No air bubbles were found to be present at any step during the treatment.

Finally, the findings of this chapter highly suggest that all the data collected from the ion permeation measurements were indeed obtained by examining a CNM. Due to a clear vision on the chip at any moment during the investigation, a blocking air bubble could be excluded to be the reason for the low conductance.

4.3.3 Forward Osmosis

The permeation of water molecules, as well as helium through a CNM has been demonstrated by Y. Yang in a recent publication.[33] The structure of CNMs were investigated with high resolution AFM and obtained small pores of subnanometers in diameter. Vapor permeation tests using acetonitrile, ethanol, n-hexane, 2-propanol as well as permeation of Ne, Ar, CO_2, N_2 and O_2 were found to be negative.
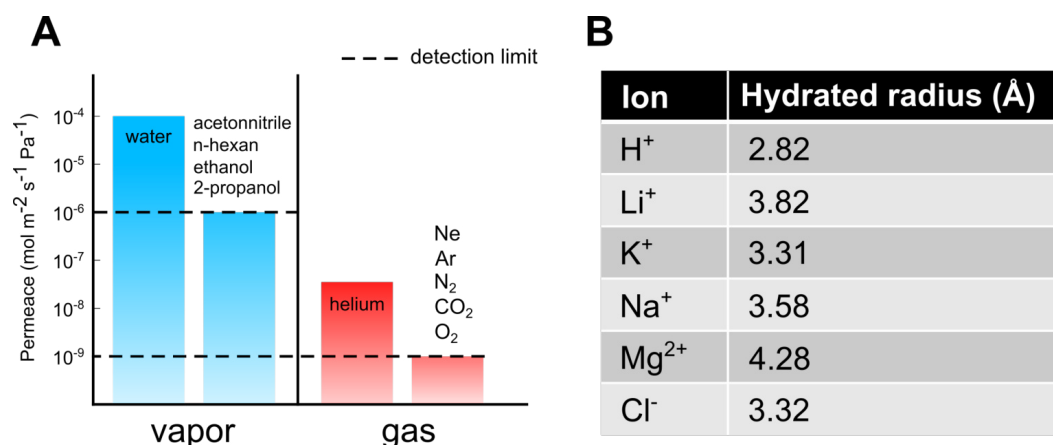

Figure 4.39: (A) Permeances of vapors and gases of TPT CNMs. The dashed lines indicate the respective detection limits of the measurements. The detection limit of vapor permeation measurements is related to the sensitivity of the balance and the duration of the experiment. The detection limit of gas permeation measurements depends on the instrumental background noise of the mass spectrometer.[33, 293] (B) Hydrated radius of various ions. Inspired by a Figure in *Yang et al.*[33]

These results indicate that CNMs contain sub-nanometer sized channels that are permeable for water molecules and helium, but are impermeable for a number of tested molecules (Fig. 4.39A). The data indicate that a CNM acts like a molecular sieve, which only allows the passing of molecules below a certain size.

Results of the present thesis indicates that ions of Na^+, K^+, Li^+, Mg^{2+} as well as H^+ (Fig. 4.39B) are not capable of passing the CNM.

The possibility of desalination is feasible and a very promising application. Additionally, the fabrication process of CNMs is scalable[39] and versatile, allowing membranes with macroscopic dimensions for high throughput applications.

The following, preliminary experimental data provide a perspective of how osmosis and water purification could be investigated using CNMs.

For the osmosis experiments, the same experimental setup was used, which was already

used for the ion permeation experiments. With one exception: Two holes were put on each side to the acrylic chamber. That way, each side of the mounted CNM is accessible by two electrodes at the same time. By this setup, which is illustrated in Fig. 4.40, the electrical conductance of the salt solution between the electrodes can be monitored over time.
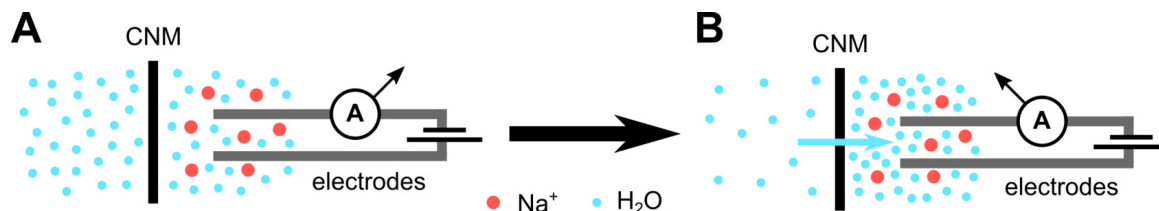

Figure 4.40: In the osmosis setup, both electrodes are attached to the reservoir containing salt water. (A) A high current is detected, due to the high concentration of ions. (B) After some time passed, water molecules had permeated the CNM due to the osmotic pressure. As the salt concentration decreased, the current decreased.

After filling the complete permeation cell with Milli-Q water, one side was carefully exchanged by a 1 M NaCl salt solution. To that side, a pair of Ag/AgCl electrodes was immersed. By the osmotic pressure, water molecules should be passing through the CNM to compensate the difference of concentrations. The osmotic pressure can be calculated by the following equation:

$$\Pi = i \cdot c \cdot R \cdot T \tag{4.4}$$

Here, i is the *van 't Hoff factor*, which is an empirical correction factor of 1.9,[294] c is the concentration of the salt solution, R is the gas constant, and T is the temperature. The osmotic pressure is about 48 bar, for a concentration of 1 M NaCl salt solution versus Milli-Q water. A difference in ionic concentration between both sides should be compensated by the flow of water through the membrane. This leads to a corresponding increase in volume on the side with the high concentration. The permeation of water ends as soon as the osmotic pressure on one side of the membrane corresponds with the hydrostatic pressure of the other side of the membrane.

The first measurement of the electrical conductance took place initially after the electrodes had been immersed to the 1 M NaCl solution in the acrylic chamber. The electrodes remained attached for the next 120 min while the electric conductance was collected in increments of 30 min.

Evaporation of water from the 1 M NaCl solution must be considered during the measurement at ambient conditions, because the deliquescence humidity of NaCl is about 75 % at room temperature.[295] An estimated amount of 4 µl of H_2O evaporated during the 120 min of the experiments.[296] This is based on a remaining $0.25\,cm^2$ water surface (the glass tubes of the electrodes blocked most of the original area). The fluid chamber was filled with a total of approximately 200 µl, distributed to both sides. Therefore, the evaporation raised the concentration of the salt solution by ca. 4 %, which led to a higher electrical conductance. Due to an almost linear correlation of concentration and conductivity in this region,[281, 282] the conductance is expected to be about 4 % higher at the end of the experiments.
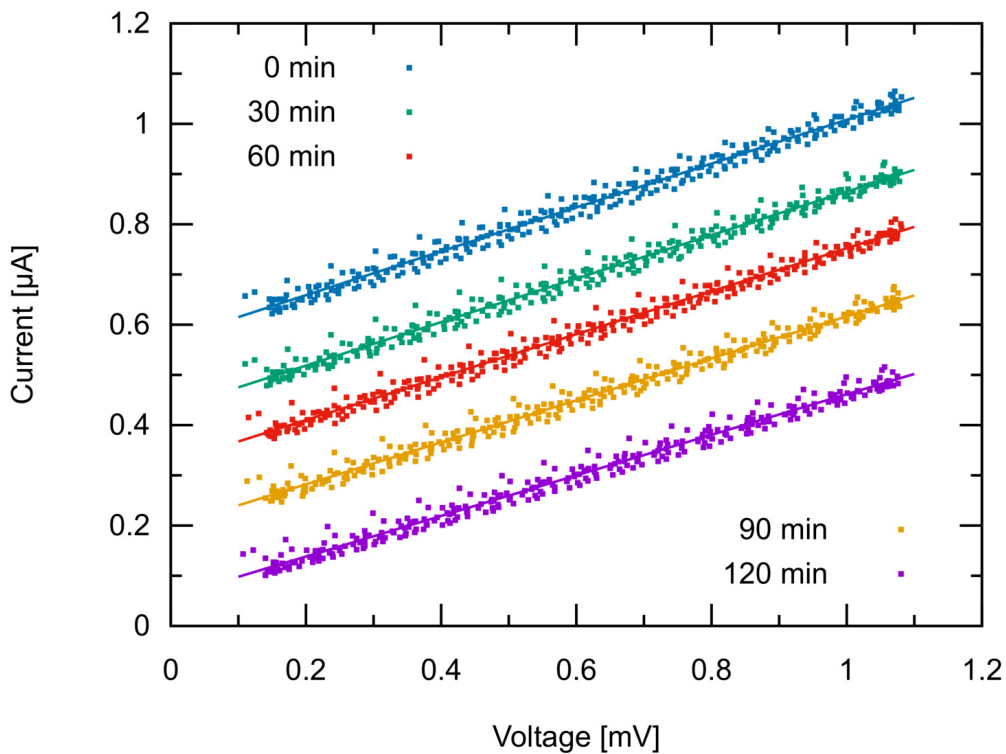
Figure 4.41: Current-voltage characteristic was taken in a short circuit manner of a 1 M NaCl in a fluid chamber. In the same chamber, an amount of Milli-Q water is separated by a Si_3N_4 chip with a 200 nm thick membrane containing a 11 µm hole that is covered by a CNM (see Fig. 4.40). Data points were collected using a *Reference 600 Potentiostat*. For a better overview, each pack of data is shifted to higher currents, and only 10 % of the points are shown but all are used in the regression calculation. The conductance decreased constantly from $436.6 \pm 0.9\,mS$ to $404.0 \pm 0.9\,mS$ (120 min). CNM sample *TPT325* was used for this data.

The recorded electrical conductance decreased constantly in the experiment, starting at $436.6 \pm 0.9\,\text{mS}$, $433.1 \pm 0.9\,\text{mS}$ (30 min), $427.6 \pm 0.8\,\text{mS}$ (60 min), $418.1 \pm 0.8\,\text{mS}$ (90 min), and $404.0 \pm 0.9\,\text{mS}$ (120 min). This is a reduction of 7.5 % and should therefore also result in a 7.5 % reduction in saline concentration to a new concentration of 0.925 M NaCl. Based on a 100 µl reservoir in the fluid chamber, an amount of 8.1 µl had to permeate through the membrane, to create that drop of concentration. This can be calculated with any form of dilution equation. Additional 4 µl permeated through the CNM, but evaporated during the investigation, which results in a total amount of permeated water of 12 µl. However, the permeance of water through a CNM can be calculated[33] by the following equation:

$$P \approx 1.1 \times 10^{-4}\,\text{mol}\,\text{m}^{-2}\,\text{s}^{-1}\,\text{Pa}^{-1} \tag{4.5}$$

Under the assumption of an 11 µm circular hole, coverted by a CNM, an osmotic pressure of 48 bar, and a lapse of time of 120 min, the water permeation is 26 µl, which is within the same order of magnitude as the experimental results.

Conclusion

Ion permeation through CNMs was investigated by electrophysiological recordings. Current-voltage characteristics revealed that Na^+, K^+, Li^+, Mg_2^+ and H^+ were not capable of passing the CNM, though more precisely: a CNM is as permeable for those ions as a 200 nm membrane of Si_3N_4.

A CNM was successfully tested to withstand a voltage of 50 V, but was very fragile to ultrasonic treatment. The growth of defective areas was monitored during electrophysiological recordings.

Finally, initial experiments for water desalination in a forward osmotic setup were performed with promising results, but have to be reproduced to verify the results.

5 Summary

The present thesis described different approaches for fabrication, characterization as well as application of membranes exhibiting only a few molecules in thickness. These nanomembranes were prepared in a free-standing as well in a supported manner.

Infrared spectroscopy of substrate supported UV-polymerizable phospholipid adlayers were performed in a collaboration with Dr. T. Kottke from the Physical and Biophysical Chemistry, Bielefeld University. The nature of the kinetics and chemistry of the polymerization was monitored and clarified using an attenuated total reflection setup. The study revealed a distinct reduction in the number of the diacetylene groups in the phospholipids during the polymerization process. Additional UV-VIS measurements confirmed the accepted theory of conjugated systems that were formed during the polymerization. Large π-systems arise, which are known for their absorption in the ultraviolet region causing the red color of the samples.

Inspected in the AFM, substrate supported membranes of UV-polymerizable phospholipids showed distinct patterns on HOPG. In domains that exhibited different orientation angles of 60° or 120° between them, the threefold symmetry of the HOPG lattice was displayed. These structures turned to be inhibited for polymerized layers showing no alignment to the underlying crystalline structure of the HOPG.

Free-standing membranes of polymerized membranes were then investigated with HIM, using a TEM grid as a supporting material. Successful formation of robust pore-spanning monolayers up to $8 \times 2\,\mu m^2$ could be verified for UV-polymerized PTPE and DiynePC. Subsequently inspected in the AFM, the membranes were found to remain intact for several hours under laboratory conditions. It was found that the mechanical properties of polymerized lipid membranes were attributed to the amount of diacetylene groups per molecule, which is in agreement with the IR spectroscopy.

Single-molecule magnets of $[(talen^{2D})Ni_3]$ were studied in a collaboration with the group of Prof. T. Glaser from the Inorganic Chemistry in the Chemistry Department at Bielefeld University. Fabricated by Dr. J. Oldengott, monolayers of triangular single-molecule magnets were investigated at the air-water interface of a LB trough,

successfully transferred to samples, and imaged by AFM and HIM. The AFM study revealed an upright, that is vertically, orientation of the triangular molecules at the air-water interface at height compression. Finally, polymerization of a monolayer resulted in free-standing membranes, inspected by HIM.

Besides the LB trough, lipid membranes were also fabricated in a fluid chamber using the Montal-Mueller method. In the aqueous environment, lipid bilayers were easy to generate and electrophysiological recordings were taken. The lipid bilayer membranes were made from conventional as well as polymerizable lipids. The specific membrane capacitance was determined in good agreement of the literature. Conductance of α-Hemolysin that incorporated into the lipid bilayer was analyzed in dependence of the buffer concentration. Using α-Hemolysin, nanopore sensing experiments of free translocation of short DNA fragments were performed. The measured translocation statistics is consistent with prior work. Initial experiments of UV-induced polymerization of lipid bilayers in aqueous environments were carried out, but were limited due to ruptured membranes during the UV-illumination. The usage of electrolyte solution free from oxygen has proved to be substantial for effective polymerization in aqueous environments.

The last experimental section originated from a collaboration with the group of Prof. A. Gölzhäuser, Supramolecular Systems and Surfaces, Faculty of Physics of Bielefeld University. Membranes were fabricated from a selfassembled carbon-rich material that was polymerized by electron illumination. These CNMs were tested on their permeability of various ions. Electrophysiological recordings revealed that Na^+, K^+, Li^+, Mg^{2+} as well as H^+ were not capable of passing the CNM. The membranes were successfully tested to withstand a voltage of $50\,V$, but were very fragile to ultrasonic treatment. The growth of defective areas was monitored during electrophysiological recordings. Preliminary experiments on an osmosis setup indicated the suitability for water purification applications, but have to be reproduced to verify the results.

Bibliography

[1] B. Alberts. *Molecular biology of the cell*. Garland Science, New York, NY, 4th edition, 2002.

[2] M. Meyerson, S. Gabriel, and G. Getz. Advances in understanding cancer genomes through second-generation sequencing. *Nature reviews. Genetics*, 11(10):685–696, 2010.

[3] H. Rehm. Disease-targeted sequencing: a cornerstone in the clinic. *Nature reviews. Genetics*, 14(4):295–300, 2013.

[4] K. Moriyoshi, M. Masu, T. Ishii, R. Shigemoto, N. Mizuno, and S. Nakanishi. Molecular cloning and characterization of the rat nmda receptor. *Nature*, 354(6348):31–37, 1991.

[5] A. Khan, R. Wang, W. Cao, D. Doerge, D. Wennerstrom, and C. Cerniglia. Molecular cloning, nucleotide sequence, and expression of genes encoding a polycyclic aromatic ring dioxygenase from mycobacterium sp. strain pyr-1. *Applied and environmental microbiology*, 67(8):3577–3585, 2001.

[6] M. Jobling and P. Gill. Encoded evidence: Dna in forensic analysis. *Nature reviews. Genetics*, 5(10):739–751, 2004.

[7] J. Bienvenue, N. Duncalf, D. Marchiarullo, J. Ferrance, and J. Landers. Microchip-based cell lysis and dna extraction from sperm cells for application to forensic analysis. *Journal of forensic sciences*, 51(2):266–273, 2006.

[8] P. Hebert, A. Cywinska, S. Ball, and J. deWaard. Biological identifications through dna barcodes. *Proceedings. Biological sciences*, 270(1512):313–321, 2003.

[9] M. Blaxter. Molecular systematics: Counting angels with dna. *Nature*, 421(6919):122–124, 2003.

Bibliography

[10] F. Sanger and A. Coulson. A rapid method for determining sequences in dna by primed synthesis with dna polymerase. *Journal of Molecular Biology*, 94(3):441–448, 1975.

[11] Y. Feng, Y. Zhang, C. Ying, D. Wang, and C. Du. Nanopore-based fourth-generation dna sequencing technology. *Genomics, proteomics & bioinformatics*, 13(1):4–16, 2015.

[12] S. Howorka and Z. Siwy. Nanopore analytics: sensing of single molecules. *Chemical Society reviews*, 38(8):2360–2384, 2009.

[13] I. Makra and R. Gyurcsányi. Electrochemical sensing with nanopores: A mini review. *Electrochemistry Communications*, 43:55–59, 2014.

[14] W. Shi, A. Friedman, and L. Baker. Nanopore sensing. *Analytical chemistry*, 89(1):157–188, 2017.

[15] Y. Kim, J. Min, I. Lee, S. Kim, A. Kim, K. Kim, K. Namkoong, and C. Ko. Nanopore sensor for fast label-free detection of short double-stranded dnas. *Biosensors & bioelectronics*, 22(12):2926–2931, 2007.

[16] The long view on sequencing. *Nature biotechnology*, 36(4):287, 2018.

[17] W. Ansorge, T. Katsila, and G. Patrinos. Perspectives for future dna sequencing techniques and applications. In *Molecular Diagnostics*, pages 141–153. Elsevier, 2017.

[18] J. Nivala, D. Marks, and M. Akeson. Unfoldase-mediated protein translocation through an alpha-hemolysin nanopore. *Nature biotechnology*, 31(3):247–250, 2013.

[19] L. Restrepo-Pérez, C. Joo, and C. Dekker. Paving the way to single-molecule protein sequencing. *Nature nanotechnology*, 13(9):786–796, 2018.

[20] J. Wilson, L. Sloman, Z. He, and A. Aksimentiev. Graphene nanopores for protein sequencing. *Advanced functional materials*, 26(27):4830–4838, 2016.

[21] W. Coulter. Means for counting particles suspended in a fluid, 1953. US Patent 2,656,508.

120

[22] J. Kasianowicz, E. Brandin, D. Branton, and D. Deamer. Characterization of individual polynucleotide molecules using a membrane channel. *Quarterly reviews of biophysics*, 93(24):13770–13773, 1996.

[23] D. Deamer, M. Akeson, and D. Branton. Three decades of nanopore sequencing. *Nature biotechnology*, 34(5):518–524, 2016.

[24] A. Storm, J. Chen, X. Ling, H. Zandbergen, and C. Dekker. Fabrication of solid-state nanopores with single-nanometre precision. *Nature materials*, 2(8):537–540, 2003.

[25] G. Schneider, S. Kowalczyk, V. Calado, G. Pandraud, H. Zandbergen, L. Vander-sypen, and C. Dekker. DNA translocation through graphene nanopores. *Nano letters*, 10(8):3163–3167, 2010.

[26] K. Liu, J. Feng, A. Kis, and A. Radenovic. Atomically thin molybdenum disulfide nanopores with high sensitivity for DNA translocation. *ACS nano*, 8(3):2504–2511, 2014.

[27] S. Liu, B. Lu, Q. Zhao, J. Li, T. Gao, Y. Chen, Y. Zhang, Z. Liu, Z. Fan, F. Yang, L. You, and D. Yu. Boron nitride nanopores: highly sensitive DNA single-molecule detectors. *Advanced materials (Deerfield Beach, Fla.)*, 25(33):4549–4554, 2013.

[28] F. Sawafta, A. Carlsen, and A. Hall. Membrane thickness dependence of nanopore formation with a focused helium ion beam. *Sensors (Basel, Switzerland)*, 14(5):8150–8161, 2014.

[29] J. Li, D. Stein, C. McMullan, D. Branton, M. Aziz, and J. Golovchenko. Ion-beam sculpting at nanometre length scales. *Nature*, 412(6843):166–169, 2001.

[30] D. Nath. Membrane biology. *Nature*, 438(7068):577, 2005.

[31] J. Werber, C. Osuji, and M. Elimelech. Materials for next-generation desalination and water purification membranes. *Nature Reviews Materials*, 1(5):41683, 2016.

[32] R. Nair, H. Wu, P. Jayaram, I. Grigorieva, and A. Geim. Unimpeded permeation of water through helium-leak-tight graphene-based membranes. *Science (New York, N.Y.)*, 335(6067):442–444, 2012.

Bibliography

[33] Y. Yang, P. Dementyev, N. Biere, D. Emmrich, P. Stohmann, R. Korzetz, X. Zhang, A. Beyer, S. Koch, D. Anselmetti, and A. Gölzhäuser. Rapid water permeation through carbon nanomembranes with sub-nanometer channels. *ACS nano*, 12(5):4695–4701, 2018.

[34] A. Mohammad, Y. Teow, W. Ang, Y. Chung, D. Oatley-Radcliffe, and N. Hilal. Nanofiltration membranes review: Recent advances and future prospects. *Desalination*, 356:226–254, 2015.

[35] P. Eriksson. Nanofiltration extends the range of membrane filtration. *Environmental Progress*, 7(1):58–62, 1988.

[36] R. Hillmann, M. Viefhues, L. Goett-Zink, D. Gilzer, T. Hellweg, A. Gölzhäuser, T. Kottke, and D. Anselmetti. Characterization of robust and free-standing 2d-nanomembranes of uv-polymerized diacetylene lipids. *Langmuir*, 34(10):3256–3263, 2018.

[37] P. Mueller, D. Rudin, H. Ti Tien, and W. Wescott. Reconstitution of cell membrane structure in vitro and its transformation into an excitable system. *Nature*, 194(4832):979–980, 1962.

[38] M. Montal and P. Mueller. Formation of bimolecular membranes from lipid monolayers and a study of their electrical properties. *Proceedings of the National Academy of Sciences of the United States of America*, 69(12):3561–3566, 1972.

[39] A. Turchanin, D. Weber, M. Büenfeld, C. Kisielowski, M. Fistul, K. Efetov, T. Weimann, R. Stosch, J. Mayer, and A. Gölzhäuser. Conversion of self-assembled monolayers into nanocrystalline graphene: structure and electric transport. *ACS nano*, 5(5):3896–3904, 2011.

[40] P. Russell. *iGenetics*. B. Cummings, San Francisco, 2002.

[41] G. Mednel. Versuche über pflanzen-hybriden. *Verhandlungen des Naturforschenden Vereines Brünn*, 4:3–47, 1866.

[42] L. Cong, A. Ran, D. Cox, S. Lin, R. Barretto, N. Habib, P. Hsu, X. Wu, W. Jiang, L. Marraffini, and F. Zhang. Multiplex genome engineering using CRISPR/Cas systems. *Science (New York, N.Y.)*, 339(6121):819–823, 2013.

[43] E. Mardis. A decade's perspective on DNA sequencing technology. *Nature*, 470(7333):198–203, 2011.

[44] D. Han, S. Pal, J. Nangreave, Z. Deng, Y. Liu, and H. Yan. DNA origami with complex curvatures in three-dimensional space. *Science (New York, N.Y.)*, 332(6027):342–346, 2011.

[45] N. Goldman, P. Bertone, S. Chen, C. Dessimoz, E. LeProust, B. Sipos, and E. Birney. Towards practical, high-capacity, low-maintenance information storage in synthesized DNA. *Nature*, 494(7435):77–80, 2013.

[46] R. Dahm. Discovering DNA: Friedrich Miescher and the early years of nucleic acid research. *Human genetics*, 122(6):565–581, 2008.

[47] J. Watson and F. Crick. Molecular structure of nucleic acids: a structure for deoxyribose nucleic acid. *Nature*, 171(4356):737–738, 1953.

[48] H. Lodish. *Molecular cell biology*. W. Freeman, New York, 6th edition, 2008.

[49] http://ib.bioninja.com.au/standard-level/topic-2-molecular-biology/26-structure-of-dna-and-rna/dna-structure.html, 04.10.2018.

[50] J. Watson and A. Berry. *DNA: The secret of life*. Borzoi book. Knopf, New York, 1st edition, 2003.

[51] E. Kool. Hydrogen bonding, base stacking, and steric effects in DNA replication. *Annual review of biophysics and biomolecular structure*, 30:1–22, 2001.

[52] M. Mandelkern, J. Elias, D. Eden, and D. Crothers. The dimensions of DNA in solution. *Journal of Molecular Biology*, 152(1):153–161, 1981.

[53] C. Calladine. *Understanding DNA: The Molecule and How it Works*. Elsevier professional, 3rd edition, 2004.

[54] J. Krebs, E. Goldstein, and S. Kilpatrick. *Lewin's essential genes*. Jones and Bartlett Publ, Burlington, MA, 3rd edition, 2013.

[55] M. Shamsi and H. Kraatz. Interactions of metal ions with DNA and some applications. *Journal of Inorganic and Organometallic Polymers and Materials*, 23(1):4–23, 2013.

Bibliography

[56] C. Bustamante, S. Smith, J. Liphardt, and D. Smith. Single-molecule studies of dna mechanics. *Current Opinion in Structural Biology*, 10(3):279–285, 2000.

[57] D. Anselmetti. Nanopores: Tiny holes with great promise. *Nature nanotechnology*, 7(2):81–82, 2012.

[58] C. Dekker. Single-molecule transport across an individual biomimetic nuclear pore complex. *Biophysical Journal*, 102(3):8a, 2012.

[59] C. Dekker. Solid-state nanopores. *Nature nanotechnology*, 2(4):209–215, 2007.

[60] O. Braha, L. Gu, L. Zhou, X. Lu, S. Cheley, and H. Bayley. Simultaneous stochastic sensing of divalent metal ions. *Nature biotechnology*, 18(9):1005–1007, 2000.

[61] J. Ettedgui, J. Kasianowicz, and A. Balijepalli. Single molecule discrimination of heteropolytungstates and their isomers in solution with a nanometer-scale pore. *Journal of the American Chemical Society*, 138(23):7228–7231, 2016.

[62] M. Ayub, D. Stoddart, and H. Bayley. Nucleobase recognition by truncated alpha-hemolysin pores. *ACS nano*, 9(8):7895–7903, 2015.

[63] D. Deamer and D. Branton. Characterization of nucleic acids by nanopore analysis. *Accounts of Chemical Research*, 35(10):817–825, 2002.

[64] A. Biesemans, M. Soskine, and G. Maglia. A protein rotaxane controls the translocation of proteins across a ClyA nanopore. *Nano letters*, 15(9):6076–6081, 2015.

[65] M. Pastoriza-Gallego, M. Breton, F. Discala, L. Auvray, J. Betton, and J. Pelta. Evidence of unfolded protein translocation through a protein nanopore. *ACS nano*, 8(11):11350–11360, 2014.

[66] F. Haque, S. Wang, C. Stites, L. Chen, C. Wang, and P. Guo. Single pore translocation of folded, double-stranded, and tetra-stranded DNA through channel of bacteriophage phi29 DNA packaging motor. *Biomaterials*, 53:744–752, 2015.

[67] H. Berman. The protein data bank. *Nucleic Acids Research*, 28(1):235–242, 2000.

[68] L. Steinbock, R. Bulushev, S. Krishnan, C. Raillon, and A. Radenovic. DNA translocation through low-noise glass nanopores. *ACS nano*, 7(12):11255–11262, 2013.

[69] D. Shenoy, A. Singh, W. Barger, and J. Kasianowicz. Method of stabilization of functional nanoscale pores for device applications, 2012. US Patent 8,294,007.

[70] A. Meller, L. Nivon, and D. Branton. Voltage-driven DNA translocations through a nanopore. *Physical review letters*, 86(15):3435–3438, 2001.

[71] H. Bayley. Designed membrane channels and pores. *Current Opinion in Biotechnology*, 10(1):94–103, 1999.

[72] S. Bhakdi and J. Tranum-Jensen. Alpha-toxin of staphylococcus aureus. *Microbiological reviews*, 55(4):733–751, 1991.

[73] L. Song, M. Hobaugh, C. Shustak, S. Cheley, H. Bayley, and J. Gouaux. Structure of staphylococcal alpha-hemolysin, a heptameric transmembrane pore. *Science (New York, N.Y.)*, 274(5294):1859–1866, 1996.

[74] S. Howorka, S. Cheley, and H. Bayley. Sequence-specific detection of individual DNA strands using engineered nanopores. *Nature biotechnology*, 19(7):636–639, 2001.

[75] M. Niederweis. Mycobacterial porins - new channel proteins in unique outer membranes. *Molecular Microbiology*, 49(5):1167–1177, 2003.

[76] L. Gu and J. Shim. Single molecule sensing by nanopores and nanopore devices. *The Analyst*, 135(3):441–451, 2010.

[77] M. Faller, M. Niederweis, and G. Schulz. The structure of a mycobacterial outer-membrane channel. *Science (New York, N.Y.)*, 303(5661):1189–1192, 2004.

[78] J. Craig, A. Laszlo, I. Derrington, B. Ross, H. Brinkerhoff, I. Nova, K. Doering, B. Tickman, M. Svet, and J. Gundlach. Direct detection of unnatural DNA nucleotides dNaM and d5SICS using the MspA nanopore. *PloS one*, 10(11):e0143253, 2015.

[79] B. Liang and L. Tamm. Structure of outer membrane protein G by solution NMR spectroscopy. *Proceedings of the National Academy of Sciences of the United States of America*, 104(41):16140–16145, 2007.

Bibliography

[80] S. Mari, S. Köster, C. Bippes, O. Yildiz, W. Kühlbrandt, and D. Muller. pH-induced conformational change of the beta-barrel-forming protein OmpG reconstituted into native E. coli lipids. *Journal of Molecular Biology*, 396(3):610–616, 2010.

[81] A. Perez-Rathke, M. Fahie, C. Chisholm, J. Liang, and M. Chen. Mechanism of OmpG pH-dependent gating from loop ensemble and single channel studies. *Journal of the American Chemical Society*, 140(3):1105–1115, 2018.

[82] P. Fürjes, Z. Fekete, L. Illés, A. L. Tóth, G. Battistig, and R. E. Gyurcsányi. Effects of the focused ion beam parameters on nanopore milling in solid state membranes. *Procedia Engineering*, 47:684–687, 2012.

[83] H. Kwok, K. Briggs, and V. Tabard-Cossa. Nanopore fabrication by controlled dielectric breakdown. *PloS one*, 9(3):e92880, 2014.

[84] A. Singer, M. Wanunu, W. Morrison, H. Kuhn, M. Frank-Kamenetskii, and A. Meller. Nanopore based sequence specific detection of duplex DNA for genomic profiling. *Nano letters*, 10(2):738–742, 2010.

[85] C. Merchant, K. Healy, M. Wanunu, V. Ray, N. Peterman, J. Bartel, M. Fischbein, K. Venta, Z. Luo, T. Charlie Johnson, and M. Drndić. DNA translocation through graphene nanopores. *Nano letters*, 10(8):2915–2921, 2010.

[86] A. Geim and K. Novoselov. The rise of graphene. *Nature materials*, 6(3):183–191, 2007.

[87] J. Larkin, R. Henley, D. Bell, T. Cohen-Karni, J. Rosenstein, and M. Wanunu. Slow DNA transport through nanopores in hafnium oxide membranes. *ACS nano*, 7(11):10121–10128, 2013.

[88] W. Chen, G. Liu, J. Ouyang, M. Gao, B. Liu, and Y. Zhao. Graphene nanopores toward DNA sequencing: a review of experimental aspects. *Science China Chemistry*, 60(6):721–729, 2017.

[89] N. Bell and U. Keyser. Nanopores formed by DNA origami: a review. *FEBS letters*, 588(19):3564–3570, 2014.

[90] H. Bayley and C. Martin. Resistive-pulse sensingfrom microbes to molecules. *Chemical Reviews*, 100(7):2575–2594, 2000.

[91] W. Shinwari, D. Zhitomirsky, I. Deen, P. Selvaganapathy, J. Deen, and D. Land-heer. Microfabricated reference electrodes and their biosensing applications. *Sensors (Basel, Switzerland)*, 10(3):1679–1715, 2010.

[92] D. Sawyer, A. Sobkowiak, and J. Roberts. *Electrochemistry for chemists*. Wiley, New York, 2nd edition, 1995.

[93] D. Ives. *Reference electrodes: Theory and practice*. Acad. Press, New York u.a., 2nd edition, 1983.

[94] S. Trasatti. The absolute electrode potential: an explanatory note. *Pure and Applied Chemistry*, 58(7):955–966, 1986.

[95] F. Scholz and A. Bond. *Electroanalytical Methods: Guide to Experiments and Applications*. Springer-Verlag Berlin Heidelberg, Berlin, Heidelberg, 2nd edition, 2010.

[96] G. Kickelbick. *Chemie für Ingenieure*. Pearson Studium, München, 2008.

[97] F. Moussy and D. Harrison. Prevention of the rapid degradation of subcutaneously implanted Ag/AgCl reference electrodes using polymer coatings. *Analytical chemistry*, 66(5):674–679, 1994.

[98] M. Sophocleous and J. Atkinson. A review of screen-printed silver/silver chloride (Ag/AgCl) reference electrodes potentially suitable for environmental potentiometric sensors. *Sensors and Actuators A: Physical*, 267:106–120, 2017.

[99] P. Zanello. *Inorganic Electrochemistry: Theory, Practice and Application*. Royal Society of Chemistry, Cambridge, 2003.

[100] G. Wedler. *Lehrbuch der physikalischen Chemie*. Wiley-VCH, Weinheim, 5th edition, 2010.

[101] B. Franklin, W. Brownrigg, and Farish. Of the stilling of waves by means of oil. *Philosophical Transactions of the Royal Society of London*, 64(0):445–460, 1774.

[102] G. Roberts, editor. *Langmuir-Blodgett Films*. Springer US, Boston, MA and s.l., 1990.

[103] J. Aitken. On the effect of oil on a stormy sea. *Proceedings of the Royal Society of Edinburgh*, 12:56–75, 1884.

Bibliography

[104] L. Rayleigh. Measurements of the amount of oil necessary in order to check the motions of camphor upon water. *Proceedings of the Royal Society of London*, 47(286-291):364–367, 1889.

[105] L. Rayleigh. Surface tension. *Nature*, 43(1115):437–439, 1891.

[106] A. Pockels. Relations between the surface-tension and relative contamination of water surfaces. *Nature*, 48(1233):152–154, 1893.

[107] I. Langmuir. The constitution and fundamental properties of solids and liquids. II. liquids. 1. *Journal of the American Chemical Society*, 39(9):1848–1906, 1917.

[108] K. Blodgett. Films built by depositing successive monomolecular layers on a solid surface. *Journal of the American Chemical Society*, 57(6):1007–1022, 1935.

[109] J. Pellicer, J. Manzanares, and S. Mafé. The physical description of elementary surface phenomena: Thermodynamics versus mechanics. *American Journal of Physics*, 63(6):542–547, 1995.

[110] M. Petty. *Langmuir-Blodgett films: An introduction.* Cambridge University Press, Cambridge, 1996.

[111] M. Sophocleous. Understanding and explaining surface tension and capillarity: an introduction to fundamental physics for water professionals. *Hydrogeology Journal*, 18(4):811–821, 2010.

[112] J. Dean and N. Lange, editors. *Lange's handbook of chemistry.* McGraw-Hill, New York, 11th edition, 1973.

[113] B. Keene. Review of data for the surface tension of pure metals. *International Materials Reviews*, 38(4):157–192, 1993.

[114] A. Ulman. *An Introduction to Ultrathin Organic Films: From Langmuir-Blodgett to Self-Assembly.* Elsevier Science, Burlington, 1991.

[115] K. Ariga. *Organized Organic Ultrathin Films: Fundamentals and Applications.* Wiley, Weinheim, 2013.

[116] S. Milner, J. Joanny, and P. Pincus. Buckling of Langmuir monolayers. *Europhysics Letters (EPL)*, 9(5):495–500, 1989.

[117] G. Overbeck, D. Hoenig, and D. Moebius. Visualization of first- and second-order phase transitions in eicosanol monolayers using Brewster angle microscopy. *Langmuir*, 9(2):555–560, 1993.

[118] S. Rivière, S. Hénon, J. Meunier, D. Schwartz, M. Tsao, and C. Knobler. Textures and phase transitions in Langmuir monolayers of fatty acids. a comparative Brewster angle microscope and polarized fluorescence microscope study. *The Journal of Chemical Physics*, 101(11):10045–10051, 1994.

[119] J. Rodríguez Patino, C. Sánchez, and R. Rodríguez Niño. Morphological and structural characteristics of monoglyceride monolayers at the air-water interface observed by Brewster angle microscopy. *Langmuir*, 15(7):2484–2492, 1999.

[120] M. Lösche, E. Sackmann, and H. Möhwald. A fluorescence microscopic study concerning the phase diagram of phospholipids. *Berichte der Bunsengesellschaft für physikalische Chemie*, 87(10):848–852, 1983.

[121] H. McConnell, L. Tamm, and R. Weis. Periodic structures in lipid monolayer phase transitions. *Proceedings of the National Academy of Sciences of the United States of America*, 81(10):3249–3253, 1984.

[122] E. Ruckenstein. On the nature of the liquid expanded/liquid condensed phase transition in monolayers of polar molecules. *Journal of colloid and interface science*, 196(2):313–315, 1997.

[123] I. Shieh and J. Zasadzinski. Visualizing monolayers with a water-soluble fluorophore to quantify adsorption, desorption, and the double layer. *Proceedings of the National Academy of Sciences of the United States of America*, 112(8):E826–35, 2015.

[124] H. Möhwald. Phospholipid and phospholipid-protein monolayers at the air/water interface. *Annual review of physical chemistry*, 41:441–476, 1990.

[125] A. Mingotaud, C. Mingotaud, and L. Patterson. *Handbook of monolayers*. Acad. Press, San Diego, 1993.

[126] H. Heller, M. Schaefer, and K. Schulten. Molecular dynamics simulation of a bilayer of 200 lipids in the gel and in the liquid crystal phase. *The Journal of Physical Chemistry*, 97(31):8343–8360, 1993.

Bibliography

[127] S. Mabrey and J. Sturtevant. Investigation of phase transitions of lipids and lipid mixtures by sensitivity differential scanning calorimetry. *Proceedings of the National Academy of Sciences of the United States of America*, 73(11):3862–3866, 1976.

[128] M. Eze. Phase transitions in phospholipid bilayers: Lateral phase separations play vital roles in biomembranes. *Biochemical Education*, 19(4):204–208, 1991.

[129] E. Honig. The transition from Y- to X-type Langmuir-Blodgett films. *Langmuir*, 5(3):882–883, 1989.

[130] R. Popovitz-Biro, K. Hill, M. Landau, M. Lahav, L. Leiserowitz, J. Sagiv, H. Hsiung, R. Meredith, and H. Vanherzeele. A new class of stable head-to tail (z-type) langmuir blodgett films. a second harmonic generation study. *Journal of the American Chemical Society*, 110(8):2672–2674, 1988.

[131] P. Vincett, W. Barlow, F. Boyle, J. Finney, and G. Roberts. Preparation of Langmuir-Blodgett "built-up" multilayer films of a lightly substituted model aromatic, anthracene. *Thin Solid Films*, 60(3):265–277, 1979.

[132] R. Jones, R. Tredgold, and P. Hodge. Langmuir-Blodgett films of simple esterified porphyrins. *Thin Solid Films*, 99(1-3):25–32, 1983.

[133] T. Richardson, G. Roberts, M. Polywka, and S. Davies. Preparation and characterization of organotransition metal Langmuir-Blodgett films. *Thin Solid Films*, 160(1-2):231–239, 1988.

[134] J. Rabe and S. Buchholz. Commensurability and mobility in two-dimensional molecular patterns on graphite. *Science (New York, N.Y.)*, 253(5018):424–427, 1991.

[135] E. Verveniotis, Y. Okawa, M. Makarova, Y. Koide, J. Liu, B. Šmíd, K. Watanabe, T. Taniguchi, K. Komatsu, T. Minari, X. Liu, C. Joachim, and M. Aono. Self-assembling diacetylene molecules on atomically flat insulators. *Physical chemistry chemical physics : PCCP*, 18(46):31600–31605, 2016.

[136] S. de Feyter and F. de Schryver. Two-dimensional supramolecular self-assembly probed by scanning tunneling microscopy. *Chemical Society Reviews*, 32(3):139–150, 2003.

[137] J. Bikerman. On the formation and structure of multilayers. *Proceedings of the Royal Society A: Mathematical, Physical and Engineering Sciences*, 170(940):130–144, 1939.

[138] S. Harirchian-Saei, M. Wang, B. Gates, and M. Moffitt. Patterning block copolymer aggregates via langmuir-blodgett transfer to microcontact-printed substrates. *Langmuir : the ACS journal of surfaces and colloids*, 26(8):5998–6008, 2010.

[139] F. Kopp, P. Fringeli, K. Mühlethaler, and H. Günthard. Spontaneous rearrangement in langmuir-blodgett layers of tripalmitin studied by means of atr infrared spectroscopy and electron microscopy. *Zeitschrift für Naturforschung C*, 30(11-12):711–717, 1975.

[140] J. Kmetko, A. Datta, G. Evmenenko, and P. Dutta. The effects of divalent ions on langmuir monolayer and subphase structure: A grazing-incidence diffraction and bragg rod study. *The Journal of Physical Chemistry B*, 105(44):10818–10825, 2001.

[141] M. Buhaenko, J. Goodwin, R. Richardson, and M. Daniel. The influence of shear viscosity of spread monolayers on the Langmuir-Blodgett process. *Thin Solid Films*, 134(1-3):217–226, 1985.

[142] I. Peterson and G. Russell. The deposition and structure of Langmuir-Blodgett films of long-chain acids. *Thin Solid Films*, 134(1-3):143–152, 1985.

[143] B. Malcolm. The flow of molecular monolayers in relation to the design of Langmuir troughs and the deposition of Langmuir-Blodgett films. *Journal of Physics E: Scientific Instruments*, 21(6):603–607, 1988.

[144] K. Urban. Is science prepared for atomic-resolution electron microscopy? *Nature materials*, 8(4):260–262, 2009.

[145] R. Bennewitz. Friction force microscopy. *Materials Today*, 8(5):42–48, 2005.

[146] K. Wang, J. Cheng, S. Yao, Y. Lu, L. Ji, and D. Xu. Determination of electrostatic force and its characteristics based on phase difference by amplitude modulation atomic force microscopy. *Nanoscale research letters*, 11(1):548, 2016.

Bibliography

[147] I. Estevez, P. Chrétien, O. Schneegans, and F. Houzé. Specific methodology for capacitance imaging by atomic force microscopy: A breakthrough towards an elimination of parasitic effects. *Applied Physics Letters*, 104(8):083108, 2014.

[148] D. Passeri, C. Dong, M. Reggente, L. Angeloni, M. Barteri, F. Scaramuzzo, F. de Angelis, F. Marinelli, F. Antonelli, F. Rinaldi, C. Marianecci, M. Carafa, A. Sorbo, D. Sordi, I. Arends, and M. Rossi. Magnetic force microscopy: quantitative issues in biomaterials. *Biomatter*, 4, 2014.

[149] W. Frammelsberger, G. Benstetter, J. Kiely, and R. Stamp. C-AFM-based thickness determination of thin and ultra-thin SiO_2 films by use of different conductive-coated probe tips. *Applied Surface Science*, 253(7):3615–3626, 2007.

[150] Y. Efremov, W. Wang, S. Hardy, R. Geahlen, and A. Raman. Measuring nanoscale viscoelastic parameters of cells directly from AFM force-displacement curves. *Scientific reports*, 7(1):1541, 2017.

[151] M. Nonnenmacher, M. O'Boyle, and H. Wickramasinghe. Kelvin probe force microscopy. *Physical review letters*, 58(25):2921–2923, 1991.

[152] O. Schneegans, F. Houze, R. Meyer, and L. Boyer. Study of the local electrical properties of metal surfaces using an AFM with a conducting probe. *IEEE Transactions on Components, Packaging, and Manufacturing Technology: Part A*, 21(1):76–81, 1998.

[153] G. Binnig and H. Rohrer. Scanning tunneling microscopy. *Journal of Applied Physics*, 126(1-3):236–244, 1983.

[154] G. Haugstad. *Atomic force microscopy: Exploring basic modes and advanced applications*. John Wiley & Sons, Hoboken, N.J, 2012.

[155] O. Custance, R. Perez, and S. Morita. Atomic force microscopy as a tool for atom manipulation. *Nature nanotechnology*, 4(12):803–810, 2009.

[156] E. Meyer, H. Hug, and R. Bennewitz. *Scanning probe microscopy: The lab on a tip*. Physics and astronomy online library. Springer, Berlin, 2004.

[157] K. Nieradka, G. Małozięć, D. Kopiec, P. Grabiec, P. Janus, A. Sierakowski, and T. Gotszalk. Expanded beam deflection method for simultaneous measurement of displacement and vibrations of multiple microcantilevers. *Review of Scientific Instruments*, 82(10):105112, 2011.

132

[158] S. Alexander, L. Hellemans, O. Marti, J. Schneir, V. Elings, P. Hansma, M. Longmire, and J. Gurley. An atomic-resolution atomic-force microscope implemented using an optical lever. *Journal of Applied Physics*, 65(1):164–167, 1989.

[159] J. Lübbe, M. Temmen, S. Rode, P. Rahe, A. Kühnle, and M. Reichling. Thermal noise limit for ultra-high vacuum noncontact atomic force microscopy. *Beilstein journal of nanotechnology*, 4:32–44, 2013.

[160] D. Rugar, H. Mamin, and P. Guethner. Improved fiber-optic interferometer for atomic force microscopy. *Applied Physics Letters*, 55(25):2588–2590, 1989.

[161] F. Giessibl. High-speed force sensor for force microscopy and profilometry utilizing a quartz tuning fork. *Applied Physics Letters*, 73(26):3956–3958, 1998.

[162] G. Binnig, C. Quate, and C. Gerber. Atomic force microscope. *Physical review letters*, 56(9):930–933, 1986.

[163] W. Pauli. The connection between spin and statistics. *Physical Review*, 58(8):716–722, 1940.

[164] R. Pérez, I. Štich, M. Payne, and K. Terakura. Surface-tip interactions in non-contact atomic-force microscopy on reactive surfaces: Si(111). *Physical Review B*, 58(16):10835–10849, 1998.

[165] C. Hamaker. The london—van der waals attraction between spherical particles. *Physica*, 4(10):1058–1072, 1937.

[166] M. Saint Jean, S. Hudlet, C. Guthmann, and J. Berger. Van der Waals and capacitive forces in atomic force microscopies. *Journal of Applied Physics*, 86(9):5245–5248, 1999.

[167] R. Mérindol. *Layer-by-layer assembly of strong bio-inspired nanocomposites.* PhD thesis, University of Strasbourg, 9 2014.

[168] H. Butt. Electrostatic interaction in atomic force microscopy. *Biophysical Journal*, 60(4):777–785, 1991.

[169] T. Albrecht, S. Akamine, T. Carver, and C. Quate. Microfabrication of cantilever styli for the atomic force microscope. *Journal of Vacuum Science & Technology A: Vacuum, Surfaces, and Films*, 8(4):3386–3396, 1990.

Bibliography

[170] S. Magonov. *Surface analysis with STM and AFM: Experimental and theoretical aspects of image analysis.* VCH, Weinheim Germany and New York, 2008.

[171] N. Burnham, R. Colton, and H. Pollock. Interpretation issues in force microscopy. *Journal of Vacuum Science & Technology A: Vacuum, Surfaces, and Films*, 9(4):2548–2556, 1991.

[172] Y. Gan. Atomic and subnanometer resolution in ambient conditions by atomic force microscopy. *Surface Science Reports*, 64(3):99–121, 2009.

[173] D. Smith. Limits of force microscopy. *Review of Scientific Instruments*, 66(5):3191–3195, 1995.

[174] A. Simon, C. Gounou, S. Tan, L. Tiefenauer, M. Di Berardino, and A. Brisson. Free-standing lipid films stabilized by annexin-a5. *Biochimica et biophysica acta*, 1828(11):2739–2744, 2013.

[175] X. Zhang, A. Beyer, and A. Gölzhäuser. Mechanical characterization of carbon nanomembranes from self-assembled monolayers. *Beilstein journal of nanotechnology*, 2:826–833, 2011.

[176] B. Bhushan. *Springer Handbook of Nanotechnology.* Springer-Verlag, Berlin/Heidelberg, 2004.

[177] B. Voigtländer. *Scanning probe microscopy: Atomic force microscopy and scanning tunneling microscopy.* NanoScience and Technology. Springer, Heidelberg, 2015.

[178] Q. Zhong, D. Inniss, K. Kjoller, and V. Elings. Fractured polymer/silica fiber surface studied by tapping mode atomic force microscopy. *Surface Science Letters*, 290(1-2):L688–L692, 1993.

[179] A. Kühle, A. Sorensen, and J. Bohr. Role of attractive forces in tapping tip force microscopy. *Journal of Applied Physics*, 81(10):6562–6569, 1997.

[180] E. Goksu, J. Vanegas, C. Blanchette, W. Lin, and M. Longo. AFM for structure and dynamics of biomembranes. *Biochimica et biophysica acta*, 1788(1):254–266, 2009.

134

[181] F. Moreno-Herrero, J. Colchero, J. Gómez-Herrero, and A. Baró. Atomic force microscopy contact, tapping, and jumping modes for imaging biological samples in liquids. *Physical review. E, Statistical, nonlinear, and soft matter physics*, 69(3 Pt 1):031915, 2004.

[182] J. Tamayo and R. García. Deformation, contact time, and phase contrast in tapping mode scanning force microscopy. *Langmuir*, 12(18):4430–4435, 1996.

[183] J. Notte, B. Ward, N. Economou, R. Hill, R. Percival, L. Farkas, S. McVey, D. Seiler, A. Diebold, R. McDonald, M. Garner, D. Herr, R. Khosla, and E. Secula. An introduction to the helium ion microscope. In *AIP Conference Proceedings*, pages 489–496. AIP, 27-29 March 2007.

[184] J. Bozzola and L. Russell. *Electron microscopy: Principles and techniques for biologists.* The Jones and Bartlett series in biology. Jones and Bartlett, Boston, 2nd edition, 2006.

[185] K. Narayan and S. Subramaniam. Focused ion beams in biology. *Nature methods*, 12(11):1021–1031, 2015.

[186] B. Ward, J. Notte, and N. Economou. Helium ion microscope: A new tool for nanoscale microscopy and metrology. *Journal of Vacuum Science & Technology B: Microelectronics and Nanometer Structures*, 24(6):2871, 2006.

[187] M. Joens, C. Huynh, J. Kasuboski, D. Ferranti, Y. Sigal, F. Zeitvogel, M. Obst, C. Burkhardt, K. Curran, S. Chalasani, L. Stern, B. Goetze, and J. Fitzpatrick. Helium ion microscopy (him) for the imaging of biological samples at sub-nanometer resolution. *Scientific reports*, 3:3514, 2013.

[188] G. Hlawacek and A. Gölzhäuser, editors. *Helium Ion Microscopy.* NanoScience and Technology. Springer International Publishing, Cham and s.l., 2016.

[189] G. Hlawacek, V. Veligura, R. van Gastel, and B. Poelsema. Helium ion microscopy. *Journal of Vacuum Science & Technology B, Nanotechnology and Microelectronics: Materials, Processing, Measurement, and Phenomena*, 32(2):020801, 2014.

[190] B. Ward and N. Notte, J. Economou. Helium-ion microscopy. *Photonics spectra*, 41(8):68–70, 2007.

Bibliography

[191] D. Bell, M. Lemme, L. Stern, J. Williams, and C. Marcus. Precision cutting and patterning of graphene with helium ions. *Nanotechnology*, 20(45):455301, 2009.

[192] Carl Zeiss Microscopy GmbH. Zeiss orion nanofab. Technical report, Product Information Version 2.0, 2018.

[193] U. Kubitscheck. *Fluorescence Microscopy: From Principles to Biological Applications*. Wiley-Blackwell, s.l., 1st edition, 2013.

[194] D. Penney, J. Powers, M. Frank, C. Willis, and C. Churukian. Analysis and testing of biological stains - the biological stain commission procedures. *Biotechnic and Histochemistry*, 77(5):237–275, 2002.

[195] J. Lakowicz. *Principles of fluorescence spectroscopy*. Springer, New York, NY, 3rd edition, 2010.

[196] H. Hsiao, J. Chang, and P. Simeonov. Preventing emergency vehicle crashes: Status and challenges of human factors issues. *Human factors*, 60(7):1048–1072, 2018.

[197] G. Stokes. On the change of refrangibility of light. *Philosophical Transactions of the Royal Society of London*, 142(0):463–562, 1852.

[198] M. Velázquez, T. Alejo, D. López-Díaz, B. Martín-García, and María D. Merchán. Langmuir–blodgett methodology: A versatile technique to build 2d material films. In Pramoda Kumar Nayak, editor, *Two-dimensional Materials - Synthesis, Characterization and Potential Applications*. InTech, 2016.

[199] K. Ariga, Y. Yamauchi, T. Mori, and J. Hill. 25th anniversary article: what can be done with the langmuir-blodgett method? recent developments and its critical role in materials science. *Advanced materials (Deerfield Beach, Fla.)*, 25(45):6477–6512, 2013.

[200] https://www.quantifoil.com/index.php?name=quantifoil, 03.01.2019.

[201] L. Rubinger, L. Moreira, A. Cury, N. Fontes, A. Neves, A. Meneguzzi, and A. Ferreira. Langmuir-blodgett and langmuir-schaefer films of poly(5-amino-1-naphthol) conjugated polymer. *Applied Surface Science*, 253(2):543–548, 2006.

[202] A. Jyoti, M. Prokop, J. Li, D. Vollhardt, Y. Kwok, R. Miller, H. Möhwald, and W. Neumann. An investigation of the compression rate dependence on the surface pressure-surface area isotherm for a dipalmitoyl phosphatidylcholine monolayer at the air/water interface. *Colloids and Surfaces A: Physicochemical and Engineering Aspects*, 116(1-2):173–180, 1996.

[203] E Honig, J. Hengst, and D. Den Engelsen. Langmuir-blodgett deposition ratios. *Journal of colloid and interface science*, 45(1):92–102, 1973.

[204] G. Wegner. Topochemische reaktionen von monomeren mit konjugierten dreifachbindungen / tochemical reactions of monomers with conjugated triple bonds. *Zeitschrift für Naturforschung B*, 24(7):824–832, 1969.

[205] B. Tieke. Polymerization of butadiene and butadiyne (diacetylene) derivatives in layer structures. In *Analysis/Reactions/Morphology*, volume 71 of *Advances in Polymer Science*, pages 79–151. Springer, Berlin and Heidelberg, 1985.

[206] R. Chance. Chromism in polydiacetylene solutions and crystals. *Macromolecules*, 13(2):396–398, 1980.

[207] S. Okada, S. Peng, W. Spevak, and D. Charych. Color and chromism of polydiacetylene vesicles. *Accounts of Chemical Research*, 31(5):229–239, 1998.

[208] R. Carpick, D. Sasaki, M. Marcus, A. Eriksson, and A. Burns. Polydiacetylene films: a review of recent investigations into chromogenic transitions and nanomechanical properties. *Journal of Physics: Condensed Matter*, 16(23):R679–R697, 2004.

[209] S. Schrettl, C. Stefaniu, C. Schwieger, G. Pasche, E. Oveisi, Y. Fontana, A. Fontcuberta i Morral, J. Reguera, R. Petraglia, C. Corminboeuf, G. Brezesinski, and H. Frauenrath. Functional carbon nanosheets prepared from hexayne amphiphile monolayers at room temperature. *Nature chemistry*, 6(6):468–476, 2014.

[210] W. Spevak, J. Nagy, and D. Charych. Molecular assemblies of functionalized polydiacetylenes. *Advanced Materials*, 7(1):85–89, 1995.

[211] R. Pabst, H. Ringsdorf, H. Koch, and K. Dose. Light-driven proton transport of bacteriorhodopsin incorporated into long-term stable liposomes of a polymerizable sulfolipid. *FEBS letters*, 154(1):5–9, 1983.

Bibliography

[212] D. Anselmetti and A. Gölzhäuser. Converting molecular monolayers into functional membranes. *Angewandte Chemie (International ed. in English)*, 53(46):12300–12302, 2014.

[213] E. Lopez, D. O'Brien, and T. Whitesides. Structural effects on the photopolymerization of bilayer membranes. *Journal of the American Chemical Society*, 104(1):305–307, 1982.

[214] G. Exarhos, W. Risen, and R. Baughman. Resonance raman study of the thermochromic phase transition of a polydiacetylene. *Journal of the American Chemical Society*, 98(2):481–487, 1976.

[215] M. Kamath, H. Kim, L. Li, J. Kumar, S. Tripathy, N. Babu, and S. Talwar. Kinetics of diacetylene polymerization: an ft-raman study. *Macromolecules*, 26(22):5954–5958, 1993.

[216] V. Enkelmann and B. Lando. Poly1,2-bis[4-(phenylcarbamoyloxy)-n-butyl]-1-buten-3-ynylene. *Acta Crystallographica Section B Structural Crystallography and Crystal Chemistry*, 34(7):2352–2353, 1978.

[217] R. Fischetti, M. Filipkowski, A. Garito, and K. Blasie. Profile structures of ultrathin periodic and nonperiodic multilayer films containing a disubstituted diacetylene by high-resolution x-ray diffraction. *Physical Review B*, 37(9):4714–4726, 1988.

[218] B. Lee. Fourier transform infrared spectroscopic studies of microstructures formed from 1,2-bis(10,12-tricosadiynoyl)-sn-glycero-3-phosphocholine. *The Journal of Physical Chemistry*, 93(2):926–931, 1989.

[219] H. Tien, S. Carbone, and E. Dawidowicz. Formation of "black" lipid membranes by oxidation products of cholesterol. *Nature*, 212(5063):718–719, 1966.

[220] D. Ives, editor. *Reference electrodes: theory and practice.* Academic Press Inc., New York, 2nd edition, 1969.

[221] A. Honigmann, C. Walter, F. Erdmann, C. Eggeling, and R. Wagner. Characterization of horizontal lipid bilayers as a model system to study lipid phase separation. *Biophysical Journal*, 98(12):2886–2894, 2010.

[222] L. Galla. *Nanopore Modifications with Lipid Bilayer Membranes*. PhD thesis, University of Bielefeld, 5 2014.

[223] F. Mirabella, editor. *Internal reflection spectroscopy: Theory and applications*, volume 15 of *Practical spectroscopy*. Dekker, New York, 1993.

[224] P. Yager and P. Schoen. Formation of tubules by a polymerizable surfactant. *Molecular Crystals and Liquid Crystals*, 106(3-4):371–381, 1984.

[225] L. Bourdieu, D. Chatenay, J. Daillant, and D. Luzet. Polymerization of a diacetylenic phospholipid monolayer at the air-water interface. *Journal de Physique II*, 4(1):37–58, 1994.

[226] O. Albrecht, H. Gruler, and E. Sackmann. Polymorphism of phospholipid monolayers. *Journal de Physique*, 39(3):301–313, 1978.

[227] S. Baoukina, L. Monticelli, S. Marrink, and P. Tieleman. Pressure-area isotherm of a lipid monolayer from molecular dynamics simulations. *Langmuir*, 23(25):12617–12623, 2007.

[228] M. Lösche, J. Rabe, A. Fischer, B. Rucha, W. Knoll, and H. Möhwald. Microscopically observed preparation of langmuir-blodgett films. *Thin Solid Films*, 117(4):269–280, 1984.

[229] T. McIntosh. Differences in hydrocarbon chain tilt between hydrated phosphatidylethanolamine and phosphatidylcholine bilayers. a molecular packing model. *Biophysical Journal*, 29(2):237–245, 1980.

[230] T. Okazaki, T. Inaba, Y. Tatsu, R. Tero, T. Urisu, and K. Morigaki. Polymerized lipid bilayers on a solid substrate: morphologies and obstruction of lateral diffusion. *Langmuir*, 25(1):345–351, 2009.

[231] D. Britt, G. Hofmann, D. Möbius, and S. Hell. Influence of substrate properties on the topochemical polymerization of diacetylene monolayers. *Langmuir*, 17(12):3757–3765, 2001.

[232] K. Ogawa, H. Tamura, M. Hatada, and T. Ishihara. Study of photoreaction processes of pda langmuir films. *Langmuir*, 4(4):903–906, 1988.

Bibliography

[233] J. Rabe, J. Rabolt, C. Brown, and J. Swalen. Polymerization of two unsaturated fatty acid esters in langmuir-blodgett films as studied by ir spectroscopy. *Thin Solid Films*, 133(1-4):153–159, 1985.

[234] D. Bloor and R. Chance. *Polydiacetylenes*. Springer Netherlands, Dordrecht, 1985.

[235] G. Odian. chapter Radical Chain Polymerization, pages 255–256. Wiley-Interscience, New York, USA, 4th edition, 2004.

[236] J. Lambert and A. Jaworski, editors. *Organic structural spectroscopy*. Prentice Hall Pearson, Boston, Mass., 2nd edition, 2011.

[237] D. Batchelder. Colour and chromism of conjugated polymers. *Contemporary Physics*, 29(1):3–31, 1988.

[238] G. Lieser, B. Tieke, and G. Wegner. Structure, phase transitions and polymerizability of multilayers of some diacetylene monocarboxylic acids. *Thin Solid Films*, 68(1):77–90, 1980.

[239] A. Rudolph and T. Burke. A fourier-transform infrared spectroscopic study of the polymorphic phase behavior of 1,2-bis(tricosa-10,12-diynoyl)-sn-glycero-3-phosphocholine; a polymerizable lipid which forms novel microstructures. *Biochimica et Biophysica Acta (BBA) - Biomembranes*, 902(3):349–359, 1987.

[240] K. Tamm and S. Tatulian. Infrared spectroscopy of proteins and peptides in lipid bilayers. *Quarterly reviews of biophysics*, 30(4):365–429, 1997.

[241] M. Roman and M. Baranska. Vibrational and theoretical study of diacetylenic acids. *Spectrochimica Acta Part A: Molecular and Biomolecular Spectroscopy*, 137:652–660, 2015.

[242] S. Magonov, V. Elings, and M. Whangbo. Phase imaging and stiffness in tapping-mode atomic force microscopy. *Surface Science*, 375(2):L385–L391, 1997.

[243] J. Elemans, S. Lei, and S. de Feyter. Molecular and supramolecular networks on surfaces: from two-dimensional crystal engineering to reactivity. *Angewandte Chemie (International ed. in English)*, 48(40):7298–7332, 2009.

[244] S. Arisawa, T. Fujii, T. Okane, and R. Yamamoto. Afm investigation of microstructures of diacetylene langmuir-blodgett films. *Applied Surface Science*, 60-61:321–325, 1992.

[245] S. de Feyter and F. de Schryver. Self-assembly at the liquid/solid interface: Stm reveals. *The Journal of Physical Chemistry B*, 109(10):4290–4302, 2005.

[246] X. Yin, L. Wan, Z. Yang, and J. Yu. Self-organization of surfactant molecules on solid surface: an stm study of sodium alkyl sulfonates. *Applied Surface Science*, 240(1-4):13–18, 2005.

[247] A. Barraud. Polymerization in langmuir-blodgett films and resist applications. *Thin Solid Films*, 99(1-3):317–321, 1983.

[248] C. Jones, C. Petty, G. Roberts, G. Davies, J. Yarwood, M. Ratcliffe, and W. Barton. Ir studies of pyroelectric langmuir-blodgett films. *Thin Solid Films*, 155(2):187–195, 1987.

[249] G. Decher, J. Maclennan, U. Sohling, and J. Reibel. Creation and structural comparison of ultrathin film assemblies: transferred freely suspended films and langmuir-blodgett films of liquid crystals. *Thin Solid Films*, 210-211:504–507, 1992.

[250] G. Mao, D. Chen, H. Handa, W. Dong, D. Kurth, and H. Möhwald. Deposition and aggregation of aspirin molecules on a phospholipid bilayer pattern. *Langmuir*, 21(2):578–585, 2005.

[251] Q. Chen, H. Yan, C. Yan, G. Pan, L. Wan, G. Wen, and D. Zhang. Stm investigation of the dependence of alkane and alkane (c18h38, c19h40) derivatives self-assembly on molecular chemical structure on hopg surface. *Surface Science*, 602(6):1256–1266, 2008.

[252] D. Shenoy, A. Singh, W. Barger, and J. Kasianowicz. Method of stabilization of functional nanoscale pores for device applications, 2012. US Patent 8,294,007.

[253] S. Kara, S. Afonin, O. Babii, A. Tkachenko, I. Komarov, and A. Ulrich. Diphytanoyl lipids as model systems for studying membrane-active peptides. *Biochimica et biophysica acta. Biomembranes*, 1859(10):1828–1837, 2017.

Bibliography

[254] I. Mey, M. Stephan, E. Schmitt, M. Müller, M. Ben Amar, C. Steinem, and A. Janshoff. Local membrane mechanics of pore-spanning bilayers. *Journal of the American Chemical Society*, 131(20):7031–7039, 2009.

[255] J. Israelachvili. Strength of van der waals attraction between lipid bilayers. *Langmuir*, 10(9):3369–3370, 1994.

[256] George Christou, Dante Gatteschi, David N. Hendrickson, and Roberta Sessoli. Single-molecule magnets. *MRS Bulletin*, 25(11):66–71, 2000.

[257] J. Oldengott. *Optimization of Single-Molecule Magnets and their Embedding into Two-Dimensional Polymers*. PhD thesis, University of Bielefeld, 5 2017.

[258] L. Bogani and W. Wernsdorfer. Molecular spintronics using single-molecule magnets. In P. Rodgers, editor, *Nanoscience and technology*, pages 194–201. Macmillan Publishers Ltd, London and Singapore, 2010.

[259] H. Bouas-Laurent, J. Desvergne, A. Castellan, and R. Lapouyade. Photodimerization of anthracenes in fluid solution: structural aspects. *Chemical Society Reviews*, 29(1):43–55, 2000.

[260] V. Kaganer, H. Möhwald, and P. Dutta. Structure and phase transitions in langmuir monolayers. *Reviews of Modern Physics*, 71(3):779–819, 1999.

[261] D. Gatteschi, A. Cornia, M. Mannini, and R. Sessoli. Organizing and addressing magnetic molecules. *Inorganic chemistry*, 48(8):3408–3419, 2009.

[262] P. Payamyar, B. King, H. Öttinger, and D. Schlüter. Two-dimensional polymers: concepts and perspectives. *Chemical communications (Cambridge, England)*, 52(1):18–34, 2016.

[263] C. Schäfer, R. Eckel, R. Ros, J. Mattay, and D. Anselmetti. Photochemical single-molecule affinity switch. *Journal of the American Chemical Society*, 129(6):1488–1489, 2007.

[264] G. Breton and X. Vang. Photodimerization of anthracene. *Journal of Chemical Education*, 75(1):81, 1998.

[265] C. Miller. *Ion Channel Reconstitution*. Springer, New York, NY, 2013.

[266] R. Latorre and O. Alvarez. Voltage-dependent channels in planar lipid bilayer membranes. *Physiological reviews*, 61(1):77–150, 1981.

[267] H. Wang and D. Branton. Nanopores with a spark for single-molecule detection. *Nature biotechnology*, 19(7):622–623, 2001.

[268] T. Sutherland, Y. Long, R. Stefureac, I. Bediako-Amoa, H. Kraatz, and J. Lee. Structure of peptides investigated by nanopore analysis. *Nano letters*, 4(7):1273–1277, 2004.

[269] D. Wong, T. Jeon, and J. Schmidt. Single molecule measurements of channel proteins incorporated into biomimetic polymer membranes. *Nanotechnology*, 17(15):3710–3717, 2006.

[270] H. Fujiwara, M. Fujihara, and T. Ishiwata. Dynamics of the spontaneous formation of a planar phospholipid bilayer: A new approach by simultaneous electrical and optical measurements. *The Journal of Chemical Physics*, 119(13):6768–6775, 2003.

[271] A. Beerlink, S. Thutupalli, M. Mell, M. Bartels, P. Cloetens, S. Herminghaus, and T. Salditt. X-ray propagation imaging of a lipid bilayer in solution. *Soft Matter*, 8(17):4595, 2012.

[272] M. Naumowicz, A. Petelska, and Z. Figaszewski. Capacitance and resistance of the bilayer lipid membrane formed of phosphatidylcholine and cholesterol. *Cellular & molecular biology letters*, 8(1):5–18, 2003.

[273] S. White. A study of lipid bilayer membrane stability using precise measurements of specific capacitance. *Biophysical Journal*, 10(12):1127–1148, 1970.

[274] R. Fettiplace, M. Andrews, and A. Haydon. The thickness, composition and structure of some lipid bilayers and natural membranes. *The Journal of membrane biology*, 5(3):277–296, 1971.

[275] G. Ashcroft, L. Coster, and R. Smith. The molecular organisation of bimolecular lipid membranes. the dielectric structure of the hydrophilic/hydrophobic interface. *Biochimica et Biophysica Acta (BBA) - Biomembranes*, 643(1):191–204, 1981.

[276] Y. Wu, K. He, S. Ludtke, and H. Huang. X-ray diffraction study of lipid bilayer membranes interacting with amphiphilic helical peptides: diphytanoyl phosphatidylcholine with alamethicin at low concentrations. *Biophysical Journal*, 68(6):2361–2369, 1995.

[277] T. Baba, Y. Toshima, H. Minamikawa, M. Hato, K. Suzuki, and N. Kamo. Formation and characterization of planar lipid bilayer membranes from synthetic phytanyl-chained glycolipids. *Biochimica et Biophysica Acta (BBA) - Biomembranes*, 1421(1):91–102, 1999.

[278] A. Velikonja, P. Kramar, D. Miklavčič, and A. Maček Lebar. Specific electrical capacitance and voltage breakdown as a function of temperature for different planar lipid bilayers. *Bioelectrochemistry (Amsterdam, Netherlands)*, 112:132–137, 2016.

[279] T. Jeon, J. Poulos, and J. Schmidt. Long-term storable and shippable lipid bilayer membrane platform. *Lab on a chip*, 8(10):1742–1744, 2008.

[280] A. Soloaga, J. Ramírez, and F. Goñi. Reversible denaturation, self-aggregation, and membrane activity of escherichia coli alpha-hemolysin, a protein stable in 6 m urea. *Biochemistry*, 37(18):6387–6393, 1998.

[281] W. Haynes and D. Lide, editors. *CRC handbook of chemistry and physics: A ready-reference book of chemical and physical data*. CRC Press, Boca Raton, Fla., 91th edition, 2010.

[282] http://myweb.wit.edu/sandinic/research/conductivity23.01.2019.

[283] G. Oukhaled, L. Bacri, J. Mathé, J. Pelta, and L. Auvray. Effect of screening on the transport of polyelectrolytes through nanopores. *Europhysics Letters (EPL)*, 82(4):48003, 2008.

[284] J. Bafna and G. Soni. Fabrication of low noise borosilicate glass nanopores for single molecule sensing. *PloS one*, 11(6):e0157399, 2016.

[285] J. Li and D. Talaga. The distribution of dna translocation times in solid-state nanopores. *Journal of Physics: Condensed Matter*, 22(45):454129, 2010.

[286] K. Morigaki, H. Schönherr, and T. Okazaki. Polymerization of diacetylene phospholipid bilayers on solid substrate: influence of the film deposition temperature. *Langmuir*, 23(24):12254–12260, 2007.

[287] Z. Siwy and S. Howorka. Engineered voltage-responsive nanopores. *Chemical Society reviews*, 39(3):1115–1132, 2010.

[288] S. Kowalczyk, A. Grosberg, Y. Rabin, and C. Dekker. Modeling the conductance and dna blockade of solid-state nanopores. *Nanotechnology*, 22(31):315101, 2011.

[289] C. Wen, Z. Zhang, and S. Zhang. Physical model for rapid and accurate determination of nanopore size via conductance measurement. *ACS sensors*, 2(10):1523–1530, 2017.

[290] C. Frament and J. Dwyer. Conductance-based determination of solid-state nanopore size and shape: An exploration of performance limits. *The journal of physical chemistry. C, Nanomaterials and interfaces*, 116(44):23315–23321, 2012.

[291] J. Hall. Access resistance of a small circular pore. *The Journal of General Physiology*, 66(4):531–532, 1975.

[292] R. Smeets, U. Keyser, D. Krapf, M. Wu, N. Dekker, and C. Dekker. Salt dependence of ion transport and dna translocation through solid-state nanopores. *Nano letters*, 6(1):89–95, 2006.

[293] E. Nightingale. Phenomenological theory of ion solvation. effective radii of hydrated ions. *The Journal of Physical Chemistry*, 63(9):1381–1387, 1959.

[294] O. Karnland. Bentonite swelling pressure in strong nacl solutions. correlation between model calculations and experimentally determined data. Technical report, Swedish Nuclear Fuel and Waste Management Co., 1997.

[295] A. Alshawa, O. Dopfer, C. Harmon, S. Nizkorodov, and J. Underwood. Hygroscopic growth and deliquescence of nacl nanoparticles coated with surfactant aot. *The journal of physical chemistry. A*, 113(26):7678–7686, 2009.

[296] H. El-Dessouky, H. Ettouney, I. Alatiqi, and M. Al-Shamari. Evaporation rates from fresh and saline water in moving air. *Industrial & Engineering Chemistry Research*, 41(3):642–650, 2002.

Bibliography

146

Acknowledgements

Appendix

List of Publications

1. D. Gilzer, **R. Hillmann**, L. Goett-Zink, J. L. Klocke, M. Viefhues, D. Anselmetti, and T. Kottke. *Biphasic Formation of 2D Nanomembranes by Photopolymerization of Diacetylene Lipids Analyzed by Infrared Difference Spectroscopy*, submitted, 2019.

2. **R. Hillmann**, M. Viefhues, L. Goett-Zink, D. Gilzer, T. Hellweg, A. Gölzhäuser, T. Kottke, and D. Anselmetti. *Characterization of Robust and Free-Standing 2D-Nanomembranes of UV-Polymerized Diacetylene Lipids*, Langmuir 34 (10), 3256–3263, 2018.

3. S. Knust, D. Kreft, **R. Hillmann**, A. Meyer, M. Viefhues, P. Reimann, and D. Anselmetti. *Measuring DNA Translocation Forces Through MoS_2-Nanopores with Optical Tweezers*, Proceedings of the 7. NRW NanoConference, December 7-8, 2016, Münster, Germany, Materials Today: Proceedings, 4 (Suppl. 2), S168–S173, 2017.

4. **R. Hillmann**, D. Gilzer, N. Biere, S. Knust, M. Viefhues, K. Toensing, T. Kottke, and D. Anselmetti. *Preparation of 2D Phospholipid and Copolymer Nanomembranes*, Proceedings of the 7. NRW NanoConference, December 7-8, 2016, Münster, Germany, Materials Today: Proceedings, 4 (Suppl. 2), S87–S92, 2017.

Contributions to Conferences

1. **R. Hillmann**, M. Viefhues, K. Tönsing, T. Kottke, and D. Anselmetti. *Atomic Force Microscopy Study of Free-Standing and Supported Nanomembranes of UV-polymerized Lipids*, Bremen Nanopore Meeting 648. WE-Heraeus-Seminar, July 16-21, 2017, Bremen, Germany.

2. **R. Hillmann**, M. Eickmann, F. Heising, D. Gilzer, K. Tönsing, M. Viefhues, T. Kottke, and D. Anselmetti. *UV-Polymerized Langmuir-Blodgett Phospholipid Nanomembranes*, Spring Meeting of the German Physical Society, March 19-24, 2017, Dresden, Germany.

3. **R. Hillmann**, D. Gilzer, S. Knust, N. Biere, M. Viefhues, K. Tönsing, T. Kottke, and D. Anselmetti. *Preparation of 2D Phospholipid and Copolymer Nanomembranes*, 7. NRW NanoConference, December 7-8, 2016, Münster, Germany.

4. **R. Hillmann**, M. Eickmann, N. Biere, T. Kottke, K. Tönsing, M. Viefhues, and D. Anselmetti. *UV-Polymerized Langmuir-Blodgett Phospholipid Nanomembranes*, Young Academics, August 30-31, 2016, Siegen, Germany.

5. **R. Hillmann**, M. Dotter, L. Galla, C. Pelargus, U. Plachetka, A. Prinzen, D. Neumaier, H. Kleinjans, H. Kurz, and D. Anselmetti. *UV induced Polymerization of Phospholipids at Langmuir Blodgett Trough*, Spring Meeting of the German Physical Society, March 15-20, 2015, Berlin, Germany.

6. **R. Hillmann**, A. Spiering, A. Sischka, X. Fernández-Busquets, and D. Anselmetti. *Quantitative DNA Overstretching by Optical Tweezers*, Spring Meeting of the German Physical Society, March 30-April 4, 2014, Dresden, Germany.